Canonical Description of the Band Structure of Metals

Article · January 1985

CITATIONS
46

READS
77

6 authors, including:

O. K. Andersen
Max Planck Institute for Solid State Research
307 PUBLICATIONS **32,059** CITATIONS

SEE PROFILE

Reprinted From
Highlights of
Condensed-Matter Theory

Soc. Italiana di Fisica - Bologna - Italy

O. K. ANDERSEN - O. JEPSEN - D. GLÖTZEL

Canonical Description of the Band Structures of Metals.

MAX-PLANCK-INSTITUT FÜR FESTKÖRPERFORSCHUNG
7000 STUTTGART-80 - F.R.G.

TIPOGRAFIA COMPOSITORI BOLOGNA - 1985

Canonical Description of the Band Structures of Metals.

O. K. ANDERSEN, O. JEPSEN and D. GLÖTZEL

Max-Planck-Institut für Festkörperforschung
Heisenbergstrasse 1, 7000 *Stuttgart*-80, *B.R.D.*

1. – Introduction.

In this lecture we shall explain how the self-consistent band structure problem, arising, for instance, in density-functional theory [1], may be solved and we shall discuss the trends in the band structures and ground-state properties calculated for a variety of metallic systems [2, 3]. Rather than using pseudopotential methods as in a previous paper, we shall use so-called *linear* band structure methods [4-10], which can treat the full one-electron potential from the nuclei and all the electrons. This allows us to treat *s*-, *p*-, *d*- (and *f*-) electrons on the same footing and to use a *minimal basis set.* After explaining the general idea behind the linear methods in sect. **2**, we will in sect. **3** consider the most simple, so-called atomic-sphere approximation (ASA) [4]. In sect. **4** we develop the linear muffin-tin orbital (LMTO) method [5, 6]. In the ASA this method is quite accurate for closely packed systems and it has, together with its descendant, the augmented-spherical-wave (ASW) method [11], been used in numerous calculations for metals and intermetallic compounds. We will show how the set of MTOs may be transformed analytically into sets of exponentially localized orbitals and we specifically discuss two sets, the set of orthogonal orbitals [12] and the set of most localized orbitals [13]. This is a new development and it leads to an *extremely simple first-principles tight-binding method* whose transfer matrix factorizes into screened canonical structure constants characterizing the lattice and potential parameters characterizing the atomic-sphere potentials placed on the lattice. A tabulation of the canonical hopping integrals makes fairly accurate ($\sim$10 mRyd) do-it-yourself calculations for arbitrary structures feasible.

Even self-consistent calculations merely require the ability to solve radial Schrödinger (or Dirac) and Poisson equations and to diagonalize a small matrix. Moreover, with the localized orbitals it is easy to go beyond the ASA.

The trends in the band structures of 33 elemental metals will be discussed in sect. **5** on the basis of the canonical bands and a tabulation of the self-

consistent potential parameters. The cohesive and magnetic ground-state properties of the elemental metals are explained in sect. **6**. In sect. **7** some of the numerous applications of the LMTO-ASA and ASW methods to the electronic structures, chemical binding, heats of formation and magnetic structures of crystalline and amorphous metallic alloys are referenced. In sect. **8** we briefly review LMTO and linear augmented-plane-wave (LAPW) [5, 6, 14] calculations for metallic surfaces and chemisorbed layers. Our summary and outlook is given in sect. **9**.

2. – Linear methods.

In the first place, we want to solve Schrödinger's equation (in atomic Rydberg units as used throughout this lecture)

$$[-\nabla^2 + V(\boldsymbol{r})]\psi_j(\boldsymbol{r}) = E_j\psi_j(\boldsymbol{r}) \tag{1}$$

for one electron in a potential $V(\boldsymbol{r})$ characteristic for a system of atoms. In the second place, we may want to construct the charge density,

$$n(\boldsymbol{r}) = \sum_j^{\text{occ}} |\psi_j(\boldsymbol{r})|^2 , \tag{2}$$

and subsequently use it to find the potential $V(\boldsymbol{r})$ for a next iteration by solving Poisson's equation for the Hartree part and by using the (local) density-functional description [1] for the exchange correlation part. After self-consistency has been reached for the potential, we may, finally, wish to evaluate the total energy of the electrons and nuclei in the Born-Oppenheimer approximation.

A typical potential is shown in fig. 1*a*), where, specifically, we show the behaviour near the surface of a crystal. The one-electron states relevant for most physical and chemical properties are those with energies in the neighbourhood of 1 Ryd of the Fermi level, *i.e.* from about -1.5 to 0.5 Ryd in fig. 1. The contribution to the electron density from the lower-lying states nearly equals the corresponding contribution in the isolated atom and it is, in fact, often approximated by the core density calculated for isolated atoms (frozen-core approximation). The energy range relevant for us thus begins where the electron has sufficient energy to move from one atom to the next and, hence, when its energy reaches the level of the potential between the atoms.

Schrödinger's equation (1) may be solved by seeking the wave function as an expansion

$$\sum_G \bar{\chi}_G(\boldsymbol{r})\, \overline{u}_{G,j} \approx \psi_j(\boldsymbol{r}) \tag{3}$$

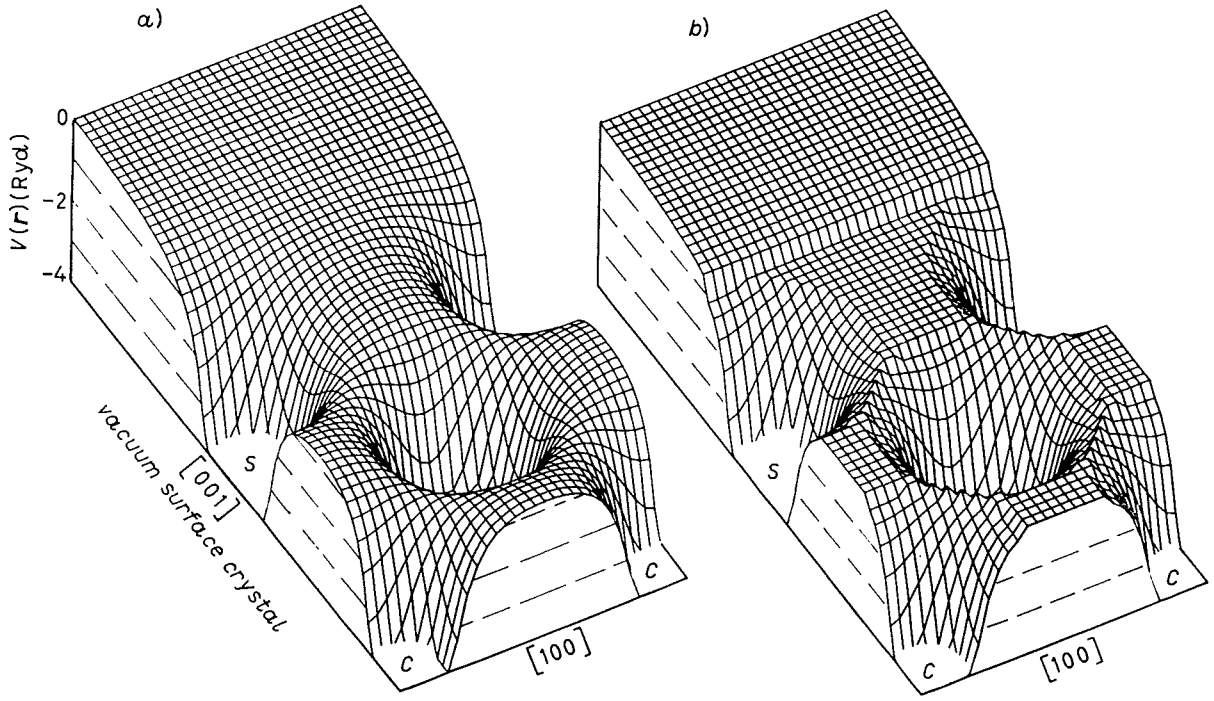

Fig. 1. – Self-consistent one-electron potential $V(\boldsymbol{r})$ near the (100) surface of a Ni crystal. This potential has been computed with the LAPW method [15]. Part *a*) is the full potential, while part *b*) is its muffin-tin average.

in some energy-independent set of basis functions $\bar{\chi}_G$ (the reason for the bar will be obvious later). The coefficients $\bar{u}_{G,j}$ and the one-electron energies E_j are then obtained with the help of the Rayleigh-Ritz variational principle as the eigenvectors and eigenvalues of the algebraic eigenvalue problem

$$(\bar{\boldsymbol{H}} - E\bar{\boldsymbol{O}})\,\bar{\boldsymbol{u}} = \boldsymbol{0} \tag{4}$$

with the Hamiltonian matrix $\bar{H}_{G'G} \equiv \langle \bar{\chi}_{G'} | -\nabla^2 + V | \bar{\chi}_G \rangle$ and the overlap matrix $\bar{O}_{G'G} \equiv \langle \bar{\chi}_{G'} | \bar{\chi}_G \rangle$. In common with many other methods, such as the linear combination of atomic orbitals (LCAO), the plane-wave and the Gaussian-orbital pseudopotential methods, the linear methods employ this highly convenient procedure. The linear methods are, however, distinguished by the way in which the basis functions are constructed and, in this respect, they have more similarity to mathematically explicit, but numerically cumbersome, methods such as the augmented-plane-wave (APW) [16] and the Korringa-Kohn-Rostoker (KKR) [17] methods which are based on partial-wave scattering theory. This we shall now explain.

The simplifying feature of Schrödinger's equation (1) with a potential like the one shown in fig. 1*a*) is that inside the atoms (or near the surface), where the kinetic energy $E_j - V(\boldsymbol{r})$ is numerically large and the wave function varies rapidly, the potential is essentially spherically (or planar) symmetric [18].

For the spherically symmetric part $v_R(|\boldsymbol{r}-\boldsymbol{R}|)$ it is, however, a trivial matter to solve Schrödinger's differential equation for any energy E inside any atom. The solutions are the partial waves

$$\varphi_{RL}(E, \boldsymbol{r}_R) \equiv \varphi_{Rl}(E, r_R)\, Y_L(\boldsymbol{r}_R)\,, \tag{5}$$

and each radial wave function φ_{Rl} may be obtained by numerical integration of the appropriate radial Schrödinger equation. In (5), and the following, $\boldsymbol{R}$ denotes the position of an atom, and $\boldsymbol{r}_R \equiv \boldsymbol{r} - \boldsymbol{R}$. Moreover, Y_L is a spherical (or real, cubic) harmonic and $L \equiv lm$ labels the angular momentum. The question is now how to incorporate the energy-dependent partial waves (5) in an energy-*in*dependent basis set, $\bar{\chi}_G(\boldsymbol{r})$?

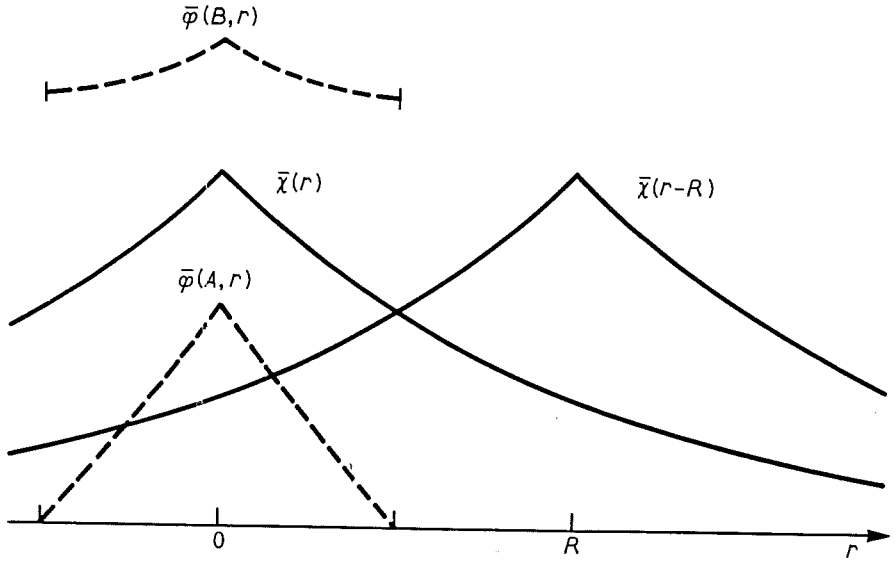

Fig. 2. – Bonding and antibonding states of a diatomic molecule.

To answer this we consider in fig. 2 a simplified model for bonding in a homonuclear diatomic molecule with just one atomic orbital $\bar{\chi}_L$. In the approximate LCAO description the bonding and antibonding states are

$$\psi_A^B(\boldsymbol{r}) \approx \bar{\chi}_L(\boldsymbol{r}) \pm (-)^l \bar{\chi}_L(\boldsymbol{r}-\boldsymbol{R}) \tag{6a}$$

and their energies, $E = B$ and A, may be estimated from (4). Inside any of the atoms, say the one at the origin, the *exact* states can, on the other hand, be expressed by the partial-wave expansions

$$\psi_A^B(\boldsymbol{r}) = \sum_{L'} \bar{\varphi}_{L'}\begin{pmatrix} B \\ A \end{pmatrix}, \boldsymbol{r}\Big) \bar{h}_{L'}\,, \tag{6b}$$

where the bars indicate that we have included the energy dependence of the expansion coefficients $\bar{h}_{L'}$, which depends on the choice of the orbital, in the normalization of the partial waves. In a *correct* description the tail of the orbital $\bar{\chi}_L(\boldsymbol{r}-\boldsymbol{R})$ should, therefore, be augmented in such a way that it equals

$$\tfrac{1}{2}(-)^l \sum_{L'} [\bar{\varphi}_{l'}(B, r) - \bar{\varphi}_{l'}(A, r)]\, Y_{L'}(\boldsymbol{r})\bar{h}_{L'}$$

inside the atom at the origin, and the head of the orbital $\bar{\chi}_L(\boldsymbol{r})$ should be augmented in such a way that it equals

$$\tfrac{1}{2}[\bar{\varphi}_l(B, r) + \bar{\varphi}_l(A, r)]\, Y_L(\boldsymbol{r})$$

deep inside its own atom.

Now, for a solid, there usually exists a continuous band of states in the range from B to A and, in this case, the entire energy dependence of the radial wave functions $\bar{\varphi}_{l'}(E, r)$ must be supplied by the tails of the energy-*in*dependent orbitals from the other sites. This can be accomplished in a convenient way if, instead of $[\bar{\varphi}_{l'}(B, r) - \bar{\varphi}_{l'}(A, r)]/2$, the tails are augmented by the energy derivative functions

$$\dot{\bar{\varphi}}_{l'}(r) \equiv [\partial\bar{\varphi}_{l'}(E, r)/\partial E]_{E_\nu} \tag{7}$$

evaluated at some energy E_ν at the centre of interest. The heads should, similarly, be augmented by the appropriate linear combination of

$$\bar{\varphi}_l(r) \equiv \bar{\varphi}_l(E_\nu, r) \tag{8}$$

and phi-dot (7).

This means that we can express the *augmented orbital* as

$$\bar{\chi}_{RL}(\boldsymbol{r}_R) = \bar{\chi}^{\mathrm{i}}_{RL}(\boldsymbol{r}_R) + \bar{\varphi}_{RL}(\boldsymbol{r}_R) + \sum_{R'} \sum_{L'} \dot{\bar{\varphi}}_{R'L'}(\boldsymbol{r}_{R'})\, \bar{h}_{R'L',RL}\,, \tag{9}$$

where $\bar{\varphi}_R$ and $\dot{\bar{\varphi}}_R$ are defined to be zero outside a chosen augmentation sphere for atom R. Moreover, $\bar{\chi}^{\mathrm{i}}$ is defined to be zero inside all augmentation spheres and to equal the original, approximate orbital in the interstitial region between the spheres. The normalization of the radial wave functions and the expansion coefficients $\bar{\boldsymbol{h}}$ can be chosen in such a way that the augmentations are continuous and once differentiable at the spheres. It may be shown [5, 6, 10] that, not only phi, but also phi-dot are orthogonal to the core states, and the phi–phi-dot augmentation could, therefore, be viewed as a way of orthogonalizing the orbitals to the core states.

The augmented orbitals (9) may now be used as basis functions (3) in a variational calculation and, for closely packed systems where the potential is nearly spherically symmetric in a large volume around each atom, the augmentation spheres are chosen as large as possible, either as touching muffin-tin (MT) spheres like the ones indicated in fig. 1*b*), or, even, as slightly overlapping, « space-filling » atomic Wigner-Seitz spheres (AS). The large spheres have the advantage that the « radial degree of freedom » is entirely described by the phi–phi-dot augmentation and only *one orbital per lm value* (*i.e.* a minimal basis set) is needed. That this works in a useful energy range is connected with the fact that the Taylor series

$$\varphi_l(E, r) \approx \varphi_l(r) + (E - E_\nu)\dot{\varphi}_l(r) \tag{10}$$

truncated after the first two, *linear* terms describes fairly well the change of the radial wave function throughout the atomic sphere ($r \leqslant s$), from the bonding shape, $\varphi_l(B, r)$, characterized by the boundary condition

$$\partial\varphi_l(B, r)/\partial r|_s = 0 \,, \tag{11}$$

to the antibonding shape, $\varphi_l(A, r)$, characterized by

$$\varphi_l(A, s) = 0 \,. \tag{12}$$

Moreover, since we use phi and phi-dot in a variational scheme, the error of the radial wave function (10), which is of second order in $E - E_\nu$, merely gives rise to fourth-order errors for the energy bands. That such a linear method using MT spheres yields accurate results over an energy range exceeding 1 Ryd is demonstrated for Pd metal in fig. 3.

In order to set up a linear method, we may start out from any set of envelope functions $\bar{\chi}^e_G(\boldsymbol{r})$ which is reasonably complete in the interstitial region. Plane waves give rise to the so-called LAPW method [5, 6, 14, 15, 19-23], MTOs [24, 25] to the so-called LMTO method [4-6, 10, 26-32] and Slater-type orbitals to the LSTO method [33]. After we have chosen a set, each basis function is then expanded in spherical harmonics about all the atomic sites $\boldsymbol{R}$ and each component is continuously and differentiably augmented with the appropriate radial phi and phi-dot functions inside spheres of chosen radii s_R. While the calculation of the contribution to the spherically symmetric part of the Hamiltonian matrix and to the overlap matrix from inside the spheres is simple and general and will be given in the following subsection, the calculation of the remaining contributions from the interstitial region and from the nonspherical potential inside the spheres is usually cumbersome and depends on the basis set [5, 12, 15, 27-30, 32, 34]. With the new localized

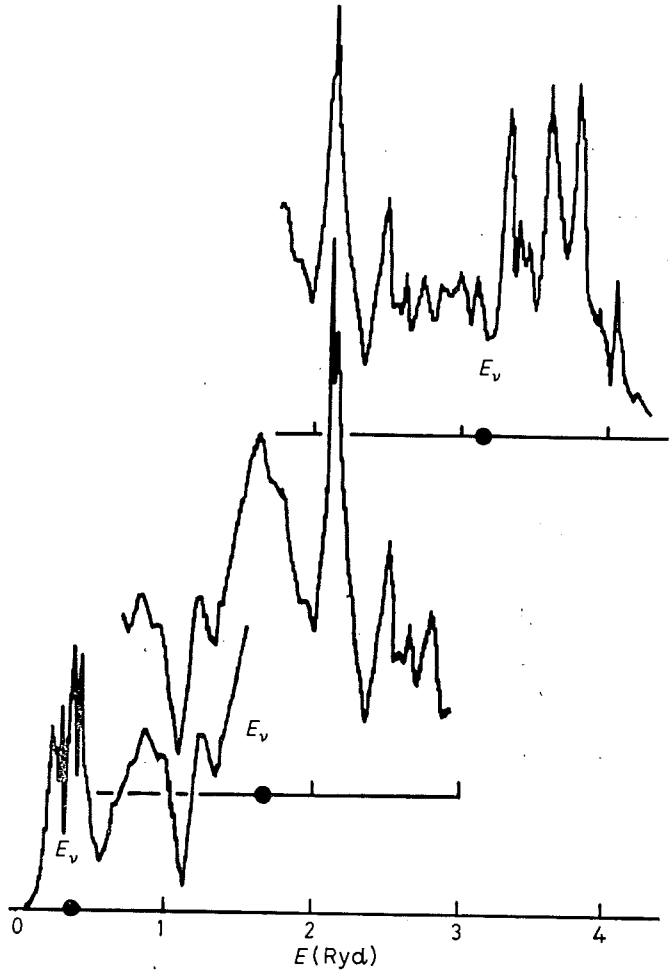

Fig. 3. – p-projected density of states for palladium metal. The Fermi level is at approximately 0.5 Ryd above the bottom of the s-band. The first peak between 0.1 and 0.5 Ryd arises from the $4d$-band. The picture is the result of 3 different LAPW calculations [20] with the E_ν's indicated. The (small) mismatch between the curves indicates the size of the second-order errors for the wave function and the fourth-order errors for the energies.

orbitals that we shall introduce in sect. 4 even this should now be straightforward. We shall not be concerned with the nonspherical terms in the following but concentrate on the so-called atomic-sphere approximation.

3. – **Atomic-sphere approximation** (ASA).

We now consider an infinite, closely packed solid and develop the simplest version of the linear methods in some detail. In this version we assume that space can be filled with Wigner-Seitz atomic spheres whose overlap we neglect. This means that, effectively, there is no interstitial region. The Wigner-Seitz spheres are taken as the augmentation spheres, whereby the term $\vec{\chi}^{\mathrm{i}}$ in (9)

drops out, and the nonspherical components of the potential are neglected. The one-electron energies obtained with the ASA are accurate to about one per cent of the appropriate band width, *e.g.* to about 10, 15 and 5 mRyd for transition metal *s*-, *p*- and *d*-bands.

3·1. *Phi and phi-dots.* – We first specify the normalizations of phi and phi-dot. Let $\varphi_{Rl}(E, r)$ be normalized to unity in its sphere, *i.e.*

$$\int_0^{s_R} \varphi_{Rl}(E, r)^2 r^2 \, \mathrm{d}r \equiv 1 \,. \tag{13}$$

Differentiation with respect to energy then reveals that the corresponding (unbarred) phi-dot is orthogonal to phi:

$$\int_0^{s_R} \varphi_{Rl}(E, r) \, \dot{\varphi}_{Rl}(E, r) \, r^2 \, \mathrm{d}r = 0 \,. \tag{14}$$

For the radial wave function, in each sphere R and for each angular momentum l, we thus use a 2-dimensional Hilbert space spanned by the *orthogonal*

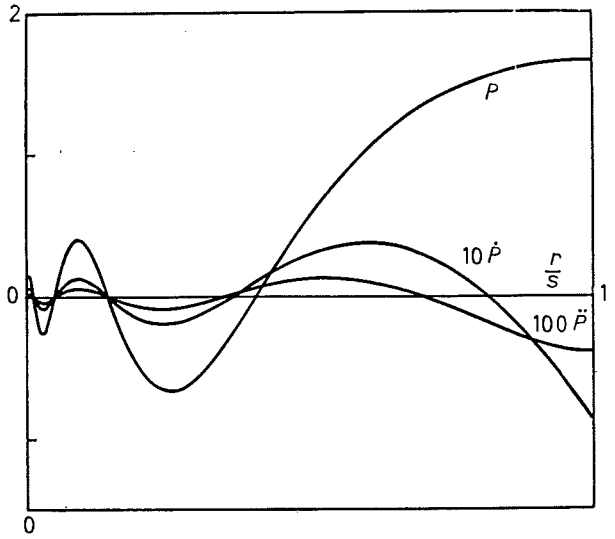

Fig. 4. – Radial φ_s, $\dot{\varphi}_s$ and $\ddot{\varphi}_s$ functions for yttrium. Here $\dot{\varphi}$ is orthogonal to φ and $D\{\varphi\} = -l - 1 = -1$. Moreover, $P \equiv s^{\frac{1}{2}} r\varphi$, $\dot{P} \equiv \partial P/\partial(Es^2)$ and $\ddot{P} \equiv \partial \dot{P}/\partial(Es^2)$.

functions phi and phi-dot. These are our radial basis functions and an example of such a pair is shown in fig. 4. In this figure the second energy derivative function $\ddot{\varphi}$ is shown as well, and we realize that for $E - E_\nu \leqslant s^{-2} \approx$ ≈ 0.1 Ryd the term $\frac{1}{2}(E - E_\nu)^2 \ddot{\varphi}(r)$ is two or three orders of magnitude smaller than $\varphi(r)$.

We then come to the previously defined functions with a bar. The normalization of the orbital in (9) is chosen in accordance with the definition

$$\bar{\varphi}_{Rl}(r) \equiv \varphi_{Rl}(r) . \tag{15}$$

For the energy dependence of phi-bar we may define

$$\bar{\varphi}_{Rl}(E, r) \equiv [1 + (E - E_\nu)\,\bar{o}_{Rl}]\varphi_{Rl}(E, r) , \tag{16}$$

such that

$$\dot{\bar{\varphi}}_{Rl}(r) = \dot{\varphi}_{Rl}(r) + \varphi_{Rl}(r)\,\bar{o}_{Rl} . \tag{17a}$$

This means that *any energy derivative function is a linear combination of the orthogonal pair*. The constants $\bar{o}$ must now be determined in such a way that the linear combination of $\dot{\bar{\varphi}}_{RL}(\boldsymbol{r}_R)$ functions in (9) matches continuously and differentiably onto the tail of $\bar{\chi}_{R'L'}(\boldsymbol{r}_{R'})$. This requires that, at the sphere, the logarithmic derivative

$$D\{\dot{\bar{\varphi}}_{Rl}\} \equiv \partial \ln \dot{\bar{\varphi}}_{Rl}(r)/\partial \ln r|_{s_R} \tag{18}$$

has the correct value $\bar{D}_{Rl,R'L'}$. For MTOs this will be considered in detail in sect. **4**.

The Hamiltonian and overlap matrices in (4) will in subsect. **3**·2 be expressed entirely in terms of the expansion coefficients $\bar{h}$ and $\bar{o}$. To derive the expressions it is convenient to use a combined vector and bra-ket notation according to which (9) in the ASA is written as

$$|\bar{\chi}\rangle^{\infty} = |\varphi\rangle + |\dot{\bar{\varphi}}\rangle\,\bar{\boldsymbol{h}} . \tag{19}$$

As usual, the function $|\bar{\chi}_{RL}\rangle^{\infty}$ extends over all space, while the functions $|\varphi_{RL}\rangle$ and $|\dot{\bar{\varphi}}_{RL}\rangle$ vanish outside their own spheres. In (19), moreover, $|\varphi\rangle$, $|\dot{\bar{\varphi}}\rangle$ and $|\bar{\chi}\rangle^{\infty}$ are row vectors with components $|\varphi_{RL}\rangle$, etc. Similarly, $\langle\varphi|$, etc. will be column vectors, while $\bar{\boldsymbol{h}}$ and ${}^{\infty}\langle\bar{\chi}|\bar{\chi}\rangle^{\infty}$, etc. are matrices. If $\bar{D}_{Rl,R'L'}$ depends on $R'L'$, then eq. (17*a*) must be generalized to

$$|\dot{\bar{\varphi}}\rangle = |\dot{\varphi}\rangle + |\varphi\rangle\,\bar{\boldsymbol{o}} \tag{17b}$$

with $\bar{\boldsymbol{o}}$ being a nondiagonal matrix. For MTOs, however, this is not the case; $\bar{\boldsymbol{o}}$ is diagonal and $\bar{\boldsymbol{h}}$ will turn out to be Hermitian. With the vector and bra-ket notation and the inclusion of the angular variables (13), (14) and (17) give

the matrix equations

$$(20)\qquad \begin{cases} \langle\varphi|\varphi\rangle = \boldsymbol{I}\,, & \langle\varphi|\dot{\varphi}\rangle = \boldsymbol{0}\,, \\ \langle\varphi|\dot{\bar{\varphi}}\rangle = \bar{\boldsymbol{o}} \quad \text{and} & \langle\dot{\bar{\varphi}}|\dot{\bar{\varphi}}\rangle \equiv \bar{\boldsymbol{p}} = \bar{\boldsymbol{o}}^2 + \boldsymbol{p}\,. \end{cases}$$

$\boldsymbol{I}$ is the unit matrix and we see that $\bar{\boldsymbol{o}}$ is the overlap of phi and phi-bar-dot. Moreover, $\boldsymbol{p}$ is a diagonal matrix with elements

$$(21a)\qquad p_{Rl} \equiv \langle\dot{\varphi}^2_{Rl}\rangle \equiv \int_0^{s_R} \dot{\varphi}_{Rl}(E, r)^2 r^2\,\mathrm{d}r\,,$$

and we realize that $0 \leqslant p_{Rl} \leqslant \bar{p}_{Rl,Rl}$. The p_{Rl}'s will turn out to be the small parameters of a linear method and only those eigenvalues for which $(E_j - E_\nu)p^{\frac{1}{2}}$ are less than unity, with p being an appropriate average of the p_{Rl}'s, will be accurately given by the method. It may furthermore be shown that [5, 6]

$$(21b)\qquad p_{Rl} = -\langle\varphi_{Rl}|\ddot{\varphi}_{Rl}\rangle = -\ddot{\varphi}_{Rl}(s_R)[3\varphi_{Rl}(s_R)]^{-1}\,,$$

where the second energy derivative function was shown in fig. 4.

3·2. *Hamiltonian and overlap matrices.* – The overlap matrix is seen to be given by

$$(22)\qquad \bar{\boldsymbol{O}} \equiv {}^{\infty}\langle\bar{\chi}|\bar{\chi}\rangle^{\infty} = \boldsymbol{I} + \bar{\boldsymbol{o}}\bar{\boldsymbol{h}} + (\bar{\boldsymbol{o}}\bar{\boldsymbol{h}})^{+} + \bar{\boldsymbol{h}}^{+}\boldsymbol{p}\bar{\boldsymbol{h}} = (\boldsymbol{I} + \bar{\boldsymbol{o}}\bar{\boldsymbol{h}})^{+}(\boldsymbol{I} + \bar{\boldsymbol{o}}\bar{\boldsymbol{h}}) + \bar{\boldsymbol{h}}^{+}\boldsymbol{p}\bar{\boldsymbol{h}}\,.$$

Apart from the on-site term of $\bar{\boldsymbol{h}}$ (see (9)) the terms in the first part of (22) are the one-, two- and three-centre terms, respectively. In order to calculate the Hamiltonian matrix, we first note that Schrödinger's equation yields

$$(23)\qquad (-\nabla^2 + V)|\bar{\varphi}(E)\rangle = E|\bar{\varphi}(E)\rangle$$

and, hence,

$$(24)\qquad (-\nabla^2 + V - E_\nu)|\varphi\rangle = \boldsymbol{0} \quad \text{and} \quad (-\nabla^2 + V - E_\nu)|\dot{\bar{\varphi}}\rangle = |\varphi\rangle\,.$$

Consequently

$$(25)\qquad \bar{\boldsymbol{H}} \equiv {}^{\infty}\langle\bar{\chi}|-\nabla^2 + V|\bar{\chi}\rangle^{\infty} = (\boldsymbol{I} + \bar{\boldsymbol{o}}\bar{\boldsymbol{h}})^{+}\bar{\boldsymbol{h}} + (\boldsymbol{I} + \bar{\boldsymbol{o}}\bar{\boldsymbol{h}})^{+}\boldsymbol{E}_\nu(\boldsymbol{I} + \bar{\boldsymbol{o}}\bar{\boldsymbol{h}}) + \bar{\boldsymbol{h}}^{+}\boldsymbol{E}_\nu\boldsymbol{p}\bar{\boldsymbol{h}}\,,$$

which, again, involves one-, two- and three-centre terms. In (25) $\boldsymbol{E}_\nu$ is a diagonal matrix with elements $E_{\nu Rl}$ and, in case these are chosen independent of R and l, then all one-electron energies may be measured relative to E_ν such

that the second and third terms in (25) drop out. Technically speaking, $\boldsymbol{E}_\nu$ in this case commutes with the surrounding matrices and the second and third terms in (25) may, therefore, be taken together with the overlap matrix (22).

One standard way of handling an eigenvalue problem with an overlap matrix (4) involves Cholesky factorization of the overlap matrix and reduction of the transformed Hamiltonian to a real symmetric tridiagonal matrix [35]. Another involves Löwdin orthogonalization [36] of the orbitals through multiplication of $\bar{\boldsymbol{H}} - E\bar{\boldsymbol{O}}$ in (4) from the left and from the right by $\bar{\boldsymbol{O}}^{-\frac{1}{2}}$. For a linear method the latter way is the more convenient one, because we essentially know the square root of the overlap matrix; it is simply $\boldsymbol{I} + \bar{\boldsymbol{o}}\bar{\boldsymbol{h}}$, as (22) shows. The reason for this approximate factorization becomes obvious if we insert (17) in (19) and use the orthogonality of phi and phi-dot:

$$|\bar{\chi}\rangle^\infty = |\varphi\rangle(\boldsymbol{I} + \bar{\boldsymbol{o}}\bar{\boldsymbol{h}}) + |\dot{\varphi}\rangle\,\bar{\boldsymbol{h}}\,. \tag{26}$$

Assuming now that the matrix $\boldsymbol{I} + \bar{\boldsymbol{o}}\bar{\boldsymbol{h}}$ can be inverted, we may transform to the following new set of (unbarred) orbitals

$$|\chi\rangle^\infty \equiv |\bar{\chi}\rangle^\infty(\boldsymbol{I} + \bar{\boldsymbol{o}}\bar{\boldsymbol{h}})^{-1} = |\varphi\rangle + |\dot{\varphi}\rangle\,\boldsymbol{h}\,, \tag{27}$$

where

$$\boldsymbol{h} \equiv \bar{\boldsymbol{h}}(\boldsymbol{I} + \bar{\boldsymbol{o}}\bar{\boldsymbol{h}})^{-1} \quad \text{or} \quad \boldsymbol{h}^{-1} = \bar{\boldsymbol{o}} + \bar{\boldsymbol{h}}^{-1}\,. \tag{28}$$

In the new basis the Hamiltonian is immediately seen to be

$$\boldsymbol{H} = \boldsymbol{E}_\nu + \boldsymbol{h} + \boldsymbol{h}\boldsymbol{E}_\nu\boldsymbol{p}\boldsymbol{h} \equiv \boldsymbol{H}^{(2)} + \boldsymbol{h}\boldsymbol{E}_\nu\boldsymbol{p}\boldsymbol{h}\,, \tag{29}$$

and, since $\boldsymbol{H}$ must be Hermitian, and $\boldsymbol{E}_\nu$ and $\boldsymbol{p}$ are diagonal, $\boldsymbol{h}$ is Hermitian. The overlap matrix in the new (unbarred) basis is

$$\boldsymbol{O} = \boldsymbol{I} + \boldsymbol{h}\boldsymbol{p}\boldsymbol{h}\,. \tag{30}$$

This means that the new set of orbitals is *orthogonal to first order* in $\boldsymbol{h} \approx \boldsymbol{H} - \boldsymbol{E}_\nu$, and that it is specified by the vector analogue (27) of the scalar first-order Taylor series (10) for energy dependence of the radial wave functions. We emphasize that, in the ASA, there is only *one matrix* which determines both the Hamiltonian and the overlap matrices, as well as the coefficients in the one-centre expansion (27) of the orbitals, and this is $\boldsymbol{h}$. The additional matrices, $\boldsymbol{E}_\nu$ and $\boldsymbol{p}$, are diagonal potential parameters.

It is now a simple matter to solve Schrödinger's equation. We first diagonalize $\boldsymbol{H}^{(2)} \equiv \boldsymbol{E}_\nu + \boldsymbol{h}$:

$$\boldsymbol{u}_j^+ \boldsymbol{H}^{(2)} \boldsymbol{u}_j = E_j^{(2)}\,, \qquad \text{with } \boldsymbol{u}^+\boldsymbol{u} = \boldsymbol{u}\boldsymbol{u}^+ = \boldsymbol{I}\,, \tag{31}$$

obtaining the eigenvectors $\boldsymbol{u}_j$ and the eigenvalues $E_j^{(2)}$. The corresponding wave functions, correct to first order in $E_j - E_\nu$, are

$$\begin{aligned}(32)\qquad \psi_j(\boldsymbol{r}) &= \sum_{RL} \chi_{RL}(\boldsymbol{r}_R)\, u_{RL,j} = \\ &= \sum_{RL} [\varphi_{Rl}(r_R) + (E_j^{(2)} - E_{\nu lR})\,\dot{\varphi}_{Rl}(r_R)]\, Y_L(\boldsymbol{r}_R)\, u_{RL,j} \approx \\ &\approx \sum_{RL} \varphi_{Rl}(E_j, r_R)\, Y_L(\boldsymbol{r}_R)\, u_{RL,j}\,,\end{aligned}$$

where the form (27) and the fact that $\boldsymbol{u}$ diagonalizes $\boldsymbol{H}^{(2)}$ (31) have allowed us to transform the multicentre expansion of overlapping energy-*in*dependent orbitals into one-centre expansions of nonoverlapping energy-*de*pendent partial waves (to first order in energy). The eigenvalues $E_j^{(2)}$ of (31) have errors of third and higher order in their deviation from E_ν, because, so far, we have neglected the second-order terms of the Hamiltonian and overlap matrices (29) and (30). These terms are most simply taken into account by first-order perturbation theory. From (4) and (29)-(31)

$$\begin{aligned}0 = \boldsymbol{u}_j^+[\boldsymbol{H}^{(2)} + \boldsymbol{h}\boldsymbol{E}_\nu\boldsymbol{p}\boldsymbol{h} - E(\boldsymbol{I} + \boldsymbol{h}\boldsymbol{p}\boldsymbol{h})]\boldsymbol{u}_j = \\ = E_j^{(2)} + \boldsymbol{u}_j^+ \boldsymbol{E}_\nu \boldsymbol{p}(E_j^{(2)}\boldsymbol{I} - \boldsymbol{E}_\nu)^2 \boldsymbol{u}_j - E[1 + \boldsymbol{u}_j^+ \boldsymbol{p}(E_j^{(2)}\boldsymbol{I} - \boldsymbol{E}_\nu)^2 \boldsymbol{u}_j]\end{aligned}$$

and the one-electron energy correct to third order in $E_j - E_\nu$ is, therefore, given by

$$(33)\qquad E_j = \frac{E_j^{(2)} + \sum_{Rl} E_{\nu Rl}\, p_{Rl}(E_j^{(2)} - E_{\nu Rl})^2 \sum_m |u_{RL,j}|^2}{1 + \sum_{Rl} p_{Rl}(E_j^{(2)} - E_{\nu Rl})^2 \sum_l |u_{RL,j}|^2}\,.$$

3·3. *Transformation between orbital sets.* – It should be realized that the only thing special about the set $|\overline{\chi}\rangle$ and the associated quantities carrying a bar is that this is the set we started out from by augmentation of some set of envelope functions $|\overline{\chi}^e\rangle$. Our formalism is, however, valid for any choice of $\bar{\boldsymbol{o}}$ in (17), provided that the corresponding set of orbitals is continuously differentiable and localized. In the following sect. 4 we shall explicitly transform, not only to the set of orthogonal orbitals, for which $\boldsymbol{o} \equiv 0$, but also to a set of highly localized orbitals. The transformation between various sets is given by (28) which states that $\bar{\boldsymbol{o}} + \bar{\boldsymbol{h}}^{-1}$ is invariant. Specifically, if for some matrix $\bar{\bar{\boldsymbol{o}}}$ the matrix $\boldsymbol{I} + (\bar{\boldsymbol{o}} - \bar{\bar{\boldsymbol{o}}})\,\bar{\boldsymbol{h}}$ can be inverted, one may obtain the following set

$$(34a)\qquad |\bar{\bar{\chi}}\rangle^\infty \equiv |\overline{\chi}\rangle^\infty [\boldsymbol{I} + (\bar{\boldsymbol{o}} - \bar{\bar{\boldsymbol{o}}})\,\bar{\boldsymbol{h}}]^{-1} = |\varphi\rangle + |\dot{\bar{\varphi}}\rangle\,\bar{\bar{\boldsymbol{h}}} + |\bar{\bar{\chi}}\rangle^1\,,$$

where

$$(34b)\qquad \bar{\bar{\boldsymbol{h}}} \equiv \bar{\boldsymbol{h}}[\boldsymbol{I} + (\bar{\boldsymbol{o}} - \bar{\bar{\boldsymbol{o}}})\,\bar{\boldsymbol{h}}]^{-1}\,, \quad \text{or} \quad \bar{\bar{\boldsymbol{o}}} + \bar{\bar{\boldsymbol{h}}}^{-1} = \bar{\boldsymbol{o}} + \bar{\boldsymbol{h}}^{-1}\,,$$

and

$$|\bar{\bar{\chi}}\rangle^{\mathrm{i}} \equiv |\bar{\chi}\rangle^{\mathrm{i}}[\boldsymbol{I} + (\bar{\mathbf{o}} - \bar{\bar{\mathbf{o}}})\,\bar{\boldsymbol{h}}]^{-1} = |\bar{\chi}\rangle^{\mathrm{i}}[\boldsymbol{I} + (\bar{\mathbf{o}} - \bar{\mathbf{o}})\,\bar{\bar{\boldsymbol{h}}}]\,. \tag{34c}$$

We have included $|\bar{\chi}\rangle^{\mathrm{i}}$ like in (9) in order to stress that the transformations have general validity and do not require the ASA. The correctness of (34) follows from (19) and from

$$|\dot{\bar{\bar{\varphi}}}\rangle = |\dot{\bar{\varphi}}\rangle + |\varphi\rangle(\bar{\bar{\mathbf{o}}} - \bar{\mathbf{o}}) \tag{35}$$

as obtained from (17*b*).

3·4. ASA *density and total energy.* – In order to perform self-consistent calculations in the ASA, one merely needs the electron density, spherically averaged in each sphere, and, for this purpose, the one-centre expansions are sufficiently accurate. The spherical density per spin is in general given by

$$n_R(r) = (4\pi)^{-1} \sum_l \int^{E_F} \varphi_{Rl}(E, r)^2 N_{Rl}(E)\,\mathrm{d}E\,, \tag{36}$$

in terms of the projected densities of states

$$N_{Rl}(E) \equiv \sum_j \delta(E - E_j) \sum_m |u_{RL,j}|^2\,. \tag{37}$$

If we now expand phi in a Taylor series and define the projected number of states

$$n_{Rl} \equiv \int^{E_F} N_{Rl}(E)\,\mathrm{d}E = \sum_j^{\mathrm{occ}} \sum_m |u_{RL,j}|^2 \tag{38}$$

and energy moments

$$m_{Rl}^{(q)} \equiv \int^{E_F} (E - E_{\nu Rl})^q N_{Rl}(E)\,\mathrm{d}E\,, \tag{39}$$

the density may conveniently be expressed as

$$n_R(r) = (4\pi)^{-1} \sum_l [n\varphi(r)^2 + m^{(1)} 2\varphi(r)\dot{\varphi}(r) + m^{(2)}\{\dot{\varphi}(r)^2 + \varphi(r)\,\ddot{\varphi}(r)\}]\,. \tag{40}$$

This is valid to second order and we have dropped the subscripts *Rl* inside the square parenthesis. The reason for going to second rather than only to first order, as in (32), is that the eigenvectors (31), in fact, are correct to second order. This will be proved in sect. **4**. It should be noted that the projection (37)-(39) is onto the nonoverlapping partial waves *as well as* onto

the overlapping, nearly orthogonal orbitals. This follows from (32). Only the first term in (40) contributes net l-charge to the sphere and the remaining terms merely redistribute the l-charge within that sphere. This is seen by integrating each term in the sphere and using (13), (14) and the energy derivative of the latter.

The total energy of the electrons in the ground state may, according to the density-functional theory [1], be estimated as

$$E_{\mathrm{tot}}^{\mathrm{el}} = T + \int\int n(\boldsymbol{r})|\boldsymbol{r}-\boldsymbol{r}'|^{-1} n(\boldsymbol{r}')\,\mathrm{d}^3r\,\mathrm{d}^3r' + E_{\mathrm{xc}}\{n(\boldsymbol{r})\} + \int v_{\mathrm{ext}}(\boldsymbol{r})n(\boldsymbol{r})\,\mathrm{d}^3r\,. \tag{41}$$

Here, v_{ext} is the electrostatic potential from the nuclei and $n(\boldsymbol{r})$ is the total electronic density generated by some potential $V(\boldsymbol{r})$ which, thanks to the variational property of the energy functional (41), need not be the exact self-consistent one, but, for instance, the self-consistent atomic-sphere potential. The first, kinetic-energy term in (41) should accordingly be expressed as the difference between the total and potential energies of the noninteracting electrons in the potential $V(\boldsymbol{r})$. In the ASA, therefore,

$$T = \int^{E_{\mathrm{F}}} EN(E)\,\mathrm{d}E - \sum_R \int_0^{s_R} v_R(r) n_R(r)\, 4\pi r^2\,\mathrm{d}r\,, \tag{42}$$

where $N(E)$ and $n_R(r)$ now include both spin directions. In the remaining terms of (41) the full, rather than the spherically averaged, density should be used. However, for calculations that do not require symmetry-lowering displacements of the nuclei the spherical average is sufficiently accurate. In this approximation, and including now the electrostatic interaction between the nuclei, and using furthermore the *local* density-functional approximation, the total-energy expression takes the most simple form

$$E_{\mathrm{tot}} = T + \sum_R \sum_{R'}{}' z_R|\boldsymbol{R}-\boldsymbol{R}'|^{-1} z_{R'} + \sum_R U_R\,. \tag{43}$$

Here, z_R is the nuclear minus the electronic charge in the sphere at $\boldsymbol{R}$. The second term in (43) is thus the int*er*sphere Coulomb (or Madelung) energy. The third term in (43) is the sum of the int*ra*sphere interactions between the electrons and between the electrons and the nucleus in that sphere, that is,

$$U = \int_0^s n(r)\left[\varepsilon_{\mathrm{xc}}(n(r)) - \frac{2Z}{r} + \int_0^s \frac{n(r')4\pi r'^2\,\mathrm{d}r'}{|\boldsymbol{r}-\boldsymbol{r}'|}\right] 4\pi r^2\,\mathrm{d}r\,, \tag{44}$$

where we have dropped the subscripts R.

4. – Muffin-tin orbitals.

We now choose a particular basis set and thereby obtain specific expressions for the second-order Hamiltonian $\boldsymbol{h}$, as well as for the family of first-order Hamiltonians $\bar{\boldsymbol{h}}$. We shall use muffin-tin orbitals because, with these, the dependences on structure and atomic-sphere potentials factorize and the convergence in l is so fast that the 9 s-, p- and d-orbitals per atom suffice for most applications.

4·1. *Multipole fields and screening.* – In sect. **2** we mentioned that a requirement on the nonaugmented basis set (or envelope set) is that it is reasonably complete in the interstitial region. Now, if the interstitial region is small, or nonexisting as in the ASA, this requirement is mild, but we must, of course, demand that each envelope function is so smooth that the radius of convergence in the one-centre angular-momentum expansion (9) exceeds the atomic-sphere radius. For fast l-convergence it is, furthermore, important that each function is a reasonable solution of Schrödinger's differential equation (1) in a larger region between the atoms, because then the augmentation only needs to take place for the few lower l-components (*i.e.* the s-, p- and, for transition and noble metals, the d- and, for rare earths and actinides, possibly the f-components). Between the atoms the potential is rather flat (fig. 1) and the kinetic energy $E - V(\boldsymbol{r})$ varies between approximately -1 and 1 Ryd. It is, therefore, quite accurate to choose basis functions whose envelopes are solutions of the wave equation $(\nabla^2 + \kappa^2)\bar{\chi}^e = 0$ with a small kinetic energy κ^2. This choice yields far better l-convergence than the use of Gaussian- or Slater-type orbitals.

The KKR and APW methods also employ wave equation solutions and the potential is approximated by a spherically symmetric one inside touching muffin-tin spheres and a flat one (of value V_{MTZ}) in the interstitial region. Such a MT potential was shown in fig. 1*b*). In these scattering methods one then chooses $\kappa^2 \equiv E - V_{\text{MTZ}}$ such that $\bar{\chi}^e$ is an *exact* solution of Schrödinger's equation (for the approximate MT potential) in the interstitial region. In the linear method we must, however, take a constant, energy-*in*dependent value of kappa in order that our basis functions be independent of energy such that we arrive at an eigenvalue problem (4). When evaluating the Hamiltonian and overlap matrices, we must then include the integrals over the interstitial region, or eliminate them by use of the ASA. We shall from now on use the simplest choice, $\kappa^2 = 0$, whereby the wave equation reduces to the Laplace equation.

The envelope function, $\bar{\chi}^e_{RL}(\boldsymbol{r}_R)$, of a MTO is defined as an atom-centred angular-momentum eigenfunction of the Laplace equation, and this means that it has the form of a static multipole field, $K_{RL}(\boldsymbol{r}_R)$, with the well-known [37]

one-centre expansion

$$(45)\qquad K_{RL}(\boldsymbol{r}_R) \equiv \left(\frac{r_R}{w}\right)^{-l-1} Y_L(\boldsymbol{r}_R) = -\sum_{L'} \left(\frac{r_{R'}}{w}\right)^{l'} \frac{Y_{L'}(\boldsymbol{r}_{R'})}{2(2l'+1)} S_{R'L',RL} \equiv$$
$$\equiv -\sum_{L'} J_{R'L'}(\boldsymbol{r}_{R'}) S_{R'L',RL} ,$$

valid for $r_{R'} < |\boldsymbol{R} - \boldsymbol{R}'|$. Here, J_{RL} is the regular and K_{RL} the irregular solution of the Laplace equation and the factor $2(2l+1)$ has been included in the definition of J_{RL} such that the matrix $\boldsymbol{S}$ is Hermitian. Moreover, we have chosen to measure all distances in units of some arbitrary length, w, say the lattice constant or, as we prefer, the average Wigner-Seitz radius of the lattice.

The expansion coefficients $\boldsymbol{S}$ are the so-called *bare canonical structure constants* which only depend on the atomic positions (in units of w); they are independent of the atomic-sphere potentials and radii. Expressed as two-centre integrals [38] with the z-axis chosen along the interatomic vector $\boldsymbol{R}-\boldsymbol{R}'$, of length d, the bare canonical structure constants are explicitly

$$(46)\qquad \begin{cases} S_{ss\sigma} = -2(w/d)\,, \quad S_{sp\sigma} = (2\sqrt{3})(w/d)^2\,, \quad S_{pp(\sigma,\pi)} = 6(w/d)^3(2,-1)\,, \\ S_{sd\sigma} = -(2\sqrt{5})(w/d)^3\,, \qquad S_{pd(\sigma,\pi)} = (6\sqrt{5})(w/d)^4(-\sqrt{3},1)\,, \\ S_{dd(\sigma,\pi,\delta)} = 10(w/d)^5(-6,4,-1)\,, \end{cases}$$

or

$$(47)\qquad S_{l'lM} = (-)^{l+M+1}(l'+l)!\,2\left[\frac{(2l'+1)(2l+1)}{(l'+M)!(l'-M)!(l+M)!(l-M)!}\right]^{\frac{1}{2}}\left(\frac{w}{d}\right)^{l'+l+1}.$$

For a general direction of the z-axis, *e.g.* the global z-axis of a crystal, the structure matrix may be obtained from (46) or (47) and table I in ref. [38] or, directly, from table II in ref. [9].

The requirement of fast l-convergence (*e.g.* $\varkappa^2$ equal to zero rather than negative and large) seemingly leads to a long-range, power law decay (45), for the MTOs. It is one of the objectives of the present lecture to disprove this and to construct short-range « wave packets » from the s, p, and d bare MTOs with $\varkappa$ equal to zero.

Since we are going to augment the envelope function, not only inside the atom at which it is centred but also inside all other atoms, we might instead of (45) use solutions of the Laplace equation which are irregular also at the neighbouring sites. In this way we can *screen* the field from the multipole at $\boldsymbol{R}$ by surrounding it by multipoles at the neighbouring atoms and, hence, obtain a very localized field. In order to express this in a convenient way, we shall use the same combined braket and vector notation as in sect. **3**, and we shall write down transformations equivalent to those given there for linear basis sets in general. With this notation the one-centre expansions of

the bare multipole field (45) about *all* sites of the structure are

$$|\boldsymbol{K}\rangle^{\infty} = |\boldsymbol{K}\rangle - |\boldsymbol{J}\rangle \boldsymbol{S}\,, \tag{48}$$

where $|K_{RL}\rangle^{\infty}$ extends over all space, whereas $|K_{RL}\rangle$, like $|J_{RL}\rangle$, vanishes outside its own Wigner-Seitz cell. The on-site elements of $\boldsymbol{S}$ are defined as zero.

We now modify the regular solution $|J_{R'L'}\rangle$ by adding the amount $-\bar{Q}_{R'l'}$ of the irregular solution, *i.e.* we define

$$|\bar{\boldsymbol{J}}\rangle \equiv |\boldsymbol{J}\rangle - |\boldsymbol{K}\rangle \bar{\boldsymbol{Q}}\,, \tag{49}$$

where $\bar{\boldsymbol{Q}}$ is a diagonal matrix. The multipole field screened accordingly is defined in analogy with (48) as

$$|\bar{\boldsymbol{K}}\rangle^{\infty} \equiv |\boldsymbol{K}\rangle - |\bar{\boldsymbol{J}}\rangle \bar{\boldsymbol{S}}\,, \tag{50}$$

and insertion of (49) into (48) reveals that the screened structure matrix is given by

$$\bar{\boldsymbol{S}} = \boldsymbol{S}(\boldsymbol{I} - \bar{\boldsymbol{Q}}\boldsymbol{S})^{-1} \quad \text{or} \quad \bar{\boldsymbol{S}}^{-1} + \bar{\boldsymbol{Q}} = \boldsymbol{S}^{-1} \quad \text{or} \quad \bar{\boldsymbol{S}} = \boldsymbol{S} + \boldsymbol{S}\bar{\boldsymbol{Q}}\bar{\boldsymbol{S}} \tag{51}$$

and that the screened multipole field is given by the superposition

$$|\bar{\boldsymbol{K}}\rangle^{\infty} = |\boldsymbol{K}\rangle^{\infty}(\boldsymbol{I} - \bar{\boldsymbol{Q}}\boldsymbol{S})^{-1} = |\boldsymbol{K}\rangle^{\infty}(\boldsymbol{I} + \bar{\boldsymbol{Q}}\bar{\boldsymbol{S}}) \tag{52}$$

of bare multipole fields. We see that $\bar{Q}\bar{S}$ is the « screening charge ».

We now want to determine $\bar{\boldsymbol{Q}}$ such that (51) and (52) have the shortest possible range. In order to avoid using *f*-, *g*-, etc. orbitals in the augmented basis set, it is necessary to choose $\bar{Q}_l = 0$ for $l > 2$, as will be explained in subsect. 4·9. Moreover, we want the screened structure constants and envelope functions to be *canonical*, that is, independent of the atomic potentials and the scale of the structure, and, therefore, choose $\bar{\boldsymbol{Q}}$ to be site-independent. We are thus left with the three parameters $\bar{Q}_s$, $\bar{Q}_p$ and $\bar{Q}_d$. By numerical inversion of the 9×9 matrix $\bar{Q}_l^{-1}\delta_{LL'} - S^k_{LL'}$ on a lattice with Bloch vectors $\boldsymbol{k}$ and subsequent Fourier transformation into $\bar{S}_{RL,R'L'}$ this matrix and the $\bar{Q}$-values which give it the shortest possible range have been determined [13]. The results for the f.c.c., b.c.c. and s.c. structures are given in table I. The $\bar{Q}$-values turn out to be independent of the lattice type and are given in (77*a*) in subsect. 4·3. $\bar{S}_{ss\sigma}(d/w)$ is indicated by the full curve in fig. 5, and it is seen that the results for screening on various lattices (f.c.c. = crosses, b.c.c. = open circles, s.c. = full circles) lie on the same curve. Moreover, for all three lattices considered the screening is essentially complete after the first and second nearest

neighbours. The dotted curve in fig. 5 is the bare structure constant $-2(w/d)$ from (46). The dashed b.c.c. and f.c.c. curves, which do not coincide, are the s-structure constant screened in such a way that the s-MTOs are the nearly orthogonal ones given by (27). This requires, as we shall see in (64), that the $\bar{Q}$'s are chosen equal to certain potential parameters named Q. The results given by the dashed lines in fig. 5 were obtained for vanadium.

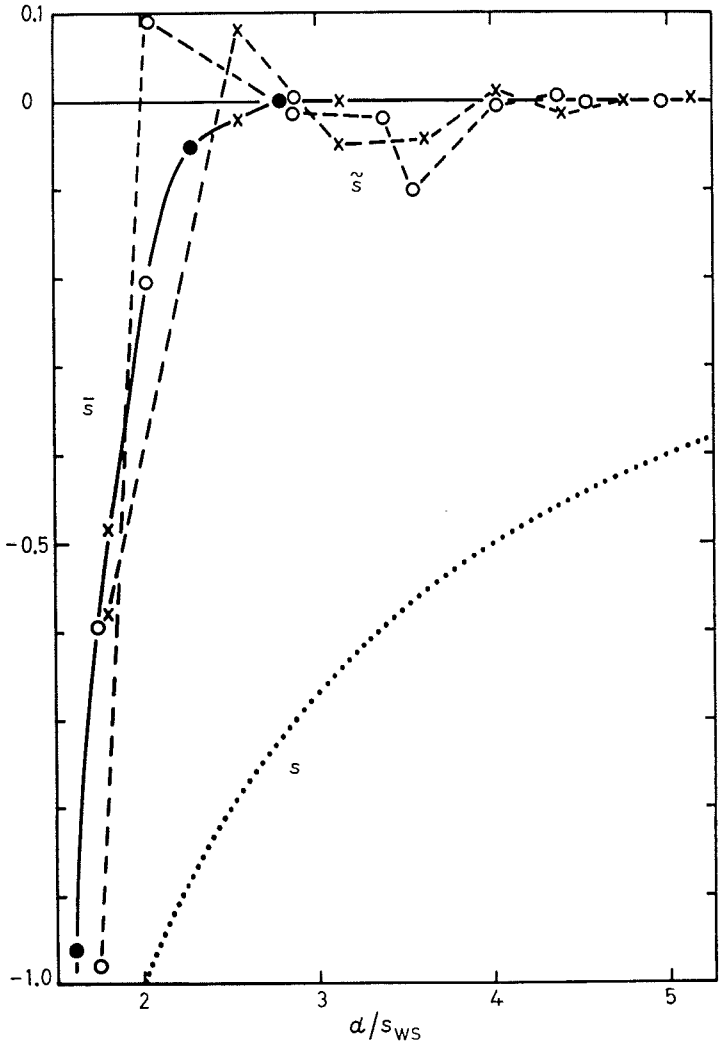

Fig. 5. – The bare (dotted), orthogonal (dashed) and most screened (full) $ss\sigma$ hopping integral as a function of the interatomic distance d in units of the Wigner-Seitz radius for the f.c.c. (×), b.c.c. (○) and s.c. (●) structures.

The monopole field, $\bar{K}_0(\boldsymbol{r})$ (52), screened on a b.c.c. lattice with the $\bar{Q}$-values for optimal screening (table I) is shown in fig. 6. The constant-$\bar{K}$ contours in fig. 6*a*) and *b*) are for the (001)- and (110)-planes, respectively. The (001)-plane contains the central atom and the second and third nearest neighbours, and the (110)-plane contains the central atom and the first, second and

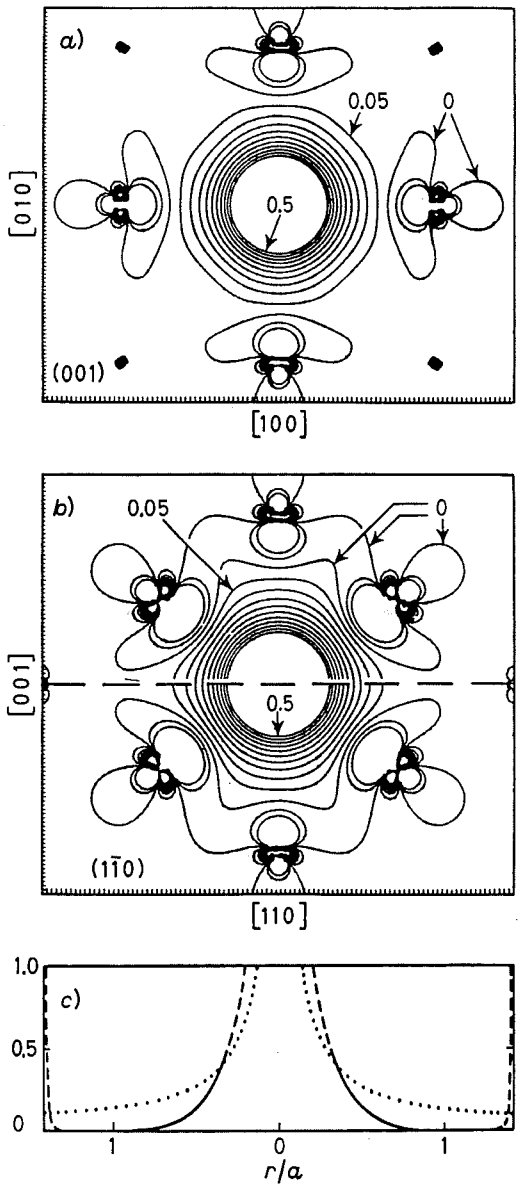

Fig. 6. – Screened monopole field, $\bar{K}_0(\boldsymbol{r})$, on a b.c.c. lattice. *a*) and *b*) show constant-$\bar{K}$ contours from — 0.1 to 0.5 in a (001) plane and a (110) plane, respectively. In *c*) the bare field (dotted) and the screened field (full and broken) are shown along the [110]-direction from the central atom and to the third nearest neighbour, *i.e.* along the dotted line in *b*).

third nearest neighbours. In fig. 6*c*) the bare $K_0(\boldsymbol{r})$ and the screened $\bar{K}_0(\boldsymbol{r})$ are plotted along the [110]-direction from the central atom and to the third nearest neighbour. The broken part of the curve in fig. 6*c*) indicates that the *s*-MTO will be obtained from the screened monopole field by augmentation inside atom-centred spheres such that the rapidly varying parts of the screened field will be substituted by linear combinations of the regular functions, phi and phi-dot.

TABLE I. – *Most localized canonical transfer matrix* $\overline{S}_{RL,0L'}$.

	$RL \backslash L'$	s	x	y	z	$3z^2-1$	x^2-y^2	yz	xz	xy	L'/RL	
f.c.c.												
on-site	$L = L'$	3.053	2.742	2.742	2.742	1.674	1.674	2.366	2.366	2.366		
		−0.484	−0.695	−0.695	0	0.663	0	0	0	−1.027	s	first nearest neighbour
			0.846	1.155	0	−0.946	−0.488	0	0	1.513	x	
				0.846	0	−0.946	0.488	0	0	1.513	y	$\boldsymbol{R} = \frac{1}{2}\begin{bmatrix} a \\ a \\ 0 \end{bmatrix}$
second nearest neighbour	s	−0.020			−0.200	0	0	−0.365	−0.365	0	z	
	x	0	0.003			−1.005	0	0	0	1.372	$3z^2-1$	
	y	0	0	0.003			1.546	0	0	0	x^2-y^2	
$\boldsymbol{R} = \begin{bmatrix} 0 \\ 0 \\ a \end{bmatrix}$	z	0.038	0	0	0.092			0.613	0.671	0	yz	
	$3z^2-1$	−0.062	0	0	−0.141	−0.226			0.613	0	xz	
	x^2-y^2	0	0	0	0	0	−0.011			−2.512	xy	
	yz	0	0	−0.006	0	0	0	−0.023				
	xz	0	−0.006	0	0	0	0	0	−0.023			
	xy	0	0	0	0	0	0	0	0	0.011		
b.c.c.												
on-site	$L = L'$	3.093	2.787	2.787	2.787	1.299	1.299	2.710	2.710	2.710		
		−0.593	−0.680	−0.680	−0.680	0	0	−0.818	−0.818	−0.818	s	first nearest neighbour
			0.548	0.904	0.904	0.275	−0.477	1.286	0.820	0.820	x	
				0.548	0.904	0.275	0.477	0.820	1.286	0.820	y	$\boldsymbol{R} = \frac{1}{2}\begin{bmatrix} a \\ a \\ a \end{bmatrix}$
second nearest neighbour	s	−0.203			0.548	−0.551	0	0.820	0.820	1.286	z	
	x	0	−0.048			1.218	0	0.386	0.386	−0.772	$3z^2-1$	
	y	0	0	−0.048			1.218	−0.669	0.669	0	x^2-y^2	
$\boldsymbol{R} = \begin{bmatrix} 0 \\ 0 \\ a \end{bmatrix}$	z	0.435	0	0	0.935			−0.981	−1.429	−1.429	yz	
	$3z^2-1$	−0.603	0	0	−1.289	−1.757			−0.981	−1.429	xz	
	x^2-y^2	0	0	0	0	0	−0.049			−0.981	xy	

	yz	0	0	0.134	0	0	0	0.364				
	xz	0	0.134	0	0	0	0	0	0.364			
	xy	0	0	0	0	0	0	0	0	0.016		
s.c. on-site	$L = L'$	3.724	3.713	3.713	3.713	5.888	5.888	1.423	1.423	1.423		
		−0.961	0	0	−1.839	−2.096	0	0	0	0	s	first nearest neighbour
			−0.756	0	0	0	0	0	−1.610	0	x	
				−0.756	0	0	0	−1.610	0	0	y	$\boldsymbol{R} = \begin{bmatrix} 0 \\ 0 \\ a \end{bmatrix}$
second nearest neighbour	s	−0.057			3.621	4.409	0	0	0	0	z	
	x	0.086	0.125			−6.168	0	0	0	0	$3z^2-1$	
$\boldsymbol{R} = \begin{bmatrix} a \\ a \\ 0 \end{bmatrix}$	y	0.086	0.130	0.125			−0.443	0	0	0	x^2-y^2	
	z	0	0	0	−0.054			3.517	0	0	yz	
	$3z^2-1$	0.041	0.061	0.061	0	−0.048			3.517	0	xz	
	x^2-y^2	0	−0.006	0.006	0	0	−0.071			−0.639	xy	
	yz	0	0	0	0.092	0	0	0.153				
	xz	0	0	0	0.092	0	0	0.141	0.153			
	xy	−0.151	−0.238	−0.238	0	0.121	0	0	0	−0.506		

$\overline{Q}_s = 0.3485$, $\overline{Q}_p = 0.05303$, $\overline{Q}_d = 0.010714$,
f.c.c.: $w = (16\pi/3)^{-1/3}a$, b.c.c.: $w = (8\pi/3)^{-1/3}a$, s.c.: $w = (4\pi/3)^{-1/3}a$.
$w \equiv$ Wigner-Seitz radius, $a \equiv$ lattice constant.
Note that $\overline{S}_{RL',0L} = (-)^{l+l'}\overline{S}_{RL,0L'}$

4·2. LMTO *Hamiltonians.* – We now perform this augmentation and thereby obtain explicit expressions for $\boldsymbol{h}$, or $\bar{\boldsymbol{h}}$ and $\bar{\boldsymbol{o}}$, in terms of the canonical quantities $\bar{\boldsymbol{S}}$ and $\bar{\boldsymbol{Q}}$ plus some parameters, C_{Rl}, Δ_{Rl} and Q_{Rl}, which together with the previously defined third-order parameter p_{Rl} (21) specify the spherically symmetric part of the potential.

We thus want to use $|\bar{K}\rangle^{\infty}$ (52) outside the augmentation spheres and $|\bar{\chi}\rangle^{\infty}$ (19) inside. Since both functions are expressed as one-centre angular-momentum expansions in, respectively, (19) and (50), the augmentation is reduced to a continuous and differentiable matching at all sphere radii, s_R. In this way each *radial* function

$$K_l(r) \equiv (r/w)^{-l-1} \tag{45}$$

and

$$\bar{J}_l(r) \equiv [2(2l+1)]^{-1}(r/w)^l - \bar{Q}_l(r/w)^{-l-1} \tag{49}$$

should be matched to a linear combination of $\varphi_{Rl}(r)$ and $\dot{\varphi}_{Rl}(r)$. The two latter functions, we remember, were obtained by numerical solution of the appropriate radial Schrödinger equation at the energies E_ν and $E_\nu + \mathrm{d}E_\nu$ and by subsequent normalization in the sphere (see (7), (8), (13) and (14)). The standard expression for the matching of a function, $f(r)$, to a linear combination of two given functions, $a(r)$ and $b(r)$, is

$$f(r) \to [a(r)\,W\{f,b\} - b(r)\,W\{f,a\}]\,W\{a,b\}^{-1}\,, \tag{53}$$

where

$$W\{a,b\} \equiv s^2[a(s)b'(s) - a'(s)b(s)] = sa(s)b(s)[D\{b\} - D\{a\}] \tag{54}$$

is the Wronskian and D is the radial logarithmic derivative defined in (18).

The Wronskian of phi-dot and phi may be obtained from (13), (24) and Green's second identity, *i.e.*

$$1 = \langle\varphi^2\rangle = \langle\varphi|-\nabla^2 + V - E_\nu|\dot{\bar{\varphi}}\rangle = W\{\dot{\bar{\varphi}},\varphi\}\,. \tag{55}$$

This holds for any phi-bar-dot as given by (17) because $W\{\varphi,\varphi\} = 0$. Here and in the following we often drop the subscripts Rl. For the radial solutions of the Laplace equation we have

$$W\{K,\bar{J}\} = W\{K,J\} = w/2\,, \tag{56}$$

where the definition (49) of $\bar{J}$ has been used.

Since the tail of the multipole field (50) is expanded in $\bar{J}$-functions only, and the tail of the MTO (19) is expanded in $\dot{\bar{\varphi}}$-functions only, these two radial

functions, for the same Rl, must have identical logarithmic derivatives at their sphere radius. This means that, with $\bar{Q}$ given, $\bar{J}(r)$ is specified by (49) and $\dot{\bar{\varphi}}(r)$ is specified by (17a) with

$$\bar{o} = -\frac{W\{\bar{J}, \dot{\varphi}\}}{W\{\bar{J}, \varphi\}} = -\frac{W\{J, \dot{\varphi}\} - W\{K, \dot{\varphi}\}\bar{Q}}{W\{J, \varphi\} - W\{K, \varphi\}\bar{Q}}. \tag{57}$$

This has been derived from (53) with $a(r) \equiv \dot{\varphi}(r)$ and $b(r) = \varphi(r)$.

The relation between $\bar{Q}$ and the logarithmic derivative of $\dot{\bar{\varphi}}(r)$, which equals the logarithmic derivative of $\bar{J}(r)$, is obtained from (49) by forming $W\{\bar{J}, \dot{\bar{\varphi}}\} = 0$, *viz.*

$$\bar{Q} = \frac{W\{J, \dot{\bar{\varphi}}\}}{W\{K, \dot{\bar{\varphi}}\}} = \frac{(s/w)^{2l+1}}{2(2l+1)} \frac{D\{\dot{\bar{\varphi}}\} - l}{D\{\dot{\bar{\varphi}}\} + l + 1}. \tag{58}$$

Having obtained the matrix elements of the diagonal matrix $\bar{\mathbf{o}}$, we may now obtain the matrix elements of $\bar{\boldsymbol{h}}$ in the following way. From (53) with $a(r) \equiv \dot{\bar{\varphi}}(r)$ and $b(r) \equiv \varphi(r)$ we find

$$\bar{J}(r) \to \dot{\bar{\varphi}}(r)\, W\{\bar{J}, \varphi\} \quad \text{and} \quad K(r) \to \dot{\bar{\varphi}}(r)\, W\{K, \varphi\} - \varphi(r)\, W\{K, \dot{\bar{\varphi}}\}. \tag{59}$$

The augmented multipole field (50) thus has the one-centre expansions

$$|\bar{\boldsymbol{K}}\rangle^{\infty} \to -|\boldsymbol{\varphi}\rangle\, \boldsymbol{W}\{K, \dot{\bar{\varphi}}\} - |\dot{\bar{\boldsymbol{\varphi}}}\rangle[-\boldsymbol{W}\{K, \varphi\} + \boldsymbol{W}\{\bar{J}, \varphi\}\bar{\boldsymbol{S}}], \tag{60}$$

where the $\boldsymbol{W}$'s are diagonal matrices and where, according to (59) and (56),

$$W\{K, \dot{\bar{\varphi}}\}\, W\{\bar{J}, \varphi\} = w/2. \tag{61}$$

By comparison with the one-centre expansions (19) for the MTO we finally see that

$$|\bar{K}_{RL}\rangle^{\infty} \to -|\bar{\chi}_{RL}\rangle^{\infty} W_{Rl}\{K, \dot{\bar{\varphi}}\} \equiv |\bar{\chi}_{RL}\rangle^{\infty} (2\bar{\Delta}_{Rl}/w)^{-\frac{1}{2}} \tag{62}$$

and that

$$\bar{\boldsymbol{H}}^{(1)} \equiv \boldsymbol{E}_\nu + \bar{\boldsymbol{h}} = \tag{63}$$

$$= \boldsymbol{E}_\nu - \frac{\boldsymbol{W}\{K, \varphi\}}{\boldsymbol{W}\{K, \dot{\bar{\varphi}}\}} + \left(\frac{2}{w}\right)^{\frac{1}{2}} \boldsymbol{W}\{\bar{J}, \varphi\}\, \bar{\boldsymbol{S}}\, \boldsymbol{W}\{\bar{J}, \varphi\} \left(\frac{2}{w}\right)^{\frac{1}{2}} \equiv \bar{\boldsymbol{C}} + \bar{\boldsymbol{\Delta}}^{\frac{1}{2}} \bar{\boldsymbol{S}} \bar{\boldsymbol{\Delta}}^{\frac{1}{2}},$$

where $\bar{\boldsymbol{C}}$ and $\bar{\boldsymbol{\Delta}}$ are diagonal matrices.

From this derivation it is obvious that the LMTO formulae given above are valid for any choice of $\bar{Q}$'s, provided that the corresponding $\bar{\boldsymbol{S}}$ (51) has

no poles. We might specifically choose [39] $\bar{Q}$ equal to

$$\frac{W\{J,\dot{\varphi}\}}{W\{K,\dot{\varphi}\}} = \frac{(s/w)^{2l+1}}{2(2l+1)} \frac{D\{\dot{\varphi}\}-l}{D\{\dot{\varphi}\}+l+1} \equiv Q \tag{64}$$

such that the corresponding o given by (57) vanishes, or, in other words, such that $\dot{\tilde{\varphi}}(r) = \dot{\varphi}(r)$. The corresponding second-order Hamiltonian is

$$\begin{aligned} \boldsymbol{H}^{(2)} &\equiv \boldsymbol{E}_\nu + \boldsymbol{h} = \\ &= \boldsymbol{E}_\nu - \frac{\boldsymbol{W}\{K,\dot{\varphi}\}}{\boldsymbol{W}\{K,\dot{\varphi}\}} + \left(\frac{2}{w}\right)^{\frac{1}{2}} \boldsymbol{W}\{\tilde{J},\varphi\}\, \tilde{\boldsymbol{S}}\, \boldsymbol{W}\{\tilde{J},\varphi\} \left(\frac{2}{w}\right)^{\frac{1}{2}} \equiv \boldsymbol{C} + \boldsymbol{\Delta}^{\frac{1}{2}}\, \tilde{\boldsymbol{S}}\, \boldsymbol{\Delta}^{\frac{1}{2}} \end{aligned} \tag{65}$$

with $|\tilde{\boldsymbol{J}}\rangle \equiv |\boldsymbol{J}\rangle - |\boldsymbol{K}\rangle \boldsymbol{Q}$ and, from (61), $\boldsymbol{W}\{\tilde{J},\varphi\} = (w/2)\, \boldsymbol{W}\{K,\dot{\varphi}\}^{-1}$. Moreover,

$$\tilde{\boldsymbol{S}} \equiv \boldsymbol{S}[\boldsymbol{I} - \boldsymbol{Q}\boldsymbol{S}]^{-1} = \bar{\boldsymbol{S}}[\boldsymbol{I} - (\boldsymbol{Q} - \bar{\boldsymbol{Q}})\, \bar{\boldsymbol{S}}]^{-1}. \tag{66}$$

(Note that the unbarred $\boldsymbol{\chi}$, $\boldsymbol{h}$, $\boldsymbol{H}$, $\boldsymbol{O}$, $\boldsymbol{Q}$ and $\boldsymbol{o} \equiv 0$, as well as $\tilde{\boldsymbol{S}}$ with a tilde correspond to the orthogonal phi-dot, while the unbarred $\boldsymbol{S}$ corresponds to the regular $J(r)$-function and hence to the choice $\bar{\boldsymbol{Q}} = 0$.) Equations (65) and (66) are among the most important of the present lecture. Equivalent with these are eqs. (63) and

$$\boldsymbol{H}^{(2)} = \boldsymbol{E}_\nu + \bar{\boldsymbol{h}}(\boldsymbol{I} + \bar{\boldsymbol{o}}\bar{\boldsymbol{h}})^{-1}, \tag{28}$$

derived in sect. **3**.

4·3. *Potential parameters.* – In (63) and (65) we have introduced the common notation for the first potential parameter

$$\bar{C} \equiv E_\nu - W\{K,\varphi\}/W\{K,\dot{\bar{\varphi}}\} = E_\nu - (2/w)\, W\{K,\varphi\}\, W\{\bar{J},\varphi\}, \tag{67}$$

which determines the *position* of the « Rl band », and the second potential parameter

$$\bar{\Delta}^{\frac{1}{2}} \equiv -(2/w)^{\frac{1}{2}} W\{\bar{J},\varphi\} = -(w/2)^{\frac{1}{2}} W\{K,\dot{\bar{\varphi}}\}^{-1}, \tag{68}$$

which determines the *width* and *hybridization strength* of the « Rl band ». Here, again, the subscripts Rl have been dropped.

The meaning of these potential parameters may be illustrated by writing (53), with $a(r) \equiv \dot{\bar{\varphi}}(r)$, $b(r) \equiv \varphi(r)$ and $f(r) \equiv K(r)$, as

$$\begin{aligned} K(r) \to &- W\{K,\dot{\bar{\varphi}}\}[\varphi(r) - \dot{\bar{\varphi}}(r)\, W\{K,\varphi\}/W\{K,\dot{\bar{\varphi}}\}] = \\ &= (\tfrac{1}{2} w/\bar{\Delta})^{\frac{1}{2}} [\varphi(r) + (\bar{C} - E_\nu)\, \dot{\bar{\varphi}}(r)] \approx [K(s)/\bar{\varphi}(C,s)]\, \bar{\varphi}(C,r). \end{aligned} \tag{69}$$

This shows that $\bar{C}$ is the energy, to first order in its deviation from E_ν, for which the radial solution of Schrödinger's equation matches onto $K(r)$ or, in other words, the energy for which the logarithmic derivative function

$$D(E) \equiv D\{\varphi(E)\} \equiv \partial \ln \varphi(E, r)/\partial \ln r|_s \tag{70}$$

takes the value $-l-1$. Equation (69), furthermore, shows that $\bar{\Delta}^{\frac{1}{2}}$ is proportional to the amplitude of the corresponding radial wave function at the average Wigner-Seitz radius of the lattice, w. Specifically,

$$\bar{\Delta}^{\frac{1}{2}} \approx (w/2)^{\frac{1}{2}}\bar{\varphi}(C, s)/K(s) \approx (w/2)^{\frac{1}{2}}\bar{\varphi}(C, w)\,. \tag{71}$$

If $\bar{Q}$ is chosen independently of the potential, as is usually the case, then (67) and (68) demonstrate that $\bar{C}$ and $\bar{\Delta}$, and thereby $\bar{\boldsymbol{H}}^{(1)}$, only depend on $\varphi(s)$ and $D\{\varphi\}$, but not on $D\{\dot{\varphi}\}$ (which is related to $\dot{\varphi}(s)$ through (55)). In this case the information about the energy derivative function is carried solely by $\bar{o}$, as seen from (57). This is consistent with the often-mentioned fact that in the ASA $\bar{\boldsymbol{H}}^{(1)}$ is the Hamiltonian correct to first order, while $\boldsymbol{H}^{(2)}$ is the Hamiltonian correct to second order. If $\bar{Q}$ is chosen according to (64), it becomes equivalent with $D\{\dot{\varphi}\}$, and the corresponding C and Δ, and thus $\bar{\boldsymbol{H}}^{(2)}$, then depend not only on $\varphi(s)$ and $D\{\varphi\}$, but also on $D\{\dot{\varphi}\}$. Moreover, C becomes the energy for which $\varphi(E, r)$ has the logarithmic derivative $-l-1$ at the sphere to order $(C-E_\nu)^2$, and $\Delta^{\frac{1}{2}}$ becomes the value $(w/2)^{\frac{1}{2}} \cdot \varphi(C, w)$, to order $C-E_\nu$.

To provide a better feeling for these potential parameters, we mention that for electrons free with respect to some flat potential V, and for $E_\nu \equiv C$,

$$\begin{cases} C_s - V = (\pi/2)^2 s^{-2} \approx 2.47 s^{-2}\,, \\ C_p - V = \pi^2 s^{-2} \approx 9.87 s^{-2}\,, \\ C_d - V \approx 20.19 s^{-2}\,. \end{cases} \tag{72}$$

Moreover, for free electrons and $E_\nu \equiv C$, the potential parameter

$$\mu \equiv (s/w)^{2l+1}(\Delta s^2)^{-1} \approx 2[s^3\varphi(C, s)^2]^{-1} \tag{73}$$

equals unity for all l. The parameter μ is thus named the *intrinsic band mass*, relative to that of a free electron. Equation (72) and the value unity for (73) in the case of free electrons may be derived [5, 6] from the recursion relations for the spherical Bessel functions.

The third potential parameter Q defined in (64) may, from (69) and the

analogous expression for $J(r)$, be interpreted as the ratio [39]

$$Q = \frac{J(s)}{K(s)} \frac{\varphi(s) + (C - E_\nu)\dot{\varphi}(s)}{\varphi(s) + (V - E_\nu)\dot{\varphi}(s)} \approx \frac{1}{2(2l+1)} \frac{\varphi(C, w)}{\varphi(V, w)}, \tag{74}$$

where V is now the energy for which the logarithmic derivative (70) of $\varphi(E, r)$ at the sphere takes the value l. For free electrons, and for $E_\nu \equiv V$, we find [5, 6] $D\{\dot{\varphi}\} = 3l + 5$, and consequently

$$Q = (s/w)^{2l+1} \frac{2l+5}{4(2l+1)(2l+3)} \approx \left(\frac{s}{w}\right)^{2l+1} \times \begin{cases} 0.42 & \text{for } l = 0, \\ 0.11 & \text{for } l = 1, \\ 0.064 & \text{for } l = 2, \end{cases} \tag{75}$$

while, for $E_\nu \equiv C$,

$$Q_{s,p,d} \approx 0.40(s/w),\ 0.09(s/w)^3 \text{ and } 0.038(s/w)^5 . \tag{76}$$

In order to provide a feeling for the size of the « perturbation $Q - \bar{Q}$ in Dyson's equation » (66) we refer to table I giving the most localized structure matrix and the corresponding $\bar{Q}$-values:

$$\bar{Q}_{s,p,d} = 0.3485,\ 0.053\,03,\ 0.010\,714 \quad \text{and} \quad \bar{Q}_l = 0 \quad \text{for } l \geqslant 3 . \tag{77a}$$

The many decimal places given here do not indicate that the localization of $\overline{\mathbf{S}}$ depends sensitively on the exact values of the $\bar{Q}$'s, but, rather, the values (77*a*) correspond to the logarithmic derivative values

$$D_{s,p,d}\{\dot{\bar{\varphi}}\}_{s=w} = 2.3, 2.4, 2.6 \quad \text{and} \quad D_l\{\dot{\bar{\varphi}}\}_{s=w} = l \quad \text{for } l \geqslant 3 , \tag{77b}$$

which were the parameters actually used in the numerical calculation [13] of $\overline{\mathbf{S}}$. We prefer to give $\bar{Q}$ rather than $D\{\dot{\bar{\varphi}}\} \equiv D\{\bar{J}\}$ because the former are independent of the sphere radii.

The fourth potential parameter is p defined in (21). It may be shown that $p^{-\frac{1}{2}}$ is the size of the *energy window* inside which a linear method is supposed to yield realistic results. For free electrons, and with $E_\nu \equiv C$, it may be shown [5, 6] that

$$p_{s,p,d}^{-\frac{1}{2}} \approx 18s^{-2},\ 27s^{-2} \text{ and } 35s^{-2}, \tag{78}$$

which, for a typical s-value of 3 Bohr radii, become 1.8, 2.7 and 3.5 Ryd.

For broad, free-electron–like bands it is customary instead of C to use a potential parameter, V, which is named the *square-well pseudopotential*. For a monoatomic solid, and in the ASA, V_s is the bottom of the s-band (if $E_\nu \approx V_s$). For free electrons all V_{Rl}'s are equal and denote the bottom of the

band. The potential parameter V thus equals the energy for which $\varphi(V, r)$ matches onto to a spherical Bessel function with $\varkappa$ zero, *i.e.* the energy for which the logarithmic derivative function (70) equals l. The definition of $\overline{V}$ is, therefore, analogous to (67):

$$\overline{V} \equiv E_\nu - W\{J, \varphi\}/W\{J, \dot{\bar{\varphi}}\}\,, \tag{79}$$

and $\overline{V}$ may be obtained from the values of $\overline{C}$, $\overline{\Delta}$ and $\overline{Q}$ using the relation

$$\overline{C} - \overline{V} = \overline{\Delta}/\overline{Q}\,. \tag{80}$$

The latter is proved by substitution of (49) and (58) in (79) and by making use of (68):

$$\overline{C} - \overline{V} = \frac{W\{J, \varphi\}}{W\{J, \dot{\bar{\varphi}}\}} - \frac{W\{K, \varphi\}}{W(K, \dot{\bar{\varphi}}\}} = \frac{W\{\bar{J}, \varphi\} + W\{K, \varphi\}\overline{Q}}{W\{K, \dot{\bar{\varphi}}\}\overline{Q}} - \frac{W\{K, \varphi\}}{W\{K, \dot{\bar{\varphi}}\}} =$$

$$= W\{\bar{J}, \varphi\}[W\{K, \dot{\bar{\varphi}}\}\overline{Q}]^{-1} = \overline{\Delta}/\overline{Q}\,.$$

The width parameter analogous to $\overline{\Delta}$ (68) is defined by

$$\overline{\Gamma}^{\frac{1}{2}} \equiv -(w/2)^{\frac{1}{2}} W\{J, \dot{\bar{\varphi}}\}^{-1} \approx 2(2l+1)(w/2)^{\frac{1}{2}}\,\tilde{\varphi}(V, w) \tag{81}$$

and, if, again, we use (49) and (58), we realize that

$$\overline{\Gamma}^{\frac{1}{2}} = -(w/2)[W\{K, \dot{\bar{\varphi}}\}\overline{Q}]^{-1} = \overline{\Delta}^{\frac{1}{2}}/\overline{Q}\,. \tag{82}$$

The parameter giving the *intrinsic band mass* near V is

$$\tau \equiv 2(2l+1)^2(2l+3)(w/s)^{2l+1}(\Gamma s^2)^{-1} \approx (2l+3)[s^3\varphi(V, s)^2]^{-1} \tag{83}$$

and, for a flat potential of value V, it equals unity for all l.

The first- and second-order Hamiltonians (63) and (65) may be expressed in terms of the potential parameters $\overline{V}$ and $\overline{\Gamma}$ instead of $\overline{C}$ and $\overline{\Delta}$. The results obtained using (80) and (82) are

$$\overline{\boldsymbol{H}}^{(1)} = \overline{\boldsymbol{V}} + \overline{\boldsymbol{\Gamma}}^{\frac{1}{2}}(\overline{\boldsymbol{Q}}^{-1} - \boldsymbol{S})^{-1}\overline{\boldsymbol{\Gamma}}^{\frac{1}{2}} \tag{84}$$

and

$$\boldsymbol{H}^{(2)} = \boldsymbol{V} + \boldsymbol{\Gamma}^{\frac{1}{2}}(\boldsymbol{Q}^{-1} - \boldsymbol{S})^{-1}\boldsymbol{\Gamma}^{\frac{1}{2}}\,. \tag{85}$$

4·4. *Transformation to the nearly orthogonal set of* LMTOs *from the canonical most localized set.* – In order to construct $\boldsymbol{H}^{(2)}$ from (65) we need the Q-dependent structure matrix $\tilde{\boldsymbol{S}}$ which can be constructed from either of the two

canonical matrices, the bare $\boldsymbol{S}$ or the localized $\overline{\boldsymbol{S}}$, through the matrix inversion implied by (66). For a crystal we, of course, use the Bloch representation

$$\bar{S}^{k}_{\boldsymbol{R}'L',\boldsymbol{R}L} = \sum_{\boldsymbol{T}} \exp\left[i\boldsymbol{k}\cdot\boldsymbol{T}\right]\bar{S}_{\boldsymbol{R}'L',(\boldsymbol{R}+\boldsymbol{T})L}\,, \tag{86}$$

in which the structure matrix is diagonal and the inversion (66) involves finite matrices only. The typical dimension is $9M\times 9M$, where M is the number of atoms per primitive cell. In (86) $\boldsymbol{T}$ are the lattice translations and $\boldsymbol{R}$ and $\boldsymbol{R}'$ label the atoms in the primitive cell. For the bare structure matrix the lattice summations (86) require use of the Ewald technique [3, 10].

An alternative procedure which may also be used in real space and does not require translational symmetry is to expand $\tilde{\boldsymbol{S}}$ like

$$\tilde{\boldsymbol{S}} = \overline{\boldsymbol{S}} + \overline{\boldsymbol{S}}(\boldsymbol{Q}-\overline{\boldsymbol{Q}})\,\overline{\boldsymbol{S}} + \overline{\boldsymbol{S}}(\boldsymbol{Q}-\overline{\boldsymbol{Q}})\,\overline{\boldsymbol{S}}(\boldsymbol{Q}-\overline{\boldsymbol{Q}})\,\overline{\boldsymbol{S}} + \ldots\,, \tag{87}$$

but this requires that the series be carried to convergence and, hence, that $(\boldsymbol{Q}-\overline{\boldsymbol{Q}})\,\overline{\boldsymbol{S}}$ be much smaller than unity.

The best procedure is to start from $\bar{\boldsymbol{h}}$ given by (63) rather than from $\boldsymbol{h}$ and to expand (28) like

$$\boldsymbol{H}^{(2)} = \overline{\boldsymbol{H}}^{(1)} - \overline{\boldsymbol{h}\boldsymbol{o}}\,\overline{\boldsymbol{h}} + \overline{\boldsymbol{h}\boldsymbol{o}}\,\overline{\boldsymbol{h}\boldsymbol{o}}\,\overline{\boldsymbol{h}} - \ldots\,. \tag{88}$$

The superiority of this method arises from the fact that $\overline{\boldsymbol{H}}^{(1)}$ alone delivers one-electron energies correct to first order in $E_j - E_\nu$, such that the inclusion of more and more terms in (88) merely increases the accuracy further and further away from E_ν. The series need, therefore, not be carried to convergence. Since, in any case, the final result of a linear method, employing (33) for instance, is correct to order $(\boldsymbol{h}\boldsymbol{p}^{\frac{1}{2}})^3_{jj}$ only, there is no reason to go beyond third order in (88) unless $(\overline{\boldsymbol{h}\boldsymbol{o}})_{jj}$ is considerably larger than $(\boldsymbol{h}\boldsymbol{p}^{\frac{1}{2}})_{jj}$. As an example we show in fig. 7 the total and the s-, p- and d-projected densities of states for b.c.c. iron calculated in the ASA and without spin polarization. The potential parameters may be found in table III and the values of particular interest at the moment are $E_{\nu s,p,d} = -0.47$, -0.33 and -0.26 Ryd, $\tilde{o}^{-1}_{s,p,d} = -2.1$, -1.7 and 1.5 Ryd, and $p^{-\frac{1}{2}}_{s,p,d} = 5.1$, 6.6 and 0.8 Ryd. Figure 7*a*) shows the result of diagonalizing the tight-binding first-order Hamiltonian $\overline{\boldsymbol{H}}^{(1)}$ and fig. 7*e*) shows the result of diagonalizing the «fully Löwdin-orthogonalized Hamiltonian »

$$(\overline{\boldsymbol{O}}^{-\frac{1}{2}})^{\dagger}\,\overline{\boldsymbol{H}\boldsymbol{O}}^{-\frac{1}{2}} = \boldsymbol{O}^{-\frac{1}{2}}\boldsymbol{H}\boldsymbol{O}^{-\frac{1}{2}} \approx [\boldsymbol{I} - \boldsymbol{h}\boldsymbol{p}\boldsymbol{h}/2][\boldsymbol{H}^{(2)} + \boldsymbol{h}\boldsymbol{E}_\nu\boldsymbol{p}\boldsymbol{h}][\boldsymbol{I} - \boldsymbol{h}\boldsymbol{p}\boldsymbol{h}/2] \equiv \boldsymbol{H}^{(3)}\,. \tag{89}$$

This is obtained from (29) and (30) and is correct to all orders in $\overline{\boldsymbol{h}\boldsymbol{o}}$ and to order $(\boldsymbol{h}\boldsymbol{p}^{\frac{1}{2}})^3$. In fig. 7*b*), *c*) and *d*) we show the s- and p-projected densities of states obtained by diagonalizing, respectively, $\overline{\boldsymbol{H}}^{(1)} - \overline{\boldsymbol{h}\boldsymbol{o}}\,\overline{\boldsymbol{h}}$, the three first

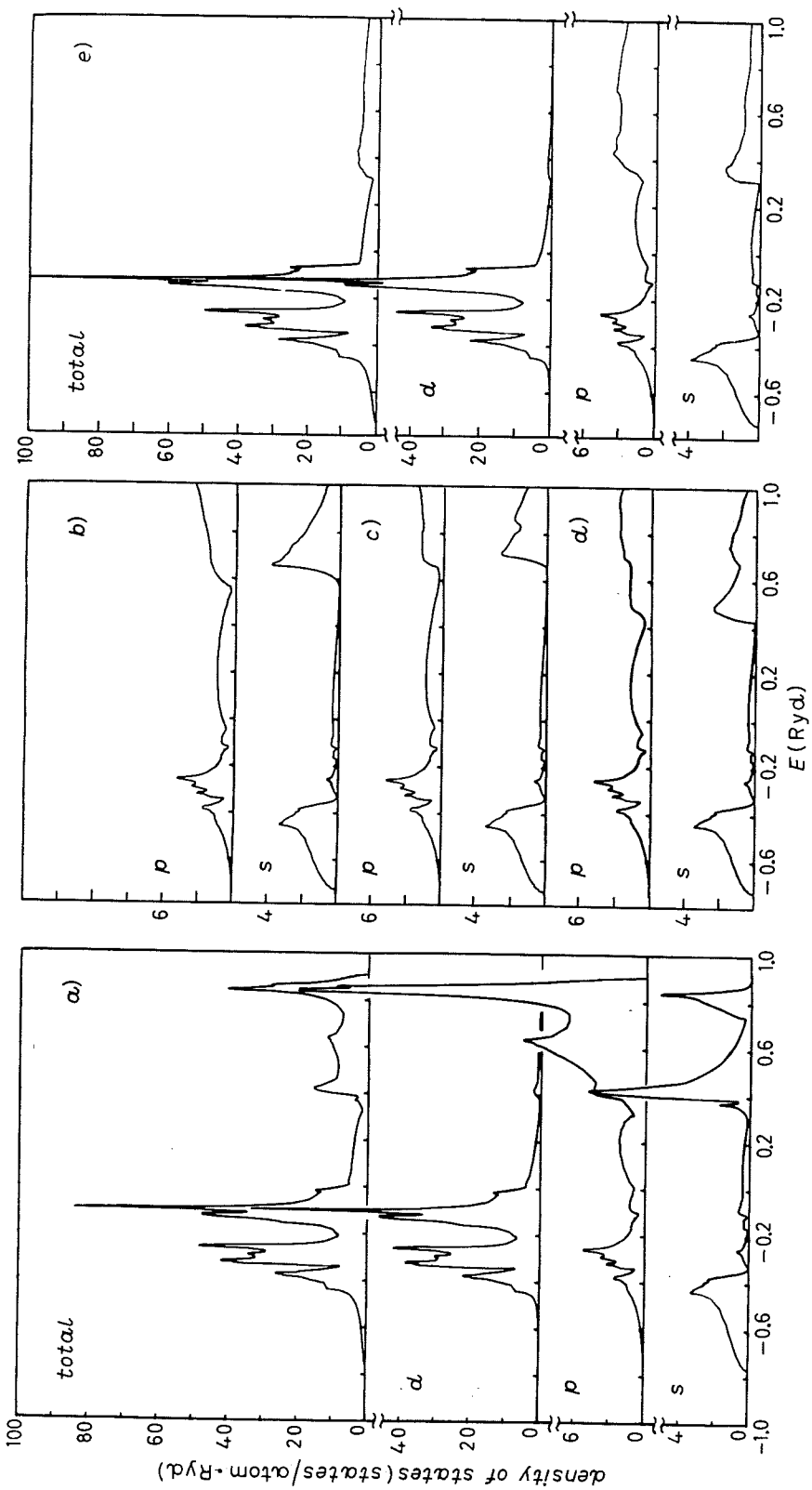

Fig. 7. – Total and partial densities of states for paramagnetic b.c.c. iron in the ASA and with the potential parameters in table III. *a*) is for the first-order Hamiltonian, $\overline{\boldsymbol{H}}^{(1)}$ (63); *b*) and *e*) are for the first two and three terms in eq. (88): $\overline{\boldsymbol{H}}^{(1)} - \overline{\boldsymbol{h}}\overline{\boldsymbol{o}}\boldsymbol{h}$ and $\overline{\boldsymbol{H}}^{(1)} - \overline{\boldsymbol{h}}\overline{\boldsymbol{o}}\boldsymbol{h} + \overline{\boldsymbol{h}}\overline{\boldsymbol{o}}\boldsymbol{h}\overline{\boldsymbol{o}}\boldsymbol{h}$, respectively; *d*) is for the second-order Hamiltonian, $\boldsymbol{H}^{(2)}$ (65), plus third-order correction (33) and *e*) is for the Löwdin-orthogonalized Hamiltonian, $\boldsymbol{H}^{(3)}$ (89).

terms of (88) and $\boldsymbol{H}^{(2)}$ given by (65) plus subsequent third-order corrections of the energy bands by means of (33). It may be seen that in the case of iron, and with the E_ν's used, the densities of states in the occupied part of the band, *i.e.* up to about $E_F \approx -0.125$ Ryd, are given reasonably well even in the tight-binding first-order approximation *a*). However, the high-lying parts of the *s*- and *p*-bands are considerably compressed, but, of course, an additional first-order calculation with E_ν's chosen around 0.5 Ryd could have yielded good results in that energy region [40]. A procedure based on (89) but with $\boldsymbol{H}^{(2)}$ given by (88) has been used [41] in connection with the *real-space* recursion method [42] to calculate the electronic structure of amorphous metals.

If we wish to use (88), we need to construct $\overline{\boldsymbol{h}}$ from (63) and $\overline{\boldsymbol{o}}$ from (57) and, hence, formulae for deriving $\bar{C}$, $\bar{\Delta}$ and $\bar{o}$ from the standard potential parameters C, Δ and Q, which are the ones usually given (and the ones that we shall list in tables III and IV).

From eqs. (67) and (68)

$$\frac{\bar{C}-E_\nu}{\bar{\Delta}^{\frac{1}{2}}} = (2/w)^{\frac{1}{2}} W\{K,\varphi\} = \frac{C-E_\nu}{\Delta^{\frac{1}{2}}}$$

and from this plus eqs. (68) and (49) we obtain

$$\bar{\Delta}^{\frac{1}{2}} - \Delta^{\frac{1}{2}} = (2/w)^{\frac{1}{2}} W\{K,\varphi\}(\bar{Q}-Q) = (\bar{Q}-Q)(C-E_\nu)\Delta^{-\frac{1}{2}}\,.$$

The relations needed are, therefore,

$$\frac{\bar{\Delta}^{\frac{1}{2}}}{\Delta^{\frac{1}{2}}} = 1-(Q-\bar{Q})\,\frac{C-E_\nu}{\Delta} = \frac{\bar{C}-E_\nu}{C-E_\nu}\,. \tag{90}$$

The expression for $\bar{o}$ in terms of C, Δ, Q and $\bar{Q}$ may be obtained from (57) and (64), plus (67) and (68) without bars. The result is

$$\frac{1}{\bar{o}} = C-E_\nu-\frac{\Delta}{Q-\bar{Q}}\,, \qquad \text{or} \qquad \bar{o} = -\frac{Q-\bar{Q}}{(\Delta\bar{\Delta})^{\frac{1}{2}}}\,. \tag{91}$$

4·5. *Exact tail cancellation, the screened* KKR-ASA *equations and the picture of Wigner and Seitz.* – It is a characteristic feature of the linear methods that the wave function (32) is given, on the one hand, as a multicentre expansion of energy-independent orbitals and, on the other hand, as a one-centre expansion of energy-dependent partial waves. The latter in fact holds to second, and not merely to first, order in $E-E_\nu$. This we prove in the present and following subsections by use of exact, energy-dependent muffin-tin orbitals constructed by augmentation of the multipole field (52) by linear combinations of $\varphi(E,r)$ and $\dot{\varphi}(E,r)$. We thus allow E_ν to vary and obtain

the energy-dependent MTO from (59)-(63) by substitution of E for E_ν. As a result

$$|\bar{\chi}(E)\rangle^{\infty} = |\varphi(E)\rangle + |\dot{\bar{\varphi}}(E)\rangle\,\bar{h}(E) + |\bar{\chi}(E)\rangle^{\mathrm{i}} \tag{92}$$

with

$$\bar{h}(E) = \left(\frac{2}{w}\right)^{\frac{1}{2}} W\{\bar{J}, \varphi(E)\}\left[-\frac{W\{K, \varphi(E)\}}{W\{\bar{J}, \varphi(E)\}} + \bar{S}\right] W\{\bar{J}, \varphi(E)\}\left(\frac{2}{w}\right)^{\frac{1}{2}} \equiv \tag{93}$$

$$\equiv [\dot{\bar{P}}(E)]^{-\frac{1}{2}}[-\bar{P}(E) + \bar{S}][\dot{\bar{P}}(E)]^{-\frac{1}{2}}\,.$$

The elements of the diagonal matrix $\bar{P}(E)$ are the (screened) *potential functions*

$$\bar{P}(E) \equiv \frac{W\{K, \varphi(E)\}}{W\{\bar{J}, \varphi(E)\}} = \frac{W\{K, \varphi(E)\}}{W\{J, \varphi(E)\} - W\{K, \varphi(E)\}\bar{Q}} = \frac{P(E)}{1 - \bar{Q}P(E)} \tag{94}$$

with

$$P(E) \equiv \frac{W\{K, \varphi(E)\}}{W\{J, \varphi(E)\}} = 2(2l+1)\left(\frac{w}{s}\right)^{2l+1}\frac{D(E) + l + 1}{D(E) - l} \tag{95}$$

being the potential functions as they are normally defined. Apart from normalization factors, (95) equals the cotangent of the phase shift in the limit of vanishing $\varkappa$. That

$$[\dot{\bar{P}}(E)]^{\frac{1}{2}} \equiv -(w/2)^{\frac{1}{2}} W\{\bar{J}, \varphi(E)\}^{-1} = \bar{\Delta}(E)^{-\frac{1}{2}} \tag{96}$$

is the square root of the energy derivative of the potential function follows from

$$\dot{\bar{P}}(E) = \frac{W\{K, \dot{\bar{\varphi}}(E)\}\,W\{\bar{J}, \varphi(E)\} - W\{\bar{J}, \dot{\bar{\varphi}}(E)\}\,W\{K, \varphi(E)\}}{W\{\bar{J}, \varphi(E)\}^2} = \tag{97}$$

$$= \frac{w/2}{W\{\bar{J}, \varphi(E)\}^2}\,.$$

(Note that P without a bar corresponds to the regular, unbarred $J(r)$-function and, hence, to the choice $\bar{Q} = 0$. To a general choice of $\bar{Q}$ corresponds $\bar{P}$, and to the special choice $\bar{Q} \equiv Q$ corresponds $\tilde{P}$. This convention for the potential function is thus the same as for the structure matrix.)

We may now form a linear combination of exact MTOs

$$|\bar{\chi}(E)\rangle^{\infty}\boldsymbol{u}(E) = |\varphi(E)\rangle\,\boldsymbol{u}(E) + |\dot{\bar{\varphi}}(E)\rangle\,\bar{h}(E)\,\boldsymbol{u}(E) + |\bar{\chi}(E)\rangle^{\mathrm{i}}\boldsymbol{u}(E) \tag{98}$$

(where $\boldsymbol{u}(E)$ is a column vector) and ask whether we can determine the energy, E, and the corresponding coefficients, $\boldsymbol{u}(E)$, such that the continuously differentiable function (98) is a solution of Schrödinger's equation for that energy.

In the ASA, where the $\varphi(E, \boldsymbol{r})$ *are* the exact solutions inside the spheres and where we neglect the interstitial region, (98) is the exact solution when, inside each sphere and for all partial waves, the sum of the « tails » $|\dot{\bar{\varphi}}(E)\rangle \bar{\boldsymbol{h}}(E)\, \boldsymbol{u}(E)$ cancels and we are left with the one-centre expansions

$$|\bar{\chi}(E)\rangle^{\infty}\, \boldsymbol{u}(E) = |\varphi(E)\rangle\, \boldsymbol{u}(E) = |\psi(E)\rangle\,. \tag{99}$$

This *tail cancellation condition* thus gives rise to the set of linear homogeneous equations

$$[-\bar{\boldsymbol{P}}(E) + \bar{\boldsymbol{S}}][\dot{\bar{\boldsymbol{P}}}(E)]^{-\frac{1}{2}}\, \boldsymbol{u}(E) = \boldsymbol{0}\,, \tag{100}$$

which are the KKR equations in the ASA [2-6, 13, 24] with screened (or bare) potential functions and structure constants. The energies for which the determinant of $\bar{\boldsymbol{P}}(E) - \bar{\boldsymbol{S}}$ vanishes are the exact one-electron energies and a solution $\boldsymbol{u}(E)$, normalized according to

$$\boldsymbol{u}(E)^{+}\, \boldsymbol{u}(E) = 1\,, \tag{101}$$

is an exact eigenvector.

For a monoatomic, closely packed solid the simple picture offered by (100) is shown in fig. 8. The energy band problem is reduced to that of finding the eigenvalues for a single atomic sphere, with its spherically symmetric potential, subject to a $\boldsymbol{k}$-dependent and angular-momentum-destroying boundary condition imposed by the surroundings. The information about the atomic sphere is carried by the logarithmic derivatives, which are functions of E, while the information about the crystal structure is carried by the canonical structure matrix, which is a function of $\boldsymbol{k}$. This is the approximate solution of the cellular matching problem envisaged fifty years ago by WIGNER and SEITZ [43].

The KKR-ASA secular equation (100) is, however, far more difficult to solve than the eigenvalue problem obtained with a linear method, in particular when the wave function coefficients are needed. Further shortcomings of the KKR-ASA method are that corrections to the ASA are impossible to include. For these reasons the transformation to a Hamiltonian formalism is useful.

4·6. *From the* KKR-ASA *equation to the* LMTO-ASA *Hamiltonian.* – In order to prove that the exact KKR-ASA equations are equivalent with the eigenvalue equation

$$(\boldsymbol{H}^{(2)} - E\boldsymbol{I})\, \boldsymbol{u} = \boldsymbol{0} \tag{31}$$

to second order in $E - E_{\nu}$, we need a second-order parametrization of the potential function, or, rather, of its inverse function $E_{Rl}(P)$, which is the

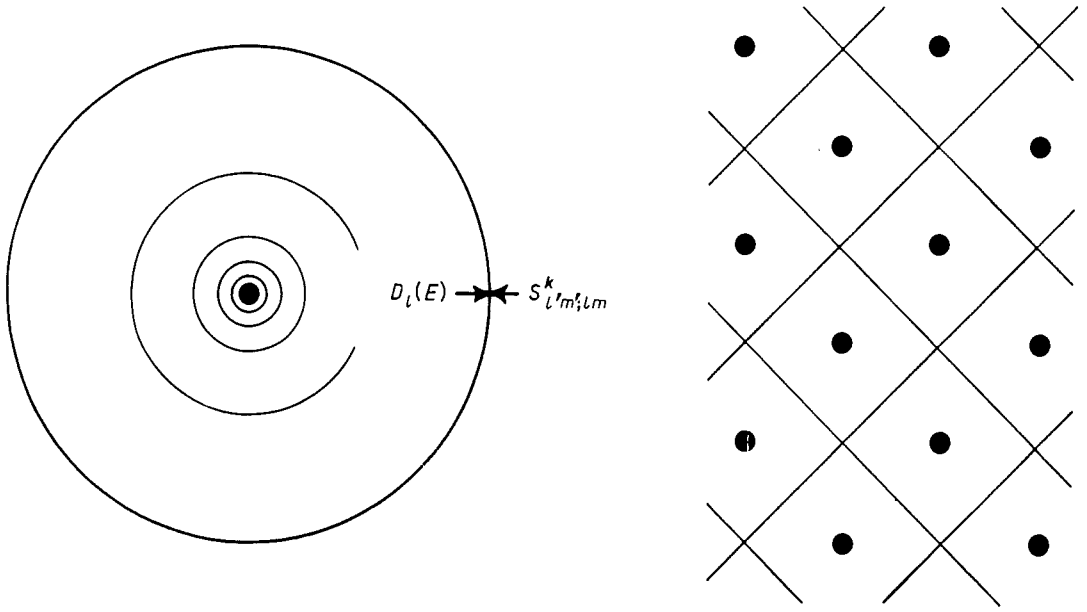

Fig. 8. – The atomic-sphere approximation. By substituting the atomic polyhedra by Wigner-Seitz spheres, the band structure problem may be approximated by a boundary-value problem in which the information about the atomic-sphere size and potential is given by logarithmic derivative function $D_l(E)$, while the information about the crystal structure is given by the structure constants, $S^k_{l'm',lm}$.

energy corresponding to the boundary condition P (see (95)) for the radial Schrödinger equation. A radial trial function with this boundary condition is

$$\Phi_{Rl}(P, r) \equiv \varphi_{Rl}(r) + \dot{\varphi}_{Rl}(r)\,\omega_{Rl}(P)\,. \tag{102}$$

This is just the scalar analogue of expression (27) for the nearly orthogonal MTO such that ω is the scalar analogue of $\boldsymbol{h}$. The matching which determines ω as a function of P is analogous to the matching leading to (65) and (66) or (85). Consequently, P is the scalar analogue of $\boldsymbol{S}$ and $\overline{P}$ is the scalar analogue of $\overline{\boldsymbol{S}}$ so that

$$E(P)^{(2)} \equiv E_\nu + \omega(P) = C + P(1 - QP)^{-1}\Delta = \tag{103}$$

$$= C + \overline{P}[1 - (Q - \bar{Q})\,\overline{P}]^{-1}\Delta = V + (Q^{-1} - P)^{-1}\Gamma\,.$$

We now use the variational principle to determine $E(P)$ and find, in analogy to (29) and (30), that

$$E(P) \approx E(P)^{(3)} \equiv \frac{\langle\Phi(P)|-\nabla^2 + V|\Phi(P)\rangle}{\langle\Phi(P)|\Phi(P)\rangle} = E_\nu + \frac{\omega(P)}{1 + p\omega(P)^2}\,. \tag{104}$$

From the form (102) it is obvious that $E(P)^{(2)}$ is the energy correct to first order. The error of the trial function (102) is, therefore, of second order and, due to the variational principle, the error of the energy estimate (104) is of fourth order. Since (104) contains no terms of order ω^2, the estimate $E(P)^{(2)}$ is, in fact, correct to second order. The corresponding second-order potential function is obtained by solution of (103) with respect to P, *i.e.*

$$P(E)^{(2)} = \frac{(E-C)\Delta^{-1}}{1+Q(E-C)\Delta^{-1}} = \frac{\Gamma}{V-E} + Q^{-1} \tag{105}$$

and

$$\bar{P}(E)^{(2)} = \frac{(E-C)\Delta^{-1}}{1+(Q-\bar{Q})(E-C)\Delta^{-1}} . \tag{106}$$

Differentiation with respect to energy yields

$$[\dot{\bar{P}}(E)^{(2)}]^{-\frac{1}{2}} = [1+(Q-\bar{Q})(E-C)\Delta^{-1}]\Delta^{\frac{1}{2}} . \tag{107}$$

If we finally insert the second-order model (106) and (107) in the left-hand side of the exact KKR-ASA equations (100) and multiply each equation by $\boldsymbol{\Delta}^{\frac{1}{2}}[\boldsymbol{I}-\bar{\boldsymbol{S}}(\boldsymbol{Q}-\bar{\boldsymbol{Q}})]^{-1}$, we obtain

$$\boldsymbol{\Delta}^{\frac{1}{2}}[\boldsymbol{I}-\bar{\boldsymbol{S}}(\boldsymbol{Q}-\bar{\boldsymbol{Q}})]^{-1}[-\bar{\boldsymbol{P}}(E)^{(2)}+\bar{\boldsymbol{S}}][\dot{\bar{\boldsymbol{P}}}(E)^{(2)}]^{-\frac{1}{2}}\boldsymbol{u}=\boldsymbol{0}$$

or

$$\boldsymbol{\Delta}^{\frac{1}{2}}[\boldsymbol{I}-\bar{\boldsymbol{S}}(\boldsymbol{Q}-\bar{\boldsymbol{Q}})]^{-1}[-\{\boldsymbol{I}-\bar{\boldsymbol{S}}(\boldsymbol{Q}-\bar{\boldsymbol{Q}})\}\{E\boldsymbol{I}-\boldsymbol{C}\}\boldsymbol{\Delta}^{-1}+\bar{\boldsymbol{S}}]\boldsymbol{\Delta}^{\frac{1}{2}}\boldsymbol{u}=\boldsymbol{0}$$

or

$$[-E\boldsymbol{I}+\boldsymbol{C}+\boldsymbol{\Delta}^{\frac{1}{2}}\{\boldsymbol{I}-\bar{\boldsymbol{S}}(\boldsymbol{Q}-\bar{\boldsymbol{Q}})\}^{-1}\bar{\boldsymbol{S}}\boldsymbol{\Delta}^{\frac{1}{2}}]\boldsymbol{u}=\boldsymbol{0} . \tag{108}$$

These equations are identical with (31), as we see by comparison with (65) and (66), and we have thus proved that the eigenvalues, $E_j^{(2)}$, *and eigenvectors*, $\boldsymbol{u}_j$, of $\boldsymbol{H}^{(2)}$ are correct to order $(E_j-E_{\nu})^2$.

This proof could, of course, have been carried through somewhat more easily had we from the onset chosen $\bar{Q}\equiv Q$ and, hence, $\bar{P}(E)^{(2)}\equiv\tilde{P}(E)^{(2)}=$ $=(E-C)\Delta^{-1}$. However, we believe that the more involved proof using a general $\bar{Q}$ illustrates our « transformation theory ». An even more complicated, and perhaps even more illustrative, proof is possible as well: In (102) we could have used a nonorthogonal $\dot{\bar{\varphi}}(r)$-function and an $\bar{\omega}(P)$-function similar to (103) but with barred potential parameters. The estimate $\bar{E}(P)^{(1)}\equiv E_{\nu}+$ $+\bar{\omega}(P)$ would only be correct to first order and the third-order estimate (104) would have contained nonorthogonality terms of order $\bar{o}\bar{\omega}^2$. Expressions (105) and (106) would have contained barred potential parameters.

We have mentioned that $\bar{o}$ has the dimension of a reciprocal energy and, by comparison of (91) with (103), we see that $\bar{o}^{-1} + E_\nu$ is the energy corresponding to the « phase shift » $P = \bar{Q}^{-1}$.

4·7. *Accurate expressions for the wave function.* – Since the eigenvectors of $\boldsymbol{H}^{(2)}$ are correct to second order, the radial wave functions, $\varphi(E_j, r)$, entering the one-centre expansions (32) of the wave function should be expanded to second, rather than merely to first, order in $E_j - E_\nu$. When *exact* continuity and differentiability at the sphere is required, a further term, $\frac{1}{6}(E_j - E_\nu)^3 \cdot g(E_j - E_\nu)\ddot{\varphi}(r)$, with $g(E_j - E_\nu)$ adjusted such that the resulting « third-order » radial function matches the first-order function at s_R, should be added.

If, as is usually the case, $\boldsymbol{H}^{(2)}$ is truncated after the s, p, and d blocks, we primarily know only the s-, p- and d-components of the eigenvectors u_{RL} and, when we include only these in (32), the *one*-centre expansion is merely converged well *inside* the atoms, maybe up to the radius of the touching MT. However, the *multi*centre MTO expansion in the first line of (32) is everywhere continuously differentiable and forms a good solution of Schrödinger's equation with only s-, p- and d-MTOs included. With $\bar{\boldsymbol{h}}$ truncated after its s, p and d blocks, the higher partial waves ($l > 2$) in the expansion (9) of the MTO tail are those of the unaugmented envelope function, $\bar{\chi}^e(\boldsymbol{r})$, which is identical with $\bar{\chi}^i(\boldsymbol{r})$ in the interstitial region. This means that, with a truncated Hamiltonian, $\bar{\chi}^i(\boldsymbol{r})$ in (9) should be redefined as follows

$$(109) \qquad |\bar{\chi}\rangle^i \to |\bar{\chi}^i\rangle^\infty \equiv [|\bar{K}\rangle^\infty - |K\rangle + |\bar{J}\rangle \bar{S}](2\bar{\Delta}/w)^{\frac{1}{2}} = \\ = [(|K\rangle^\infty - |K\rangle)(I + \bar{Q}\bar{S}) + |J\rangle \bar{S}](2\bar{\Delta}/w)^{\frac{1}{2}} .$$

Here we have used (62) and (49)-(52) and $\bar{\boldsymbol{S}}$ *is truncated at the same point as* $\bar{\boldsymbol{h}}$. The « orbital » $|\bar{\chi}^i_{RL}\rangle^\infty$ thus vanishes well inside its own sphere, it equals the MTO, $|\bar{\chi}_{RL}\rangle^\infty$, in the interstitial region and its tail vanishes well inside the neighbouring atoms.

In order to express the part of the wave function missing in the truncated *one*-centre expansion (32), the *multi*centre expansion in terms of the most localized orbitals is very useful. Suppose that we have diagonalized the truncated $\boldsymbol{H}^{(2)}$ and, therefore, know $E_j^{(2)}$ and $\boldsymbol{u}_j$, we now transform to the set of most localized orbitals. From (32), (27), (28) and (31) we obtain

$$(110) \qquad \psi_j(\boldsymbol{r}) = |\chi\rangle^\infty \boldsymbol{u}_j = |\bar{\chi}\rangle^\infty (\boldsymbol{I} + \bar{\boldsymbol{o}}\bar{\boldsymbol{h}})^{-1} \boldsymbol{u}_j = |\bar{\chi}\rangle^\infty (\boldsymbol{I} - \bar{\boldsymbol{o}}\bar{\boldsymbol{h}}) \boldsymbol{u}_j \equiv |\bar{\chi}\rangle^\infty \bar{\boldsymbol{u}}_j$$

with

$$(111) \qquad \bar{u}_{RL,j} \equiv [1 - \bar{o}_{Rl}(E_j^{(2)} - E_{\nu Rl})]\, u_{RL,j} .$$

We note that the transformation (111) requires no matrix multiplication but merely energy scaling. With (109) the part of the wave function missing in

the truncated one-centre expansion (32) is thus

$$\psi^{i}_{j}(\boldsymbol{r}) = |\overline{\chi}^{i}\rangle^{\infty}\,\overline{u}_{j} = \tag{112}$$
$$= \sum_{R'}\sum_{L'}(w/r_{R'})^{l'+1}_{>}\,Y_{L'}(\boldsymbol{r}_{R'})\sum_{R}\sum_{L}(\delta_{R'R}\delta_{L'L} + \bar{Q}_{l'}\overline{S}_{R'L',RL})(2\overline{\Delta}_{Rl}/w)^{\frac{1}{2}}\,\overline{u}_{RL,j} +$$
$$+ \sum_{R'}\sum_{L'}(r_{R'}/w)^{l'}_{<}[2(2l'+1)]^{-1}\,Y_{L'}(\boldsymbol{r}_{R'})\sum_{R}\sum_{L}\overline{S}_{R'L',RL}(2\overline{\Delta}_{Rl}/w)^{\frac{1}{2}}\,\overline{u}_{RL,j}\,.$$

The subscripts $>$ and $<$ are here meant to indicate that the radial function vanishes, respectively, inside or outside the sphere at R' with radius $s_{R'}$. The cubic harmonics are

$$\begin{cases} Y_{s} \equiv (4\pi)^{-\frac{1}{2}}\,, \qquad Y_{p(x,y,z)} \equiv (4\pi/3)^{-\frac{1}{2}}(\boldsymbol{x},\,\boldsymbol{y},\,\boldsymbol{z})\,, \\ Y_{d(3z^2-1,x^2-y^2)} \equiv (16\pi/5)^{-\frac{1}{2}}(3\boldsymbol{z}^2-1,\,\sqrt{3}(\boldsymbol{x}^2-\boldsymbol{y}^2))\,, \\ Y_{d(yz,xz,xy)} \equiv (4\pi/15)^{-\frac{1}{2}}(\boldsymbol{yz},\,\boldsymbol{xz},\,\boldsymbol{xy})\,, \end{cases} \tag{113}$$

where $\boldsymbol{x} \equiv x/r$, etc. The most localized structure matrix $\overline{\boldsymbol{S}}$ and its parameters $\bar{Q}$ are listed in table I. The $K(\boldsymbol{r})$ or $J(\boldsymbol{r})$ functions entering the superposition (112) are, at most, those $9\times(1+12+6) = 171$ (f.c.c.) or those $9\times(1+8+6) = 135$ (b.c.c.) s-, p- and d-functions which are centred at the atoms belonging to the two shells nearest to the region $\boldsymbol{r}$. In order to obtain the nonspheridized density, $n(\boldsymbol{r})$ (2), for use in the total-energy expression (41) eqs. (32) and (112) should be employed.

4'8. *Exact overlap matrix and the combined-correction term.* – It is often desirable to go beyond the ASA not only for the evaluation of the electron-electron interactions but also for the evaluation of the kinetic-energy term (42) and, hence, for the one-electron Hamiltonian and overlap matrices. Since the definition and construction of the MTOs and the transformations between different MTO sets are independent of the ASA, it should be clear, in principle, how to include the non-ASA terms in $\overline{\boldsymbol{H}}$ and $\overline{\boldsymbol{O}}$. For this purpose the most localized MTO representation is particularly suited. The simplest and most widely used correction to the ASA is the so-called [6] « combined correction » which adds to the sum of the sphere overlaps (22) the difference

$${}^{\infty}\langle\overline{\chi}|\overline{\chi}\rangle^{\infty}_{\mathrm{ex}} - {}^{\infty}\langle\overline{\chi}|\overline{\chi}\rangle^{\infty} = \tag{114}$$
$$= (2\overline{\boldsymbol{\Delta}}/w)^{\frac{1}{2}}(\boldsymbol{I}+\overline{\boldsymbol{S}}\overline{\boldsymbol{Q}})[{}^{\infty}\langle\boldsymbol{K}|\boldsymbol{K}\rangle^{\infty}_{\mathrm{ex}} - {}^{\infty}\langle\boldsymbol{K}|\boldsymbol{K}\rangle^{\infty}](\boldsymbol{I}+\overline{\boldsymbol{Q}}\overline{\boldsymbol{S}})(2\overline{\boldsymbol{\Delta}}/w)^{\frac{1}{2}} =$$
$$= {}^{\infty}\langle\overline{\boldsymbol{\chi}}^{i}|\overline{\boldsymbol{\chi}}^{i}\rangle^{\infty}_{\mathrm{ex}} \equiv (2\overline{\boldsymbol{\Delta}}/w)^{\frac{1}{2}}\,{}^{\infty}\langle\overline{\boldsymbol{K}}^{i}|\overline{\boldsymbol{K}}^{i}\rangle^{\infty}_{\mathrm{ex}}(2\overline{\boldsymbol{\Delta}}/w)^{\frac{1}{2}}$$

between the *exact* overlap and the sum of the sphere overlaps, and which adds to the sphere Hamiltonian (25) the above-mentioned difference times the

average value, V_{MTZ}, of the potential in the «interstitial» region, or, better and more conveniently, (114) times

$$ {}^{\infty}\langle \bar{\chi}^{\mathrm{i}}_{RL} | \bar{\chi}^{\mathrm{i}}_{R'L'} \rangle^{\infty}_{\mathrm{ex}} [v_R(s_R) + v_{R'}(s_{R'})]/2 \,, $$

where $v_R(s_R)$ is the value of the atomic-sphere potential at the sphere. In this way the geometry violation of the ASA as well as the neglect of the higher partial waves arising from truncation of tail expansions are corrected for.

The overlap integrals ${}^{\infty}\langle \boldsymbol{K}|\boldsymbol{K}\rangle^{\infty}_{\mathrm{ex}}$ were originally [6] computed by Fourier transformation of the bare MTO tails. As a consequence, the combined correction could only be applied to crystals and it effectively required the computation of a second set of structure constants as functions of $\boldsymbol{k}$. It is, however, possible [32, 44], and even simpler, to calculate the exact integrals directly in real space. If, for simplicity, we choose the z-axis along the interatomic vector $\boldsymbol{R}' - \boldsymbol{R}$, the result can be expressed as the following two-centre integrals:

$$ (115) \quad \begin{cases} w^{-3}\,{}^{\infty}\langle K_{Rs}|K_{R's}\rangle^{\infty}_{\mathrm{ex}} \equiv {}^{\infty}\langle ss\sigma\rangle^{\infty} = \dfrac{1}{2}\dfrac{d}{w}\,, \\ {}^{\infty}\langle sp\sigma\rangle^{\infty} = -\dfrac{\sqrt{3}}{2}\,, \qquad {}^{\infty}\langle pp\sigma\rangle^{\infty} = 0\,, \qquad {}^{\infty}\langle pp\pi\rangle^{\infty} = \dfrac{3}{2}\left(\dfrac{d}{w}\right)^{-1}\,, \\ {}^{\infty}\langle sd\sigma\rangle^{\infty} = \dfrac{\sqrt{5}}{6}\left(\dfrac{d}{w}\right)^{-1}\,, \; {}^{\infty}\langle pd\sigma\rangle^{\infty} = \dfrac{\sqrt{15}}{6}\left(\dfrac{d}{w}\right)^{-2}\,, \; {}^{\infty}\langle pd\pi\rangle^{\infty} = -\dfrac{\sqrt{5}}{2}\left(\dfrac{d}{w}\right)^{-2}\,, \\ {}^{\infty}\langle dd\sigma\rangle^{\infty} = \dfrac{5}{3}\left(\dfrac{d}{w}\right)^{-3}\,, \qquad {}^{\infty}\langle dd\pi\rangle^{\infty} = -\dfrac{5}{3}\left(\dfrac{d}{w}\right)^{-3}\,, \; {}^{\infty}\langle dd\delta\rangle^{\infty} = \dfrac{5}{6}\left(\dfrac{d}{w}\right)^{-3}\,, \end{cases} $$

where, as usual, $d \equiv |\boldsymbol{R}' - \boldsymbol{R}| \neq 0$, and w is the scale factor ($\equiv$ average Wigner-Seitz radius) chosen in the definition (45) of $K(\boldsymbol{r})$ and of the potential parameters. The overlap integrals for a general z-direction may be obtained from the two-centre integrals (115) by use of table I in ref. [38]. For the two bare s-functions the integral in the sphere (of radius d) centred at one of the atoms and passing through the centre of the other equals $(d/w)/2$, while the remaining part of the integral, of course, diverges. Since we are going to screen the bare s-functions, this divergence will, however, be exactly cancelled and it has, therefore, been neglected in (115). For the on-site ($\boldsymbol{R}' = \boldsymbol{R}$) terms we define

$$ (116) \qquad w^{-3}\,{}^{\infty}\langle K_{RL}|K_{RL'}\rangle^{\infty}_{\mathrm{ex}} \equiv \delta_{LL'} \begin{cases} 0 & \text{for } l = 0\,, \\ (2l-1)^{-1}(s_R/w)^{-(2l-1)} & \text{for } l > 0\,. \end{cases} $$

For $l > 0$ this is the value of the integral outside the sphere of radius s_R, because the (diverging) integral inside the sphere will be cancelled by the on-site term from the second, spherical part of (114). For $l = 0$ the integral inside the sphere will again be cancelled by the on-site term from the second

part of (114) and the integral outside the sphere diverges, but will be cancelled through the screening.

The second, spherical term in (114) may be evaluated from (48), and the result of (114) in the « bare representation » is, therefore, seen to be

$$(117) \qquad {}^{\infty}\langle \boldsymbol{K}^{\mathrm{i}}|\boldsymbol{K}^{\mathrm{i}}\rangle_{\mathrm{ex}}^{\infty} = {}^{\infty}\langle \boldsymbol{K}|\boldsymbol{K}\rangle_{\mathrm{ex}}^{\infty} + \boldsymbol{S}\langle \boldsymbol{JK}\rangle + \langle \boldsymbol{JK}\rangle \boldsymbol{S} - \boldsymbol{S}\langle \boldsymbol{JJ}\rangle \boldsymbol{S} .$$

Here ${}^{\infty}\langle \boldsymbol{K}|\boldsymbol{K}\rangle_{\mathrm{ex}}^{\infty}$ is the matrix defined through (115) and (116) and $\langle \boldsymbol{JK}\rangle$ and $\langle \boldsymbol{JJ}\rangle$ are diagonal matrices with elements easily calculated as

$$(118) \qquad w^{-3}\langle JK\rangle_{Rl} = [4(2l+1)]^{-1}(s_R/w)^2$$

and

$$(119) \qquad w^{-3}\langle JJ\rangle_{Rl} = [4(2l+1)^2(2l+3)]^{-1}(s_R/w)^{2l+3} .$$

We finally transform to the screened representation and obtain for use in (114)

$$(120) \qquad {}^{\infty}\langle \boldsymbol{K}^{\mathrm{i}}|\boldsymbol{K}^{\mathrm{i}}\rangle_{\mathrm{ex}}^{\infty} = (\boldsymbol{I} + \overline{\boldsymbol{S}}\overline{\boldsymbol{Q}})\,{}^{\infty}\langle \boldsymbol{K}|\boldsymbol{K}\rangle_{\mathrm{ex}}^{\infty}(\boldsymbol{I} + \overline{\boldsymbol{Q}}\overline{\boldsymbol{S}}) +$$

$$+ \overline{\boldsymbol{S}}\langle \boldsymbol{JK}\rangle(\boldsymbol{I} + \overline{\boldsymbol{Q}}\overline{\boldsymbol{S}}) + (\boldsymbol{I} + \overline{\boldsymbol{S}}\overline{\boldsymbol{Q}})\langle \boldsymbol{JK}\rangle\overline{\boldsymbol{S}} - \overline{\boldsymbol{S}}\langle \boldsymbol{JJ}\rangle\overline{\boldsymbol{S}} =$$

$$= (\boldsymbol{I} + \overline{\boldsymbol{S}}\overline{\boldsymbol{Q}})[{}^{\infty}\langle \boldsymbol{K}|\boldsymbol{K}\rangle_{\mathrm{ex}}^{\infty} + \langle \hat{\boldsymbol{K}}^2\rangle](\boldsymbol{I} + \overline{\boldsymbol{Q}}\overline{\boldsymbol{S}}) - [\boldsymbol{I} + \overline{\boldsymbol{S}}(\overline{\boldsymbol{Q}} - \hat{\boldsymbol{Q}})]\langle \hat{\boldsymbol{K}}^2\rangle[\boldsymbol{I} + (\overline{\boldsymbol{Q}} - \hat{\boldsymbol{Q}})\overline{\boldsymbol{S}}] .$$

Here, the second form is the more convenient, and $\langle \hat{\boldsymbol{K}}^2\rangle$ and $\hat{\boldsymbol{Q}}$ are diagonal matrices with the elements

$$(121) \qquad \frac{\langle \hat{K}^2\rangle}{w^3} \equiv \frac{\langle JK\rangle^2}{w^3\langle JJ\rangle} = \frac{2l+3}{4}\left(\frac{s}{w}\right)^{-(2l-1)}$$

and

$$(122) \qquad \hat{Q} \equiv \frac{\langle JJ\rangle}{\langle JK\rangle} = \frac{1}{(2l+1)(2l+3)}\left(\frac{s}{w}\right)^{2l+1} .$$

$\langle \hat{K}^2\rangle$ in the first term thus effectively adds the integral inside the sphere to the diagonal element (116) of ${}^{\infty}\langle \boldsymbol{K}|\boldsymbol{K}\rangle_{\mathrm{ex}}^{\infty}$.

The combined-correction matrix depends on the atomic positions, the sphere radii and the l-truncation. The augmentation spheres need not be taken as space-filling atomic spheres, but, if they are, the combined correction is usually small enough to be treated together with the third-order correction $\overline{\boldsymbol{h}}\boldsymbol{p}\overline{\boldsymbol{h}}$ to the overlap matrix (22) and $\overline{\boldsymbol{h}}\boldsymbol{E}_{\nu}\boldsymbol{p}\overline{\boldsymbol{h}}$ to the Hamiltonian (25), either by first-order perturbation theory as in (33) or by the approximate Löwdin procedure (89). For use in (33) we merely need the diagonal ($j = j'$) matrix element which equals (120) multiplied from the left by the vector

$$(2\bar{\Delta}_{Rl}/w)^{\frac{1}{2}}[1 - \tilde{o}_{Rl}(E_j^{(2)} - E_{\nu Rl})]u_{Rl,j}$$

and from the right by its transpose. For similar sphere sizes, *i.e.* $s_R \approx w$, we see from (77*a*) and (122) that $\bar{Q} - \hat{Q}$ is rather small.

4·9. *Convergence in R and l.* – The condition that the long-ranged part of bare monopole fields be screened is the condition of « charge neutrality », which from (52) is seen to be

$$0 = \sum_{R=0}^{\infty} (\delta_{0R} + \bar{Q}_s \bar{S}_{0s,Rs}) = \tag{123}$$

$$= 1 + \bar{Q}_s [ss\sigma(\text{on-site}) + M_1 \cdot ss\sigma(d_1) + M_2 \cdot ss\sigma(d_2) + \ldots] .$$

Here M_1 is the number of first nearest neighbours and d_1 their distance from the central atom. From the construction of the screened structure matrix $\bar{\mathbf{S}}$, through inversion of the finite matrix $\bar{\mathbf{Q}}^{-1} - \mathbf{S}^k$ and subsequent Fourier transformation, it is obvious that $\bar{\mathbf{S}}$ decays exponentially in real space, provided that the determinant of $\bar{\mathbf{Q}}^{-1} - \mathbf{S}^k$ vanishes nowhere in the Brillouin zone. The sum rule (123) applied to our most localized structure matrix given in table I for the f.c.c., b.c.c. and s.c. lattices yields $(1 + 1.06) - 2.02 - 0.04 = 0.00$ for the f.c.c. lattice, $(1 + 1.08) - 1.65 - 0.43 = 0.00$ for the b.c.c. lattice and $(1 + 1.30) - 2.01 - 0.29 = 0.00$ for the s.c. lattice. In all three cases we merely include the zeroth-, first- and second-neighbour shells.

With an exponential decay not only the bare monopole field, but all multipole fields vanish as $r \to \infty$, provided that infinitely many terms are included in (52), that is, if we do not truncate $\bar{\mathbf{S}}$ after a certain number of shells. In fig. 6 we included the shell of third nearest neighbours. The general sum rule is expressed as follows: The screened multipole field, $\bar{K}_{0L'}(\boldsymbol{r})$, centred at the origin may be expressed as the superposition (52) of bare multipole fields, $K_{RL}(\boldsymbol{r}_R)$, centred at the origin and at the neighbouring sites. The bare fields may be expanded about the origin according to

$$K_{RL}(\boldsymbol{r}_R) = \sum_{l' \geqslant l} \sum_{m'} K_{0L'}(\boldsymbol{r})\, T_{0L',RL} , \tag{124}$$

which is analogous to (45), but valid for $r > R$. The condition that $\bar{K}_{0L'}(\boldsymbol{r})$ decays faster than any inverse power of r as $r \to \infty$ now means that the matrix elements $[\boldsymbol{T}(\boldsymbol{I} + \bar{\mathbf{Q}}\bar{\mathbf{S}})]_{0L'0L''}$ must vanish for all L'. The matrix $\boldsymbol{T}$ is not Hermitian and is given by

$$\begin{cases} T_{0L',RL} = 0 \text{ for } l' < l\,, \quad T_{0L',0L} = \delta_{L'L}\,, \quad T_{0lm',Rlm} = \delta_{m'm}\,, \\ T_{pp\sigma} = \dfrac{1}{\sqrt{3}} \dfrac{d}{w}\,, \quad T_{dp(\sigma,\pi)} = \left(\dfrac{2\sqrt{3}}{\sqrt{5}}\,,\ \dfrac{3}{\sqrt{5}} \right) \dfrac{d}{w}\,, \quad T_{ds\sigma} = \dfrac{1}{\sqrt{5}} \left(\dfrac{d}{w} \right)^2 , \end{cases} \tag{125}$$

such that the general sum rule for the screened structure matrix may be

expressed as

$$0 = \delta_{L'L''} + \sum_{R} \bar{Q}_{l'} \bar{S}_{RL',0L''} + \sum_{R>0} \sum_{l=0}^{l'-1} \sum_{m} T_{0L',RL} \bar{Q}_{l} \bar{S}_{RL,0L''} \tag{126}$$

for all L' and L''.

The bare structure matrix is given by the simple analytical expressions (46) or (47), but the *screened* structure matrix must be calculated numerically for each lattice type. The results given in table I enable one to perform band structure calculations for any compound whose atoms are placed on one of the three lattice types, f.c.c., b.c.c., or s.c., or on a superlattice of any of these. The band structure of Cu_3Au may, for instance, be computed from the f.c.c. structure matrix, that of CsCl from the b.c.c. structure matrix and that of NaCl from the s.c. structure matrix. Moreover, the band structure of Si may be computed from the b.c.c. structure matrix by placing «empty spheres», *i.e.* spheres with no nucleus, on every second lattice point [45]. The results in table I furthermore enable one to perform calculations for localized impurities using either a Dyson equation for the perturbation, $\delta\overline{\boldsymbol{H}}$ and $\delta\overline{\boldsymbol{O}}$, caused by the change of the potential parameters at the impurity and near-neighbour sites, or a Dyson equation based on the KKR-ASA equation (100) for the perturbation $\delta\overline{\boldsymbol{P}}(E)$. In the ASA the latter procedure [46] is the more convenient because $\delta\overline{\boldsymbol{P}}(E)$ is diagonal.

We have chosen to use only the s, p and d multipoles for the construction of the screened structure matrix although it seems obvious that with the inclusion of f, and perhaps even higher, multipoles (*i.e.* with $\bar{Q}_f$ as an adjustable parameter) the screening in $\boldsymbol{r}$-space could have been further improved. The reason for not including f multipoles when constructing the canonical $\overline{\boldsymbol{S}}$ is that this would force us *always* to include the f-orbitals, even in calculations for materials without f-bands in the energy region of interest. This is so because in a basis set, without f-orbitals, $\dot{\bar{\varphi}}_f(r)$ is the only radial f-function present, as seen from eq. (9). This function has a logarithmic derivative which is given by (58) with the $\bar{Q}_f$-value obtained from the screening calculation. The proper, regular solution $\varphi_f(E, r)$ of the radial Schrödinger equation, however, behaves like the *regular* solution of the radial wave or Laplace equation, *i.e.* like

$$j_l(r\sqrt{E - V_l}) \to \text{const} \times J_l(r) = \text{const} \times r^l\,, \tag{127}$$

when l is so large ($l > l_{\max} \approx 2$) that the centrifugal term $l(l+1)r^{-2}$ dominates, or when the energy is far from a l-resonance. With $\bar{Q}_f$ considerably different from zero the only way of forming a radial f-function which behaves like (127) is thus to form a linear combination of $\dot{\bar{\varphi}}_f(r)$ and $\varphi_f(r)$, where the latter functions *must* be supplied through the explicit inclusion of f-orbitals. In conclusion, in order to avoid using orbitals with l-values for which the centrifugal term dominates the radial Schrödinger equation inside the sphere, we must

choose

$$\bar{Q}_l = 0 \qquad \text{for } l > l_{\max}. \tag{128}$$

Our choice of $l_{\max} = 2$, rather than smaller than two, was necessitated by our desire to localize the range of the orbitals to the two nearest-neighbour shells. The values (77) obtained for $\bar{Q}_s$, $\bar{Q}_p$ and $\bar{Q}_d$ can now be « understood » as the sequence giving the fastest, and still smooth, increase of $\bar{D}_l - l$ for decreasing l. ($\bar{D}_l - l = 0, 0, 0.6, 1.4$ and 2.3 for l decreasing from 4 to 0.)

4·10. *Moving the atoms.* – The above-mentioned applications require that the atoms are positioned on points of a lattice. If the translational symmetry of the positions is broken, say because we displace an atom or consider an amorphous structure, the inversion of $\bar{\mathbf{Q}}^{-1} - \boldsymbol{S}$ is not trivial. From our numerical inversion for the f.c.c., b.c.c. and s.c. lattices two simplifying features, however, emerge. First of all, the set of $\bar{Q}$-values found to give the best localization for the b.c.c. lattice also gave good localization for the more closely packed f.c.c. lattice as well as for the more loosely packed s.c. lattice. It thus seems that, once found, this set can be used universally. Secondly, if for any submatrix $\bar{\boldsymbol{S}}_{Rl,R'l'}$ with a given interatomic vector $\boldsymbol{R}' - \boldsymbol{R}$ and given l and l' we rotate the orbitals such that their z-direction points along the interatomic vector, then, for the three lattices considered, the resulting matrix elements $ss\sigma$, $sp\sigma$, etc. plotted as functions of the interatomic distance (d/w) in units of the Wigner-Seitz radius of the lattice essentially lie on one « universal » curve. This was illustrated for $ss\sigma$ by the full curve in fig. 5 and it is illustrated for the remaining « two-centre integrals » in fig. 9. We have, in other words, obtained canonical curves analogous to (46) but for the most localized structure constants, and these curves interpolating between the f.c.c., b.c.c. and s.c. lattice points may now be used to construct localized structure matrices for *any* structure without the need to perform further matrix inversions.

This is, of course, only an approximation. Since the screening was performed on a lattice, a screened L-orbital, like, for instance, the b.c.c. screened s-orbital in fig. 6, has a « halo » on the neighbouring sites which makes it not strictly transform according to the l-th irreducible representation of the full rotation group but only according to the corresponding representation of the point group of the site. For the two-centre integrals there may, therefore, depending on the symmetry of the interatomic axis in the lattice, be elements for which $m \neq m'$. Moreover, not all $ll'(m = m')$ elements need to be identical. Such cases may be found in table I and seen in fig. 9. As an example, in the s.c. structure the nearest-neighbour $dd\delta$ interaction is -0.443 between $x^2 - y^2$ orbitals but -0.639 between xy orbitals. For well-localized orbitals these « deviations from axial symmetry of the surrounding medium » are relatively small, however, and it should be possible to treat them by perturbation theory in real space, as we shall indicate below. On the other hand, for orthogonal

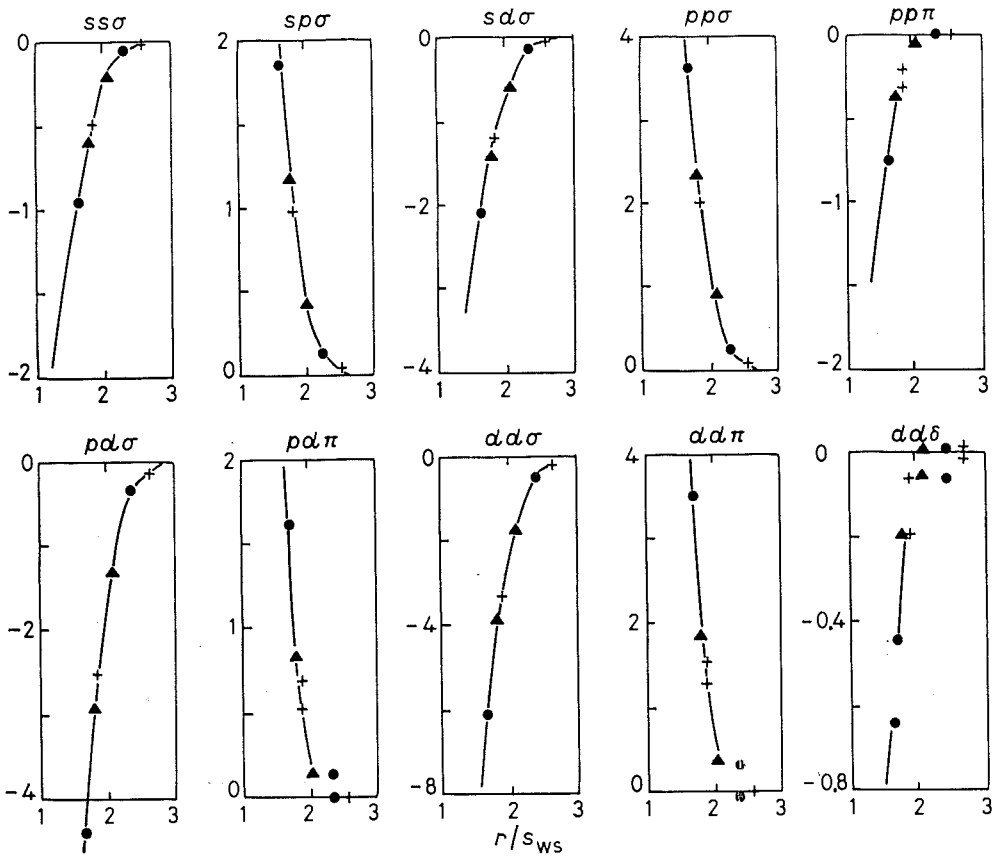

Fig. 9. – The most localized two-centre integrals as a function of the interatomic distance r in units of the Wigner-Seitz radius for the f.c.c. (+), b.c.c. (▲) and s.c. (•) structures.

orbitals, which decay exponentially but have long range, the two-centre integrals are quite structure dependent as was demonstrated in fig. 5 for $ss\sigma$ of vanadium.

Figure 9 shows that it does make sense to interpolate between (the axially symmetric average of) the most localized two-centre integrals obtained by screening on different lattices, and table II gives a simple interpolation for-

TABLE II. – *Interpolation formula,* $\bar{S}_{ll'm}(d) \approx \bar{S} z^{-p} \exp[-z^q]$, *for closely packed structures.*

	$ss\sigma$	$sp\sigma$	$sd\sigma$	$pp\sigma$	$pp\pi$	$pd\sigma$	$pd\pi$	$dd\sigma$	$dd\pi$	$dd\delta$
$\bar{S}$	−0.56	1.10	−1.54	8.59	−16.95	−1.10	27.8	−1.27	11.88	−4.51
λ	0.493	0.488	0.488	0.601	0.859	0.426	0.804	0.415	0.633	0.703
p	5	4	3	2	1	4	2	4	3	4
q	3	4	4	3	3	6	3	6	4	4

$z \equiv \lambda d/w$, $d \equiv$ interatomic distance, $w \equiv$ volume/number of atoms,
$d/w = 1.7589$ for the eight first nearest neighbours in the b.c.c. structure,
1.8094 (f.c.c. twelve first nearest neighbours),
2.0310 (b.c.c. six second nearest neighbours),
2.5589 (f.c.c. six second nearest neighbours).

mula which reproduces the b.c.c. and f.c.c. results rather well. The structure matrix for a non-f.c.c., b.c.c. or s.c. structure may then be found by using table II as a zeroth estimate of the off-site elements. The on-site elements for $l > 0$ depend on the local symmetry and should be estimated from the off-site elements using $\overline{\mathbf{S}}_{on} = \mathbf{S}_{off}\overline{\mathbf{Q}}\overline{\mathbf{S}}_{off}$. The element $ss\sigma$ (on-site) should be obtained from the sum rule (123). Starting from this zeroth estimate, $\overline{\mathbf{S}}^0$, one should finally solve (51) iteratively, *i.e.* construct the matrix

$$\overline{\mathbf{S}}^{i+1} = \mathbf{S} + \mathbf{S}\overline{\mathbf{Q}}\overline{\mathbf{S}}^i \tag{129}$$

in real space and iterate until $\overline{\mathbf{S}}^{i+1} \approx \overline{\mathbf{S}}^i$.

4·11. *Blowing-up.* – In table I only the interactions between the *s*-, *p*- and *d*-orbitals have been included, but, for rare earths and actinides, the interactions with and between the *f*-orbitals are needed as well. Since we have chosen $\bar{Q}_f = 0$, the off-diagonal block $\overline{\mathbf{S}}^{HL}$ of the screened structure matrix, where the index H refers to the « higher » orbitals (here *f*) for which $\bar{Q}^H \equiv 0$ and the index L refers to the « lower » orbitals (here *s*, *p* and *d*), equals

$$\overline{\mathbf{S}}^{HL} = \mathbf{S}^{HL} + \mathbf{S}^{HL}\overline{\mathbf{Q}}^L\overline{\mathbf{S}}^{LL}, \tag{130}$$

as obtained from (51). We may thus obtain $\overline{\mathbf{S}}^{HL}$ (in real space) from the HL block of the bare structure matrix given by (47) and the LL block of the screened structure matrix given by table I. Similarly, the *ff* diagonal block of the screened structure matrix may be obtained from

$$\overline{\mathbf{S}}^{HH} = \mathbf{S}^{HH} + \mathbf{S}^{HL}(\overline{\mathbf{Q}}^L + \overline{\mathbf{Q}}^L\overline{\mathbf{S}}^{LL}\overline{\mathbf{Q}}^L)\mathbf{S}^{LH}. \tag{131}$$

Expressions (130) and (131) not only apply to the *f*-orbitals but to any type of orbitals for which we have chosen $\bar{Q}^H = 0$. An important second example is the calculation of matrix elements for orbitals at interstitial impurity sites.

4·12. *Folding-down.* – In certain cases it is desirable, at some expense of localization, to reduce the number of orbitals to less than the nine *s*-, *p*- and *d*-orbitals per site. Such cases include the folding-down of the *d*-orbitals for simple metals, the folding-down of the chalcogen or halogen *s*- and *d*-orbitals for chalcogenides or halogenides, and the folding-down of the *s*-, *p*- and *d*-orbitals at vacancy sites.

The principle for folding-down is the following: If we wish to exclude the « higher » subset $|\overline{\chi}^H\rangle^\infty$ from the basis set (9) and, therefore, are left with only *one* radial degree of freedom for each higher radial Schrödinger-equation

solution, namely the tail function $\dot{\bar{\bar{\varphi}}}_H(r)$ of the reduced set

$$|\bar{\bar{\chi}}^{\mathrm{L}}\rangle^{\infty} \equiv |\varphi^{\mathrm{L}}\rangle + |\dot{\bar{\bar{\varphi}}}^{\mathrm{L}}\rangle \bar{\bar{h}}^{\mathrm{LL}} + |\dot{\bar{\bar{\varphi}}}^{\mathrm{H}}\rangle \bar{\bar{h}}^{\mathrm{HL}} + |\bar{\bar{\chi}}^{\mathrm{Li}}\rangle^{\infty}\,, \tag{132}$$

then we better choose $\dot{\bar{\bar{\varphi}}}_H(r)$ approximately equal to the proper solution $\varphi_H(E, r)$. In (132) the «lower» radial tail functions are unchanged from the original basis set, *i.e.*

$$\dot{\bar{\bar{\varphi}}}_L(r) \equiv \dot{\bar{\varphi}}_L(r)$$

or, equivalently,

$$\bar{\bar{o}}_L \equiv \bar{o}_L\,, \qquad \text{or} \qquad \bar{\bar{Q}}_L \equiv \bar{Q}_L\,. \tag{133}$$

We shall now specify the higher radial tail functions and let us, for the sake of the argument, first consider the extreme case where we let $\dot{\bar{\bar{\varphi}}}_H(r)$, and hence the basis set (132), be energy dependent and let $\dot{\bar{\bar{\varphi}}}_H(r)$ be equal to $\varphi_H(E, r)$ times a normalization factor. The two functions thus have the same logarithmic derivative or, in other words, we have chosen

$$\bar{\bar{Q}}_H(E) \equiv [P_H(E)]^{-1}\,, \tag{134}$$

as seen by comparison of (58) with (95). Let us for further simplicity use the KKR-ASA equations (100). In the down-folded «double-bar representation» the one-electron energies are given by

$$\det[\bar{\bar{\mathbf{P}}}(E) - \bar{\bar{\mathbf{S}}}(E)] = 0 \tag{135}$$

and, since from (133), (134) and (94)

$$\bar{\bar{P}}_L(E) = \bar{P}_L(E) \quad \text{and} \quad \bar{\bar{P}}_H(E) \to \infty\,, \tag{136}$$

the secular equation (135) reduces to

$$\det[\bar{\mathbf{P}}^{\mathrm{L}}(E) - \bar{\bar{\mathbf{S}}}^{\mathrm{LL}}(E)] = 0 \tag{137}$$

which only involves the lower block. This is exact within the ASA. The price paid for the lower matrix dimensions in (137) is, of course, that the double-barred structure matrix depends on energy and on the higher potential parameters through (134). Furthermore, the exact calculation of $\bar{\bar{\mathbf{S}}}^{\mathrm{LL}}(E)$ requires evaluation of the Green-function matrix

$$\bar{\mathbf{F}}^{\mathrm{HH}}(E) \equiv [\bar{\mathbf{P}}^{\mathrm{H}}(E) - \bar{\mathbf{S}}^{\mathrm{HH}}]^{-1}\,, \tag{138}$$

as we shall see in (142) below. The down-folding is, therefore, only useful in those cases in which the lower and higher energy bands are so well separated that, for E in the lower range, the inversion of $\overline{\boldsymbol{P}}^{\mathrm{H}}(E) - \overline{\boldsymbol{S}}^{\mathrm{HH}}$ can be simplified, for instance, by neglect of the off-diagonal elements. In the higher energy range the exact $\overline{\overline{\boldsymbol{S}}}^{\mathrm{LL}}(E)$, of course, has poles at the zeros of $\det[\overline{\boldsymbol{P}}^{\mathrm{H}}(E) - \overline{\boldsymbol{S}}^{\mathrm{HH}}]$.

The explicit expression for $\overline{\overline{\boldsymbol{S}}}$, as defined by (133) and (134), in terms of the canonical energy-independent structure matrix that we started out from may be obtained from the general transformation

$$\overline{\overline{\boldsymbol{S}}} = \overline{\boldsymbol{S}} + \overline{\boldsymbol{S}}(\overline{\overline{\boldsymbol{Q}}} - \overline{\boldsymbol{Q}})\,\overline{\overline{\boldsymbol{S}}} \tag{139}$$

derived from (51). With $\overline{\overline{\boldsymbol{Q}}}^{\mathrm{L}} - \overline{\boldsymbol{Q}}^{\mathrm{L}} = \boldsymbol{0}$ and

$$\overline{\overline{\boldsymbol{Q}}}^{\mathrm{H}} - \overline{\boldsymbol{Q}}^{\mathrm{H}} = [\boldsymbol{P}^{\mathrm{H}}(E)]^{-1} - \overline{\boldsymbol{Q}}^{\mathrm{H}} = [\overline{\boldsymbol{P}}^{\mathrm{H}}(E)]^{-1}\,, \tag{140}$$

where the last expression follows from (94), the transformation yields for the HH block

$$\overline{\overline{\boldsymbol{S}}}^{\mathrm{HH}}(E) = \overline{\boldsymbol{S}}^{\mathrm{HH}} + \overline{\boldsymbol{S}}^{\mathrm{HH}}[\overline{\boldsymbol{P}}^{\mathrm{H}}(E)]^{-1}\,\overline{\overline{\boldsymbol{S}}}^{\mathrm{HH}}(E)$$

or

$$\overline{\overline{\boldsymbol{S}}}^{\mathrm{HH}}(E) = \overline{\boldsymbol{P}}^{\mathrm{H}}(E)\,\overline{\boldsymbol{F}}^{\mathrm{HH}}(E)\,\overline{\boldsymbol{S}}^{\mathrm{HH}}\,. \tag{141}$$

Similarly for the HL block

$$\overline{\overline{\boldsymbol{S}}}^{\mathrm{HL}}(E) = \overline{\boldsymbol{P}}^{\mathrm{H}}(E)\,\overline{\boldsymbol{F}}^{\mathrm{HH}}(E)\,\overline{\boldsymbol{S}}^{\mathrm{HL}} \tag{142}$$

and for the LL block

$$\overline{\overline{\boldsymbol{S}}}^{\mathrm{LL}}(E) = \overline{\boldsymbol{S}}^{\mathrm{LL}} + \overline{\boldsymbol{S}}^{\mathrm{LH}}[\overline{\boldsymbol{P}}^{\mathrm{H}}(E)]^{-1}\,\overline{\overline{\boldsymbol{S}}}^{\mathrm{HL}}(E) = \overline{\boldsymbol{S}}^{\mathrm{LL}} + \overline{\boldsymbol{S}}^{\mathrm{LH}}\,\overline{\boldsymbol{F}}^{\mathrm{HH}}(E)\,\overline{\boldsymbol{S}}^{\mathrm{HL}}\,. \tag{143}$$

These are the results anticipated above. Another way of obtaining the same results is to eliminate the unknowns $[\dot{\bar{P}}_H(E)]^{-\frac{1}{2}}u_H(E)$ from the KKR-ASA equations (100) in the barred representation.

Although the ASA energies are given in (137) by the lower block of $\overline{\overline{\boldsymbol{S}}}(E)$ alone, it is obvious that the higher radial functions are needed in the one-centre expansion (99) of the wave function. Even if we are only interested in the lower components $\boldsymbol{u}^{\mathrm{L}}(E)$ of the eigenvector, we do need the higher components $\boldsymbol{u}^{\mathrm{H}}(E)$, because they are involved in the normalization (101). We now determine the entire eigenvector $\boldsymbol{u}(E)$. In the double-bar representation the lower KKR-ASA equations (100) are

$$[-\overline{\boldsymbol{P}}^{\mathrm{L}}(E) + \overline{\overline{\boldsymbol{S}}}^{\mathrm{LL}}(E)][\dot{\overline{\boldsymbol{P}}}^{\mathrm{L}}(E)]^{-\frac{1}{2}}\,\boldsymbol{u}^{\mathrm{L}}(E) + \overline{\overline{\boldsymbol{S}}}^{\mathrm{LH}}(E)[\dot{\overline{\overline{\boldsymbol{P}}}}^{\mathrm{H}}(E)]^{-\frac{1}{2}}\,\boldsymbol{u}^{\mathrm{H}}(E) = \boldsymbol{0}\,. \tag{144}$$

Since $\dot{\bar{\boldsymbol{P}}}^{\mathrm{H}}(E)$ diverges according to (136) and since $\bar{\bar{\boldsymbol{S}}}^{\mathrm{LH}}(E)$ (143) is finite, the second term in (144) vanishes. The lower components of the eigenvector may, therefore, apart from their normalization, be found by solution of the linear homogeneous equations for the LL block. The higher KKR-ASA equations are

$$\bar{\bar{\boldsymbol{S}}}^{\mathrm{HL}}(E)[\dot{\bar{\boldsymbol{P}}}^{\mathrm{L}}(E)]^{-\frac{1}{2}}\boldsymbol{u}^{\mathrm{L}}(E)+[-\dot{\bar{\boldsymbol{P}}}^{\mathrm{H}}(E)+\bar{\bar{\boldsymbol{S}}}^{\mathrm{HH}}(E)][\dot{\bar{\boldsymbol{P}}}^{\mathrm{H}}(E)]^{-\frac{1}{2}}\boldsymbol{u}^{\mathrm{H}}(E)=\boldsymbol{0}. \tag{145}$$

Here the first term is finite, but, in the second term, $\dot{\bar{\boldsymbol{P}}}^{\mathrm{H}}(E)$ diverges and $[\dot{\bar{\boldsymbol{P}}}^{\mathrm{H}}(E)]^{-\frac{1}{2}}$ vanishes. From (94) we, however, realize that

$$\bar{P}(E)[\dot{\bar{P}}(E)]^{-\frac{1}{2}}=P(E)[\dot{P}(E)]^{-\frac{1}{2}}=\bar{P}(E)[\dot{\bar{P}}(E)]^{-\frac{1}{2}}\approx(E-C)\Delta^{-\frac{1}{2}} \tag{146}$$

is finite and invariant. We may thus solve (145) for each higher component $u_H(E)$ in terms of the (unnormalized) eigenvector $\boldsymbol{u}^{\mathrm{L}}(E)$. If we use (142) in (146) and (145), the result is found to be

$$[\dot{\bar{\boldsymbol{P}}}^{\mathrm{H}}(E)]^{-\frac{1}{2}}\boldsymbol{u}^{\mathrm{H}}(E)=\bar{\boldsymbol{F}}^{\mathrm{HH}}(E)\,\bar{\boldsymbol{S}}^{\mathrm{HL}}[\dot{\bar{\boldsymbol{P}}}^{\mathrm{L}}(E)]^{-\frac{1}{2}}\boldsymbol{u}^{\mathrm{L}}(E)\,. \tag{147}$$

Finally, the wave function normalization is given by

$$\begin{aligned}1&=\boldsymbol{u}^{\mathrm{L}}(E)^{+}\boldsymbol{u}^{\mathrm{L}}(E)+\boldsymbol{u}^{\mathrm{H}}(E)^{+}\boldsymbol{u}^{\mathrm{H}}(E)=\\&=\boldsymbol{u}^{\mathrm{L}}(E)^{+}\{\boldsymbol{I}+[\dot{\bar{\boldsymbol{P}}}^{\mathrm{L}}(E)]^{-\frac{1}{2}}\bar{\boldsymbol{S}}^{\mathrm{LH}}\bar{\boldsymbol{F}}^{\mathrm{HH}}(E)\,\dot{\bar{\boldsymbol{P}}}^{\mathrm{H}}(E)\,\bar{\boldsymbol{F}}^{\mathrm{HH}}(E)\,\bar{\boldsymbol{S}}^{\mathrm{HL}}[\dot{\bar{\boldsymbol{P}}}^{\mathrm{L}}(E)]^{-\frac{1}{2}}\}\,\boldsymbol{u}^{\mathrm{L}}(E)\,.\end{aligned} \tag{148}$$

For $\dot{\bar{P}}_H(E)$ in (147) and (148) and for $\bar{P}_H(E)$ in (138) we may use the second-order expressions (107) and (106), respectively.

If $\bar{\boldsymbol{S}}$ is the most localized structure matrix and the higher bands, defined as the zeros of $\det[\bar{\boldsymbol{P}}^{\mathrm{H}}(E)-\bar{\boldsymbol{S}}^{\mathrm{HH}}]$, are well separated from the lower ones that we seek, then we may approximate $\bar{\boldsymbol{S}}^{\mathrm{HH}}$ by its on-site diagonal elements and $\bar{\bar{\boldsymbol{F}}}^{\mathrm{HH}}(E)$, therefore, becomes a diagonal matrix with the elements

$$\bar{F}^{\mathrm{HH}}_{RL,R'L'}(E)\approx[\bar{P}^{\mathrm{H}}_{RL}(E)-\bar{S}^{\mathrm{HH}}_{RL,RL}]^{-1}\delta_{RR'}\delta_{LL'}\approx\dot{\bar{P}}^{\mathrm{H}}_{RL}(E)^{-1}\delta_{RR'}\delta_{LL'}\,. \tag{149}$$

In this case $\bar{\bar{\boldsymbol{S}}}^{\mathrm{LL}}(E)$ as given by (143) is rather well localized. In the opposite extreme, where E lies within the higher bands, $\bar{\boldsymbol{F}}^{\mathrm{HH}}(E)$ is delocalized and so is $\bar{\bar{\boldsymbol{S}}}^{\mathrm{LL}}(E)$.

The reduction of the down-folded KKR-ASA equations (144) to an orthogonal Hamiltonian problem may be performed along the lines leading to (108), because they merely involve left-multiplication by $(\boldsymbol{\Delta}^{\mathrm{L}})^{\frac{1}{2}}[\boldsymbol{I}-\bar{\bar{\boldsymbol{S}}}^{\mathrm{LL}}(E)(\boldsymbol{Q}^{\mathrm{L}}-\bar{\boldsymbol{Q}}^{\mathrm{L}})]^{-1}$. The result is the slightly energy-dependent second-order Hamiltonian, $\tilde{\boldsymbol{H}}^{\mathrm{LL}}(E)^{(2)}$, given by (65) with

$$\tilde{\boldsymbol{S}}(E)\equiv\bar{\bar{\boldsymbol{S}}}^{\mathrm{LL}}(E)[\boldsymbol{I}-(\boldsymbol{Q}^{\mathrm{L}}-\bar{\boldsymbol{Q}}^{\mathrm{L}})\,\bar{\bar{\boldsymbol{S}}}^{\mathrm{LL}}(E)]^{-1}\,. \tag{150}$$

(This is the Hamiltonian given below in (162) with E substituted for ${}_{\nu}E$.) Alternatively, we may by the application of (63) with $\bar{\bar{S}}^{LL}(E)$ substituted for $\bar{S}$ form the first-order Hamiltonian $\bar{\bar{H}}^{LL}(E)^{(1)}$. (This is the Hamiltonian given below in (157*b*) with E substituted for ${}_{\nu}E$.) Subsequently we may use this Hamiltonian in (88) and, further, in (89) to form more accurate but still slightly energy-dependent Hamiltonians.

In order to go beyond the ASA and to arrive at an energy-*in*dependent but nonorthogonal Hamiltonian problem, we must use the variational LMTO formalism. We, therefore, now return to the muffin-tin orbital in (132). For the lower radial functions we shall use (133), but for the higher functions we must, instead of (134), use an energy-independent choice, *e.g.*

$$\bar{\bar{Q}}_H \equiv [P_H({}_{\nu}E)^{(2)}]^{-1} = \frac{\Delta_H}{{}_{\nu}E - C_H} + Q_H \,. \tag{151}$$

Here, for convenience, we have used the second-order estimate (105) and ${}_{\nu}E$ is an energy at the centre of interest in the lower bands, for instance the average of the elements of the diagonal matrix $\boldsymbol{E}_{\nu}^{L}$. Equivalent with (151) is the following choice of $\bar{\bar{o}}^{H}$

$$E_{\nu H} + \bar{\bar{o}}_H^{-1} = {}_{\nu}E \,, \tag{152}$$

as seen from (91). The energy dependence which in the down-folded KKR-ASA equations enters through $\bar{F}^{HH}(E)$ will in the LMTO equations (4) be accounted for to first order through the overlap matrix. Like in the down-folded KKR-ASA equations the first problem is now to express the blocks $\bar{\bar{h}}^{LL}$ and $\bar{\bar{h}}^{HL}$ entering (132) in terms of the known short-range matrix $\bar{h}$ (63) describing the original orbital set. The transformation from the barred to the double-barred basis is given by (34), which we now write in the following way

$$\bar{\bar{h}} = \bar{h} + \bar{h}(\bar{\bar{o}} - \bar{o})\,\bar{\bar{h}} \,. \tag{153}$$

This transformation is equivalent with (139) and is solved in the same way. The meaning of, and the expression for, the energy $E_{\nu H} + (\bar{\bar{o}}_H - \bar{o}_H)^{-1}$ may be obtained by comparison of (35) with the barred version of (102). The result is

$$E_{\nu H} + (\bar{\bar{o}}_H - \bar{o}_H)^{-1} = E_{\nu H} + \bar{\omega}_H(P_H({}_{\nu}E)^{(2)}) = \bar{C}_H + \bar{\Delta}_H \bar{P}_H({}_{\nu}E)^{(2)} \equiv {}_{\nu}\bar{E}_H \,, \tag{154}$$

which is the energy ${}_{\nu}E$ «seen to first order in ${}_{\nu}E - E_{\nu H}$» from the H-channel in question. ${}_{\nu}\bar{\boldsymbol{E}}^{H}$ is thus a diagonal matrix and, if all H-channels had the same first-order accuracy, its elements would all be the same, that is ${}_{\nu}\bar{\boldsymbol{E}}^{H} = {}_{\nu}\bar{E}\boldsymbol{I}^{H}$. The expression for $\bar{P}_H({}_{\nu}E)^{(2)}$ obtained from (151) and (94), or from

(106), is

$$\bar{P}_H({}_\nu E)^{(2)} = (\bar{\bar{Q}}_H - \bar{Q}_H)^{-1} = \left[\frac{\Delta_H}{{}_\nu E - C_H} + Q_H - \bar{Q}_H\right]^{-1}. \tag{155}$$

With the notation (154) the solution of (153) is

$$\bar{\bar{\mathbf{o}}}^{\mathrm{H}}\bar{\bar{\mathbf{h}}}^{\mathrm{HL}} = \frac{{}_\nu\bar{\mathbf{E}}^{\mathrm{H}} - \mathbf{E}_\nu^{\mathrm{H}}}{{}_\nu E\mathbf{I} - \mathbf{E}_\nu^{\mathrm{H}}}\,[{}_\nu\bar{\mathbf{E}}^{\mathrm{H}} - \bar{\mathbf{H}}^{\mathrm{HH}(1)}]^{-1}\,\bar{\mathbf{h}}^{\mathrm{HL}} \tag{156a}$$

and

$$\bar{\bar{\mathbf{H}}}^{\mathrm{LL}(1)} = \mathbf{E}_\nu^{\mathrm{L}} + \bar{\bar{\mathbf{h}}}^{\mathrm{LL}} = \bar{\mathbf{H}}^{\mathrm{LL}(1)} + \bar{\mathbf{h}}^{\mathrm{LH}}[{}_\nu\bar{\mathbf{E}}^{\mathrm{H}} - \bar{\mathbf{H}}^{\mathrm{HH}(1)}]^{-1}\,\bar{\mathbf{h}}^{\mathrm{HL}}. \tag{157a}$$

In (156*a*) we have given $\bar{\bar{\mathbf{o}}}^{\mathrm{H}}\bar{\bar{\mathbf{h}}}^{\mathrm{HL}}$ rather than $\bar{\bar{\mathbf{h}}}^{\mathrm{HL}}$ because it is the former which enters the expressions for the Hamiltonian and overlap matrices to be derived in the following. Moreover, in the MTO expression (132), the tail function $\dot{\bar{\varphi}}_H(r)$ defined by the double-barred version of (17) is nearly proportional to $\varphi_H(r)$ and has very little by-mixing of $\dot{\varphi}_H(r)$, and, if all E_ν's (L *and* H) were equal, this by-mixing would vanish. This means that $\bar{\bar{v}}_H$ and $\dot{\bar{\bar{\varphi}}}_H(r)$ are very large and that $\bar{\bar{h}}^{\mathrm{HL}}$ is very small, but that the coefficient of $\varphi_H(r)$ in (132), *i.e.* $\bar{\bar{\mathbf{o}}}^{\mathrm{H}}\bar{\bar{\mathbf{h}}}^{\mathrm{HL}}$, is « well behaved ». If ${}_\nu E$ is close to all $E_{\nu H}$'s, the numerator and the denominator of the first factor in (156*a*) are equal and the factor has value one. This is also the value when all E_ν's are equal, so that the numerator and the denominator both vanish. The second factor in (156*a*) would be a Green function, $\bar{\mathbf{G}}^{\mathrm{HH}}(E)^{(1)}$, evaluated at ${}_\nu\bar{E}^{\mathrm{H}}$ if all ${}_\nu\bar{E}_H$'s were equal.

Had we instead of the $\bar{\bar{\mathbf{h}}}$-transformation (153) used the $\bar{\bar{\mathbf{S}}}$-transformation (139)-(143) together with relation (63) between $\bar{\bar{\mathbf{h}}}$ and $\bar{\bar{\mathbf{S}}}$, the results (156*a*) and (157*a*) would have been obtained as

$$\bar{\bar{\mathbf{o}}}^{\mathrm{H}}\bar{\bar{\mathbf{h}}}^{\mathrm{HL}} = \bar{\bar{\mathbf{o}}}^{\mathrm{H}}(\bar{\bar{\Delta}}^{\mathrm{H}})^{\frac{1}{2}}\,\bar{\mathbf{P}}^{\mathrm{H}}({}_\nu E)^{(2)}\,\bar{\mathbf{F}}^{\mathrm{HH}}({}_\nu E)\,\bar{\mathbf{S}}^{\mathrm{HL}}(\bar{\Delta}^{\mathrm{L}})^{\frac{1}{2}} = [\dot{\bar{\mathbf{P}}}^{\mathrm{H}}({}_\nu E)^{(2)}]^{\frac{1}{2}}\,\bar{\mathbf{F}}^{\mathrm{HH}}({}_\nu E)\,\bar{\mathbf{S}}^{\mathrm{HL}}(\bar{\Delta}^{\mathrm{L}})^{\frac{1}{2}} \tag{156b}$$

and

$$\bar{\bar{\mathbf{H}}}^{\mathrm{LL}(1)} \equiv \mathbf{E}_\nu^{\mathrm{L}} + \bar{\bar{\mathbf{h}}}^{\mathrm{LL}} = \bar{\mathbf{C}}^{\mathrm{L}} + (\bar{\Delta}^{\mathrm{L}})^{\frac{1}{2}}\,\bar{\bar{\mathbf{S}}}^{\mathrm{LL}}({}_\nu E)(\bar{\Delta}^{\mathrm{L}})^{\frac{1}{2}}. \tag{157b}$$

The $\bar{P}^{\mathrm{H}}$- and $\dot{\bar{P}}^{\mathrm{H}}$-functions entering these equations as well as the definitions (138) are the second-order estimates (106), or (155), and (107). That (157*b*) equals (157*a*) immediately follows from (154). That the first equation (156*b*) equals (156*a*) most easily follows from (154), (155) and the expression preceding (90). The second equation (156*b*) follows from the first by application of the double-barred version of (91) plus (155) and (107). Expressions (156*b*) and (157*b*) are usually more convenient than expressions (156*a*) and (157*a*).

The transformation from the original to the down-folded basis set is

according to (34*c*)

$$|\bar{\bar{\chi}}^{\mathrm{L}}\rangle^{\infty} = |\bar{\chi}^{\mathrm{L}}\rangle^{\infty} + |\bar{\chi}^{\mathrm{H}}\rangle^{\infty}(\bar{\bar{o}}^{\mathrm{H}} - \bar{o}^{\mathrm{H}})\,\bar{\bar{h}}^{\mathrm{HL}}\,, \tag{158}$$

where the matrix involved is

$$(\bar{\bar{o}}^{\mathrm{H}} - \bar{o}^{\mathrm{H}})\,\bar{\bar{h}}^{\mathrm{HL}} = [{}_{\nu}\bar{E}^{\mathrm{H}} - \bar{H}^{\mathrm{HH}(1)}]^{-1}\,\bar{h}^{\mathrm{HL}}\,, \tag{159a}$$

$$(\bar{\bar{o}}^{\mathrm{H}} - \bar{o}^{\mathrm{H}})\,\bar{\bar{h}}^{\mathrm{HL}} = (\bar{\Delta}^{\mathrm{H}})^{-\frac{1}{2}}\,\bar{F}^{\mathrm{HH}}({}_{\nu}E)\,\bar{S}^{\mathrm{HL}}(\bar{\Delta}^{\mathrm{L}})^{\frac{1}{2}}\,. \tag{159b}$$

This was obtained from (156*a*), (152) and (154). One way of constructing the down-folded overlap and Hamiltonian matrices,

$$\bar{\bar{O}}^{\mathrm{LL}} \equiv {}^{\infty}\langle\bar{\bar{\chi}}^{\mathrm{L}}|\bar{\bar{\chi}}^{\mathrm{L}}\rangle^{\infty} \quad \text{and} \quad \bar{\bar{H}}^{\mathrm{LL}} \equiv {}^{\infty}\langle\bar{\bar{\chi}}^{\mathrm{L}}|-\nabla^2 + V|\bar{\bar{\chi}}^{\mathrm{L}}\rangle^{\infty}\,, \tag{160}$$

is to start off from the full $\bar{O}$ (22) and $\bar{H}$ (25) and include the combined correction (114) and (120) and thereafter perform the transformation (158). This is a general but computationally heavy method, in contrast to the simple energy-dependent ASA method mentioned in connection with (150), and it should only be used if one of the last two terms, $|\dot{\bar{\bar{\varphi}}}^{\mathrm{H}}\rangle\,\bar{\bar{h}}^{\mathrm{HL}} + |\bar{\bar{\chi}}^{\mathrm{Li}}\rangle^{\infty}$, of the MTO (132) give substantial contributions. That is, if the down-folding or the combined-correction terms, or both, are large.

When this is not the case, it is usually advantageous to orthogonalize the down-folded set approximately by application of the further transformation (27):

$$\begin{aligned}|\bar{\bar{\chi}}^{\mathrm{L}}\rangle^{\infty}(I + \bar{o}^{\mathrm{L}}\bar{\bar{h}}^{\mathrm{LL}})^{-1} &= |\bar{\bar{\chi}}^{\mathrm{L}}\rangle^{\infty}(I - \bar{o}^{\mathrm{L}}\bar{\bar{h}}^{\mathrm{LL}} + \bar{o}^{\mathrm{L}}\bar{\bar{h}}^{\mathrm{LL}}\bar{o}^{\mathrm{L}}\bar{\bar{h}}^{\mathrm{LL}} - \ldots) \equiv \\ &\equiv |\tilde{\bar{\chi}}^{\mathrm{L}}\rangle^{\infty} = |\varphi^{\mathrm{L}}\rangle + |\dot{\varphi}^{\mathrm{L}}\rangle\,\tilde{h}^{\mathrm{LL}} + |\dot{\bar{\bar{\varphi}}}^{\mathrm{H}}\rangle\,\tilde{h}^{\mathrm{HL}} + |\tilde{\bar{\chi}}^{\mathrm{Li}}\rangle^{\infty}\,,\end{aligned} \tag{161}$$

where, from (132),

$$\begin{aligned}\tilde{H}^{\mathrm{LL}(2)} \equiv E_{\nu}^{\mathrm{L}} + \tilde{h}^{\mathrm{LL}} &= E_{\nu}^{\mathrm{L}} + \bar{\bar{h}}^{\mathrm{LL}}(I + \bar{o}^{\mathrm{L}}\bar{\bar{h}}^{\mathrm{LL}})^{-1} = \\ &= \bar{\bar{H}}^{\mathrm{LL}(1)} - \bar{\bar{h}}^{\mathrm{LL}}\bar{o}^{\mathrm{L}}\bar{\bar{h}}^{\mathrm{LL}} + \bar{\bar{h}}^{\mathrm{LL}}\bar{o}^{\mathrm{L}}\bar{\bar{h}}^{\mathrm{LL}}\bar{o}^{\mathrm{L}}\bar{\bar{h}}^{\mathrm{LL}} - \ldots = \\ &= C^{\mathrm{L}} + (\Delta^{\mathrm{L}})^{\frac{1}{2}}\,\bar{\bar{S}}^{\mathrm{LL}}({}_{\nu}E)[I - (Q^{\mathrm{L}} - \bar{Q}^{\mathrm{L}})\,\bar{\bar{S}}^{\mathrm{LL}}({}_{\nu}E)]^{-1}(\Delta^{\mathrm{L}})^{\frac{1}{2}}\,.\end{aligned} \tag{162}$$

Here, $\bar{\bar{h}}^{\mathrm{LL}}$ was given in (157) and $\bar{\bar{S}}^{\mathrm{LL}}$ in (143). Moreover,

$$\begin{aligned}\bar{\bar{o}}^{\mathrm{H}}\,\tilde{h}^{\mathrm{HL}} \equiv \bar{\bar{o}}^{\mathrm{H}}\bar{\bar{h}}^{\mathrm{HL}}(I + \bar{o}^{\mathrm{L}}\bar{\bar{h}}^{\mathrm{LL}})^{-1} &= \\ = \bar{\bar{o}}^{\mathrm{H}}\bar{\bar{h}}^{\mathrm{HL}} - \bar{\bar{o}}^{\mathrm{H}}\bar{\bar{h}}^{\mathrm{HL}}\bar{o}^{\mathrm{L}}\bar{\bar{h}}^{\mathrm{LL}} + \bar{\bar{o}}^{\mathrm{H}}\bar{\bar{h}}^{\mathrm{HL}}\bar{o}^{\mathrm{L}}\bar{\bar{h}}^{\mathrm{LL}}\bar{o}^{\mathrm{L}}\bar{\bar{h}}^{\mathrm{LL}} - \ldots\,.\end{aligned} \tag{163}$$

The nearly orthogonal down-folded representation (161) has the overlap matrix

$$\tilde{O}^{\mathrm{LL}} = I + \tilde{h}^{\mathrm{LL}}\,p^{\mathrm{L}}\,\tilde{h}^{\mathrm{LL}} + \tilde{h}^{\mathrm{LH}}(\bar{\bar{o}}^{\mathrm{H}})^2\,\tilde{h}^{\mathrm{HL}} + {}^{\infty}\langle\chi^{\mathrm{Li}}|\chi^{\mathrm{Li}}\rangle^{\infty} \tag{164}$$

and, due to the third term, this representation is less orthogonal than the nonfolded representation (27). It is, however, not possible to apply our analytical Löwdin orthogonalization further because it is based on having, in each sphere and for each angular momentum, a *local* orthogonal set from which we then build the nearly orthogonal *orbital* set. (In (164) we have, due to the very small by-mixing of $\dot{\varphi}_H(r)$ to $\dot{\bar{\varphi}}_H(r)$, neglected the term proportional to p_H.) The Hamiltonian matrix is

$$\tilde{\boldsymbol{H}}^{\mathrm{LL}} = \tilde{\boldsymbol{H}}^{\mathrm{LL}(2)} + \tilde{\boldsymbol{h}}^{\mathrm{LL}} \boldsymbol{p}^{\mathrm{L}} \boldsymbol{E}_\nu^{\mathrm{L}} \tilde{\boldsymbol{h}}^{\mathrm{LL}} + \tilde{\boldsymbol{h}}^{\mathrm{LH}} (\boldsymbol{I} + \bar{\boldsymbol{o}}^{\mathrm{H}} \boldsymbol{E}_\nu^{\mathrm{H}}) \bar{\boldsymbol{o}}^{\mathrm{H}} \tilde{\boldsymbol{h}}^{\mathrm{HL}} + {}^{\infty}\langle \tilde{\chi}^{\mathrm{Li}} | V | \tilde{\chi}^{\mathrm{Li}} \rangle^{\infty} . \tag{165}$$

If all E_ν's are the same, we can measure all energies relatively to this E_ν and hence drop the terms proportional to E_ν. This was mentioned in connection with (25). Moreover, in connection with (156*a*) it was mentioned that, if all E_ν's are the same, then $\bar{\boldsymbol{h}}^{\mathrm{HL}}$ vanishes, while $\bar{\boldsymbol{o}}^{\mathrm{H}} \bar{\boldsymbol{h}}^{\mathrm{HL}}$ remains finite. This also applies to $\tilde{\boldsymbol{h}}^{\mathrm{HL}}$, as seen from (163). Consequently, also the term $\tilde{\boldsymbol{h}}^{\mathrm{LH}} \bar{\boldsymbol{o}}^{\mathrm{H}} \tilde{\boldsymbol{h}}^{\mathrm{HL}}$ in (165) vanishes and as a result only $\tilde{\boldsymbol{H}}^{\mathrm{LL}(2)}$ plus the last, combined-correction term remain in the expression for the Hamiltonian matrix, *i.e.*

$$\tilde{\boldsymbol{H}}^{\mathrm{LL}} \approx \tilde{\boldsymbol{H}}^{\mathrm{LL}(2)} + {}^{\infty}\langle \tilde{\chi}^{\mathrm{Li}} | V | \tilde{\chi}^{\mathrm{Li}} \rangle^{\infty} . \tag{166}$$

This is exactly the result anticipated in our much simpler KKR-ASA treatment which resulted in the energy-dependent orthogonal Hamiltonian $\tilde{\boldsymbol{H}}^{\mathrm{LL}}(E)^{(2)}$. What is achieved with the variational LMTO method, apart from the possibility of going beyond the ASA, is to fix the energy of the ASA Hamiltonian at $_\nu E$ (see (157) and (138)) and then to re-introduce the energy dependence via the overlap matrix (see (164) and (156)). This is why the nonorthogonality is essential, except at E_ν.

If in the overlap matrix (164) the three last terms are much smaller than unity, then we may treat them by first-order perturbation theory like in (33). A more accurate procedure is the one similar to (89) which is based on approximate Löwdin orthogonalization specified by the matrix

$$(\tilde{\boldsymbol{O}}^{\mathrm{LL}})^{-\frac{1}{2}} \approx \boldsymbol{I} - \tfrac{1}{2} \tilde{\boldsymbol{h}}^{\mathrm{LL}} \boldsymbol{p}^{\mathrm{L}} \tilde{\boldsymbol{h}}^{\mathrm{LL}} - \tfrac{1}{2} \tilde{\boldsymbol{h}}^{\mathrm{LH}} (\bar{\boldsymbol{o}}^{\mathrm{H}})^2 \tilde{\boldsymbol{h}}^{\mathrm{HL}} - \tfrac{1}{2} {}^{\infty}\langle \dot{\tilde{\chi}}^{\mathrm{Li}} | \tilde{\chi}^{\mathrm{Li}} \rangle^{\infty} . \tag{167}$$

With this procedure the energy bands are obtained by diagonalization of the Hamiltonian

$$\boldsymbol{H}^{\mathrm{LL}(3)} \equiv (\bar{\bar{\boldsymbol{O}}}^{\mathrm{LL}})^{-\frac{1}{2}} \bar{\bar{\boldsymbol{H}}}^{\mathrm{LL}} (\bar{\bar{\boldsymbol{O}}}^{\mathrm{LL}})^{-\frac{1}{2}} = (\tilde{\boldsymbol{O}}^{\mathrm{LL}})^{-\frac{1}{2}} \tilde{\boldsymbol{H}}^{\mathrm{LL}} (\tilde{\boldsymbol{O}}^{\mathrm{LL}})^{-\frac{1}{2}} . \tag{168}$$

In our down-folding formalism *only two* higher potential parameters enter, namely the values of the potential function and its energy derivative, $\bar{P}_H(_\nu E)^{(2)}$ and $\dot{\bar{P}}_H(_\nu E)^{(2)}$, at the chosen energy $_\nu E$. This is seen in (156*b*), (157*b*) and (138). For similar materials, the higher potential functions are rather similar such

that, if we choose *the same* value $\bar{P}_H$ for all these materials and use

$$(155) \qquad {}_{\nu}E = C_H + \frac{\Delta_H}{\bar{P}_H^{-1} - (Q_H - \bar{Q}_H)} = C_H + \frac{\Delta_H}{P_H^{-1} - Q_H}$$

and (from (107))

$$(169) \qquad [-\partial \bar{P}_H(E)^{-1}/\partial E]_{{}_{\nu}E}^{\frac{1}{2}} = \frac{\dot{\bar{P}}_H^{\frac{1}{2}}}{\bar{P}_H} = \frac{\dot{P}_H^{\frac{1}{2}}}{P_H} = \frac{\Delta_H^{\frac{1}{2}}}{{}_{\nu}E - C_H} = \frac{\bar{P}_H^{-1} + \bar{Q}_H - Q_H}{\Delta_H^{\frac{1}{2}}} = \frac{P_H^{-1} - Q_H}{\Delta_H^{\frac{1}{2}}}$$

as the two potential parameters characterizing each individual material, then these ${}_{\nu}E$'s still fall « within the range of interest » and the scheme is sufficiently accurate. Fixing $\bar{P}_H({}_{\nu}E)$ has the advantage that the most involved part of the down-folding (the calculation of $\bar{\boldsymbol{F}}^{\mathrm{HH}}$ defined in (138) and used in (156*b*) and (157*b*), plus the subsequent construction of the down-folded short-range structure matrix $\bar{\bar{\boldsymbol{S}}}^{\mathrm{LL}}$ defined in (143) and used in (157*b*)) can be performed once and for all for a given class of materials and structure. In other words, a canonical description can been regained. The formalism becomes particularly simple, and the localization unaffected, if we can choose $\bar{P}_H = \infty$. This is equivalent to taking $\bar{\bar{Q}}_H = \bar{Q}_H$ and, consequently, the lower orbitals and the Hamiltonian matrix are unchanged. Merely the overlap matrix is modified.

The higher radial wave function often has the « off-resonance » or « free-electron » behaviour (127) and this means that the square-well pseudopotential V_H (see (79) and (105)) lies in the energy range of interest and that the value of Γ_H (see (81)-(83) and (105)) corresponds to an intrinsic band mass τ_H not far from unity. This, for instance, holds for *d*-functions in simple metals and for the *s*-, *p*- and *d*-functions in « vacancy potentials ». In such cases it is natural to choose $P_H = \infty$, or equivalently

$$(170) \qquad {}_{\nu}E = V_H \,,$$

and

$$(171) \qquad \dot{\bar{P}}_H^{\frac{1}{2}} \bar{P}_H^{-1} = -\Gamma_H^{-\frac{1}{2}} \,.$$

The down-folding (143) of the structure matrix is thus a *partial unscreening* and the result, if calculated exactly, is the same as would have been obtained in a screening calculation starting from the bare structure matrix but including only the LL block. If the square-well pseudopotential essentially equals the value $v(s)$ of the potential at the sphere and the intrinsic band mass is close to unity, one only needs to calculate the LL block of the partially unscreened structure matrix, while the remaining terms of the down-folded Hamiltonian and overlap matrices may be taken care of by the combined-correction term (subsect. 4·8) containing LL-matrices only.

4'13. *Ghost bands.* – There are cases in which the removal of redundant orbitals from the linear basis set is not only a convenient way of reducing the matrix size but is even a necessity. Otherwise false roots, so-called ghost bands, occur. In order to understand this, let us consider the case of Cd and suppose that we are interested in the *sp*-like energy bands around the Fermi level and, therefore, choose all $E_\nu \equiv E_F$. Then the LMTO method with *s*-, *p*- and *d*-orbitals might become schizophrenic because, with only five *d*-orbitals, it cannot decide whether to describe the $4d$-bands far below E_ν or the $5d$-bands far above E_ν. As a result, the LMTO method might pick out the top of the $4d$-bands together with the bottom of the $5d$-bands *and* connect the two by a steep ghost band crossing through the energy range of interest.

The obvious cure for this schizophrenia is to choose $E_{\nu d}$ closer to the $4d$- *or* closer to the $5d$-bands, whereby only the nearest band will be picked and the ghost band will disappear. This procedure is, however, not optimal, first of all, because with $E_{\nu d}$ far from E_F the weak *d*-hybridization of the *sp*-bands near E_F is not described in the most accurate way and, secondly, because the matrix size is larger than necessary.

The better cure is, therefore, to eliminate the *d*-orbitals through downfolding, *e.g.* with $\bar{P}_H = \infty$, as explained in the previous subsection. In this way the energy dependence of the inverse of the *d* potential function is only correct to first order in $E - {}_\nu E$. This is, however, sufficient in this case in which ${}_\nu E$ lies *between* resonances.

From the formal point of view a ghost arises from a nearly singular behaviour of $\boldsymbol{H}^{(2)}$ defined in (65), or rather of $\tilde{\boldsymbol{S}}$ given by (66), and the associated long-ranged oscillations of the orthogonal orbitals. This is caused by the vanishing of the determinant of some subblock $(\boldsymbol{Q}^H)^{-1} - \boldsymbol{S}^{HH}$. Considering the fact that the zeros of $\det[\boldsymbol{P}(E) - \boldsymbol{S}]$ give the energy bands in the ASA, that $P(E)$ is a never decreasing, cotangentlike function of energy, that

$$P(E) \equiv \frac{W\{K, \varphi(E)\}}{W\{J, \varphi(E)\}}, \tag{95}$$

while

$$Q^{-1} \equiv \frac{W\{K, \dot{\varphi}(E_\nu)\}}{W\{J, \dot{\varphi}(E_\nu)\}}, \tag{64}$$

and that $\varphi(E)$ and $\dot{\varphi}(E)$ are oscillating functions of energy « phase shifted » with respect to each other, it is obvious that Q^{-1} considered as a function of E_ν behaves like $P(E)$, but shifted in energy. Consequently, there are E_ν ranges where $\det[(\boldsymbol{Q}^H)^{-1} - \boldsymbol{S}^{HH}]$ vanishes and they occur when the logarithmic derivative of phi-dot is negative, *i.e.* they follow the Wigner-Seitz rules—for phi-dot though—mentioned in sect. **2**. The fact that usually a ghost band, rather than a divergence, develops in the energy bands is due to « damping » from the remaining blocks of $\boldsymbol{Q}^{-1} - \boldsymbol{S}$.

4'14. *Comparison to the traditional* LMTO-ASA *and* ASW *methods.* – The analytical transformation of the unscreened MTOs to a nearly orthogonal set is fairly recent [12] and has only been applied in a few calculations [46-51], first of all, in connection with solutions of the impurity problem [46]. The most localized representation is presented here for the first time, and it has so far only been applied to amorphous metals [41] in connection with the recursion method [42]. All other solid-state applications have been of the traditional LMTO-ASA method [6-10] or of its closely related descendant, the ASW method [11].

The traditional procedure involves computation of the *bare* structure matrix $\boldsymbol{S}^{k}$ on a $\boldsymbol{k}$-space mesh using (46) plus the Ewald method for evaluation of the lattice sums (86). Then, for given atomic-sphere potentials, one solves the radial Schrödinger equations and obtains for all R and l the potential parameters ${}^{0}C$, ${}^{0}\Delta$ and ${}^{0}o$, corresponding to the choice $\bar{Q} = 0$, plus p. From ${}^{0}\boldsymbol{C}$ and ${}^{0}\boldsymbol{\Delta}$ and the bare structure matrix one then constructs ${}^{0}\boldsymbol{H}^{(1)} \equiv {}^{0}\boldsymbol{C} + {}^{0}\boldsymbol{\Delta}^{\frac{1}{2}}\boldsymbol{S}\,{}^{0}\boldsymbol{\Delta}^{\frac{1}{2}}$ according to (63) and, from (22) and (25), the overlap and Hamiltonian matrices are formed using ${}^{0}\boldsymbol{h} = {}^{0}\boldsymbol{H}^{(1)} - \boldsymbol{E}_{\nu}$, ${}^{0}\boldsymbol{o}$ and $\boldsymbol{p}$. The traditional combined-correction term [6], which is far more involved than the version presented in subsect. 4'8, may be added. The eigenvalue problem (4) is finally solved by *numerical* Cholesky factorization of the overlap matrix and reduction of the transformed Hamiltonian to a real symmetric tridiagonal matrix [35].

The essential differences between the traditional LMTO-ASA method and the ASW method are, firstly, that the ASWs are augmented by the radial-Schrödinger-equation solutions, $\varphi(V, r)$ and $\varphi(C, r)$, which match onto the spherical Bessel and Hankel functions, $J(r)$ and $K(r)$, respectively. This approximation to $\varphi(E, r)$ by the *chord* at the *fixed* points V and C is less flexible and (usually) less accurate than the phi–phi-dot approximation by the *tangent* at the arbitrary point E_{ν} used in the LMTO method. Secondly, in the ASW method the overlap integral in the cell (rather than in the sphere) is computed from the $\varkappa^2$ derivative of the bare structure matrix in the same way as that used in the standard KKR method for normalization of the wave function. This procedure is simpler than the *traditional* combined correction used in the LMTO method, but it does not correct for the neglect of the higher partial waves.

The advantages of the new localized LMTO method, which in principle gives the same numerical results as the traditional method, are the following. The orbitals have short range and there are no Ewald summations to be done. This makes calculations for nonperiodic systems possible. Moreover, the Löwdin orthogonalization may conveniently be performed via the power series (88) and (89). The nonspheridized charge density and the combined correction to the ASA are relatively simple to calculate, and the atomic spheres may even be substituted by muffin-tin spheres and fairly large non-MT corrections to the potential may be included. Conceptually the new canonical tight-binding formulation is even simpler than the traditional canonical formulation.

5. – Energy bands of elemental metals.

In the preceding sections we have developed a simple orbital theory for self-consistent electronic-structure calculations in closely packed systems. Most modern applications of the traditional LMTO-ASA and ASW methods, which are based on this theory, aim towards an understanding of phase diagrams and, so far, involve zero-temperature calculations of pressure-volume relations, structural-energy differences and interatomic forces, heats of formation of alloys and of $3d$ magnetic moments and structures. One of the first applications of the LMTO-ASA method was to self-consistent local-density [52] calculations of the equilibrium lattice constants and bulk moduli, as well as of the spin magnetic moments and susceptibilities, for the 33 elemental metals K $\rightarrow$ Cu, Rb $\rightarrow$ Ag and Cs $\rightarrow$ Au [2, 3, 53]. These results agree with those [54] obtained for the K and Rb rows with the far more elaborate KKR method [16]. The Fermi surfaces arising from these ground-state calculations are generally in good agreement with the wealth of existing detailed dHvA data [2] and, for the nonmagnetic metals, also the energy bands show good resemblance with those deduced from angular resolved photoemission experiments [55]. We shall now review the band structures of these elemental metals as the simplest application of the concepts defined in the previous sections of the paper.

The canonical, most localized hopping integrals $\bar{S}$ were listed in tables I and II and the self-consistent potential parameters C, Δ, Q, p and E_ν are listed in table III. The results for ferromagnetic Fe, Co and Ni are given in table IV. Each $E_{\nu l}$ has been chosen to lie at the centre of gravity of the occupied part of the l-projected band such that $m_l^{(1)} = 0$ in (39). Moreover, in the elemental metals $w \equiv s$, where the experimental values of the Wigner-Seitz radius may be found in tables V and VI. The information in tables I-IV thus suffices to construct the band structures of the elemental metals using manipulations of, at most, 9×9 matrices, or 18×18 matrices for the h.c.p. structure. In the ASA, and to second order in $E - E_\nu$, we have the following three simple possibilities.

The first one is to transform the unbarred potential parameters in tables III-IV into the barred ones using

$$\text{(90)-(91)} \qquad \frac{\bar{\Delta}^{\frac{1}{2}}}{\Delta^{\frac{1}{2}}} = \frac{\bar{C} - E_\nu}{C - E_\nu} = 1 - (Q - \bar{Q}) \frac{C - E_\nu}{\Delta} = -\frac{Q - \bar{Q}}{\Delta} \frac{1}{\bar{o}}$$

and then form the first-order Hamiltonian

$$\text{(63)} \qquad \bar{\boldsymbol{H}}^{(1)} = \boldsymbol{E}_\nu + \bar{\boldsymbol{h}} = \bar{\boldsymbol{C}} + \bar{\boldsymbol{\Delta}}^{\frac{1}{2}} \bar{\boldsymbol{S}} \bar{\boldsymbol{\Delta}}^{\frac{1}{2}}$$

TABLE III. – *Potential parameters at experimental equilibrium atomic volume.*

		K Rb Cs	Ca Sr Ba	Sc Y Lu	Ti Zr Hf	V Nb Ta	Cr Mo W	Mn Tc Re	Fe Ru Os	Co Rh Ir	Ni Pd Pt	Cu Ag Au
E_ν (mRyd)	s	−270	−340	−351	−351	−350	−374	−438	−474	−497	−521	−545
		−260	−320	−337	−337	−329	−352	−381	−424	−485	−537	−545
		−243	−271	−377	−397	−399	−433	−464	−504	−565	−620	−638
	p	−247	−286	−264	−233	−223	−227	−290	−325	−346	−370	−404
		−241	−282	−260	−226	−208	−209	−235	−277	−348	−422	−450
		−229	−246	−271	−242	−223	−225	−246	−285	−354	−435	−491
	d	−233	−257	−222	−207	−198	−215	−248	−263	−272	−282	−357
		−226	−250	−229	−219	−211	−240	−245	−277	−330	−387	−509
		−214	−222	−230	−224	−209	−242	−242	−269	−320	−383	−471
	f	−214	−251	−251	−184	−177	−185	−233	−256	−264	−281	−359
		−163	−220	−217	−190	−184	−197	−216	−242	−302	−375	−496
		−212	−219	−223	−193	−180	−193	−206	−220	−274	−357	−465
$C - E_\nu$ (mRyd)	s	31	16	74	136	188	215	184	182	174	161	105
		21	2	50	106	161	189	200	205	192	171	89
		18	27	10	45	80	95	98	99	92	76	27
	p	347	418	642	837	1011	1099	1038	1053	1067	1063	961
		334	400	607	804	1005	1092	1140	1160	1116	1047	878
		308	473	645	804	982	1052	1094	1118	1086	1020	911
	d	468	306	238	215	189	157	104	71	50	30	11
		392	300	276	266	251	214	155	107	60	23	0
		266	236	337	319	302	264	197	143	84	34	2
	f	1160	1747	2422	3011	3552	3733	3999	3946	4367	4494	4415
		920	1181	1634	2012	2378	2656	2814	2967	3112	3061	2998
		771	989	1913	2225	2533	2707	2827	2908	2925	2991	2899
$20\,\Delta$ (mRyd)	s	1031	1468	2318	2036	3611	3958	3743	3744	3772	3719	3325
		910	1256	1981	2629	3207	3542	3701	3755	3561	3223	2702
		797	1323	2009	2544	3040	3302	3433	3480	3317	2988	2562
	p	1045	1423	2171	2805	3320	3624	3446	3466	3507	3482	3162
		970	1286	1957	2567	3129	3425	3566	3615	3447	3165	2705
		868	1386	2099	2617	3117	3371	3507	3569	3441	3167	2796
	d	621	411	394	414	418	397	319	280	256	230	174
		544	469	541	614	667	651	601	539	440	337	220
		386	449	646	715	783	773	728	672	569	448	325

TABLE III. – (*Continued*).

		K Rb Cs	Ca Sr Ba	Sc Y Lu	Ti Zr Hf	V Nb Ta	Cr Mo W	Mn Tc Re	Fe Ru Os	Co Rh Ir	Ni Pd Pt	Cu Ag Au
$20\,\Delta$ (mRyd)	f	831	1630	2300	2867	3366	3292	3740	3416	4046	4146	4022
		640	851	1278	1649	1980	2254	2325	2429	2587	2385	2221
		549	829	1603	1923	2220	2363	2451	2498	2443	2523	2280
$Q\times$ $\times 2(2l+1)\cdot$ $\cdot 10^3$	s	846	846	860	866	869	868	863	860	857	853	845
		847	848	863	871	875	876	874	872	868	862	850
		852	865	854	861	866	867	866	864	860	854	843
	p	694	685	702	711	715	711	697	691	687	682	671
		711	706	728	746	758	753	744	733	720	709	693
		727	758	722	736	749	746	740	734	723	712	700
	d	469	283	173	128	94	67	33	10	— 6	— 21	— 29
		472	354	285	251	225	195	159	129	97	69	56
		431	351	314	285	265	240	207	179	146	113	88
	f	402	561	553	550	550	508	556	514	562	565	571
		331	360	405	424	434	449	441	444	471	455	458
		405	448	466	467	469	464	461	458	454	483	471
$p^{-\frac{1}{2}}$ (mRyd)	s	1300	1840	3100	4200	5070	5560	5120	5060	5030	5870	4190
		1150	1590	2710	3750	4690	5200	5420	5460	5080	4490	3560
		1040	1840	2640	3490	4280	4680	4850	4990	4580	4030	3300
	p	2000	2670	4000	5020	5900	6550	6470	6570	6660	6600	5920
		1880	2470	3500	4250	4890	5560	6130	6580	6640	6280	5330
		1680	2280	3960	4700	5320	5880	6330	6690	6730	6360	5620
	d	1190	810	850	950	1000	1000	860	800	770	730	610
		1120	960	1140	1320	1460	1460	1390	1290	1110	930	710
		810	960	1360	1530	1700	1710	1640	1540	1360	1140	910

using the localized structure matrix. *This Hamiltonian has the two-centre tight-binding form.* From it we may then form the second-order Hamiltonian

$$\boldsymbol{H}^{(2)} = \boldsymbol{E}_\nu + \bar{\boldsymbol{h}}(\boldsymbol{I} + \bar{\boldsymbol{o}}\bar{\boldsymbol{h}})^{-1}\,, \tag{28}$$

$$\boldsymbol{H}^{(2)} = \bar{\boldsymbol{H}}^{(1)} - \bar{\boldsymbol{h}}\bar{\boldsymbol{o}}\bar{\boldsymbol{h}} + \bar{\boldsymbol{h}}\bar{\boldsymbol{o}}\bar{\boldsymbol{h}}\bar{\boldsymbol{o}}\bar{\boldsymbol{h}} - \ldots\,, \tag{88}$$

and perhaps even the third-order Hamiltonian (89), which is then diagonalized. The second possibility is to use the unbarred potential parameters from the

TABLE IV. – *Potential parameters at experimental equilibrium atomic volume.*

		↑ Fe	↓	↑ Co	↓	↑ Ni	↓
E_ν (Ryd)	s	−0.486	−0.444	−0.505	−0.478	−0.523	−0.516
	p	−0.351	−0.283	−0.367	−0.313	−0.379	−0.359
	d	−0.274	−0.242	−0.292	−0.248	−0.295	−0.273
	f	−0.273	−0.220	−0.296	−0.235	−0.300	−0.267
$C - E_\nu$ (Ryd)	s	0.181	0.173	0.174	0.165	0.160	0.157
	p	1.065	1.033	1.080	1.044	1.070	1.053
	d	0.028	0.146	0.019	0.090	0.019	0.041
	f	3.949	3.932	4.402	4.334	4.518	4.475
$20\,\Delta$ (Ryd)	s	3.719	3.781	3.749	3.799	3.709	3.728
	p	3.453	3.485	3.497	3.517	3.478	3.484
	d	0.260	0.327	0.241	0.281	0.224	0.237
	f	3.397	3.442	4.054	4.040	4.154	4.141
$Q \times 2(2l+1)$	s	0.859	0.860	0.856	0.857	0.853	0.853
	p	0.691	0.692	0.687	0.686	0.682	0.681
	d	−0.012	0.046	−0.019	0.011	−0.024	−0.016
	f	0.513	0.516	0.563	0.561	0.565	0.564
$p^{-\frac{1}{2}}$ (Ryd)	s	5.017	5.101	4.991	5.052	4.857	4.882
	p	6.561	6.570	6.651	6.648	6.593	6.589
	d	0.764	0.888	0.744	0.814	0.714	0.737
	f	10.228	10.404	∞	∞	∞	∞

tables and directly form

$$\boldsymbol{H}^{(2)} \equiv \boldsymbol{E}_\nu + \boldsymbol{h} = \boldsymbol{C} + \boldsymbol{\Delta}^{\frac{1}{2}}\,\tilde{\boldsymbol{S}}\,\boldsymbol{\Delta}^{\frac{1}{2}} \tag{65}$$

with $\tilde{\boldsymbol{S}}$ obtained from (66), or from (87), *i.e.*

$$\tilde{\boldsymbol{S}} = \boldsymbol{S}[\boldsymbol{I} - \boldsymbol{Q}\boldsymbol{S}]^{-1} = \overline{\boldsymbol{S}}[\boldsymbol{I} - (\boldsymbol{Q} - \overline{\boldsymbol{Q}})\,\overline{\boldsymbol{S}}]^{-1} = \tag{172}$$

$$= \overline{\boldsymbol{S}} + \overline{\boldsymbol{S}}(\boldsymbol{Q} - \overline{\boldsymbol{Q}})\,\overline{\boldsymbol{S}} + \overline{\boldsymbol{S}}(\boldsymbol{Q} - \overline{\boldsymbol{Q}})\,\overline{\boldsymbol{S}}(\boldsymbol{Q} - \overline{\boldsymbol{Q}})\,\overline{\boldsymbol{S}} + \ldots .$$

The third possibility illustrated in fig. 8 is to use the KKR-ASA equations (100), which give the energy bands as the solutions of

$$\det\,[\overline{\boldsymbol{P}}(E) - \overline{\boldsymbol{S}}] = 0\,, \tag{173}$$

TABLE V. – *Band parameters at experimental equilibrium atomic volume.*

		K Rb Cs	Ca Sr Ba	Sc Y Lu	Ti Zr Hf	V Nb Ta
s_{exp} (a.u.)		4.862	4.122	3.427	3.052	2.818
		5.197	4.494	3.761	3.347	3.071
		5.656	4.652	3.624	3.301	3.069
$n\left(\frac{\text{electrons}}{\text{atom}}\right)$	s	0.616	0.849	0.757	0.685	0.637
		0.633	0.905	0.795	0.715	0.657
		0.634	0.799	0.886	0.818	0.770
	p	0.309	0.656	0.674	0.722	0.693
		0.273	0.526	0.587	0.659	0.649
		0.237	0.334	0.645	0.768	0.776
	d	0.071	0.480	1.542	2.539	3.605
		0.084	0.544	1.575	2.536	3.579
		0.125	0.841	1.426	2.324	3.332
	f	0.004	0.015	0.027	0.054	0.065
		0.010	0.025	0.043	0.090	0.115
		0.004	0.026	0.043	0.090	0.122
	tot	1	2	3	4	5
$q\left(\frac{\text{electrons}}{\text{atom}}\right)$		1.14	2.16	2.76	3.13	3.26
		1.15	2.20	3.04	3.66	4.02
		1.16	2.24	3.12	3.88	4.40
v (mRyd)		−363	−501	−630	−724	−785
		−345	−468	−598	−699	−774
		−321	−457	−622	−719	−795
E_F (mRyd)		−199	−200	−166	−123	−111
		−197	−190	−166	−119	− 98
		−193	−187	−153	−115	− 90
r.m.s. $(E - E_v)$ (mRyd)	s	43	74	86	89	94
		40	66	74	77	85
		33	49	96	102	111
	p	35	66	82	90	93
		32	59	75	84	88
		27	42	102	113	119
	d	28	46	50	58	62
		25	41	49	63	72
		20	28	67	79	88
	f	38	43	48	52	57
		20	39	46	58	68
		9	83	65	72	80

Cr Mo W	Mn Tc Re	Fe Ru Os	Co Rh Ir	Ni Pd Pt	Cu Ag Au
2.684	2.699	2.662	2.621	2.602	2.669
2.992	2.840	2.791	2.809	2.873	3.005
2.945	2.872	2.825	2.835	2.897	3.002
0.624	0.646	0.633	0.644	0.651	0.699
0.649	0.650	0.641	0.631	0.616	0.687
0.760	0.766	0.764	0.759	0.759	0.801
0.776	0.785	0.751	0.740	0.721	0.733
0.795	0.791	0.788	0.746	0.653	0.667
0.937	0.958	0.962	0.928	0.839	0.782
4.518	5.489	6.528	7.533	8.551	9.505
4.407	5.399	6.400	7.464	8.601	9.556
4.138	5.087	6.055	7.095	8.217	9.276
0.082	0.080	0.088	0.083	0.077	0.063
0.149	0.160	0.171	0.159	0.130	0.090
0.165	0.189	0.219	0.218	0.188	0.141
6	7	8	9	10	11
3.40	3.22	3.06	2.93	2.78	2.54
4.36	4.27	4.14	3.76	3.23	2.75
4.86	4.92	4.89	4.58	4.04	3.45
—830	—812	—810	—811	—803	—766
—828	—844	—849	—821	—770	—706
—850	—871	—883	—863	—817	—755
— 62	—119	—125	—134	—150	—145
— 33	— 42	— 57	—109	—202	—186
— 15	— 6	— 4	— 36	—133	—165
105	112	113	123	128	154
104	114	121	118	108	155
128	142	155	153	144	171
103	108	107	115	118	136
104	115	122	118	103	146
133	147	156	156	143	153
74	82	87	88	88	75
92	117	127	124	111	83
105	138	153	156	146	121
70	71	75	79	78	72
93	108	119	115	99	89
101	121	141	144	131	108

TABLE VI. – *Band parameters at experimental equilibrium atomic volume.*

		↑ Fe	↓	↑ Co	↓	↑ Ni	↓
s_{exp} (a.u.)		2.662		2.621		2.602	
$n\left(\frac{\text{electrons}}{\text{atom}}\right)$	s	0.314	0.329	0.318	0.334	0.324	0.330
	p	0.355	0.406	0.349	0.406	0.350	0.376
	d	4.373	2.144	4.591	2.924	4.589	3.953
	f	0.048	0.031	0.041	0.037	0.039	0.039
	tot	5.090	2.910	5.299	3.701	5.302	4.698
$m\left(\frac{\text{spins}}{\text{atom}}\right)$		2.180		1.598		0.604	
$q\left(\frac{\text{electrons}}{\text{atom}}\right)$		3.058		2.946		2.781	
v (mRyd)		−805	−815	−804	−819	−800	−808
E_F (mRyd)		−127		−123		−139	
r.m.s. $(E - E_v)$ (mRyd)	s	122	117	129	126	132	129
	p	110	113	116	120	119	121
	d	97	67	93	83	89	87

where the second-order expression for the potential functions is

$$\bar{P}(E)^{(2)} = \frac{E-C}{\Delta}\left[1+(Q-\bar{Q})\frac{E-C}{\Delta}\right]^{-1} \tag{106}$$

and a third-order expression is

$$\bar{P}(E)^{(3)} = \bar{P}\big(E+p(E-E_v)^3\big)^{(2)}\,. \tag{174}$$

We now discuss the overall features of the band structures of the elemental metals using the factorization, exhibited above in (63), in (65) and (172) and in (173), into canonical hopping integrals, which only depend on structure but are independent of the potential and the lattice constant, and potential parameters. We first consider the canonical hopping integrals and, since for the most localized hopping $Q-\bar{Q}$ is usually so small that (88) or (172) converge fast, while this is generally not true for the bare unscreened hopping where $Q-\bar{Q}=Q$, we start our discussion with the most localized canonical hopping integrals. Then, because of the existence of simple analytical expressions (46)-(47) for the bare canonical hopping integrals, we consider these and we use them to verify the interpretation of the potential parameters V_s, V_p, τ_s, τ_p, C_d and μ_d given in subsect. 4·3. Having in this way obtained a feeling for how energy bands « are built » from canonical bands and potential parameters, we finally discuss the trends of the latter going through the rows of elemental metals.

5·1. *Canonical tight-binding bands.* – For closely packed elemental metals with 8 or 12 nearest neighbours of the same kind the environment of each atom is so isotropic that the *magnitude* of angular momentum is fairly well conserved. This means that the s-, p- and d-bands mix relatively little and, in order to describe the rough features of the band structures, we now neglect the ll'-hybridization in the sense of dropping the off-diagonal blocks in (63). (We note that this is not quite equivalent to dropping the interactions between the l- and l'-localized MTOs because that would require dropping the off-diagonal blocks of the *full* Hamiltonian and overlap matrices.) Since for elemental metals and in the ASA the potential parameters are independent of R and m, the neglect of the off-diagonal ll' blocks of $\bar{\boldsymbol{H}}^{(1)}$ is equivalent with dropping the off-diagonal blocks of $\bar{\boldsymbol{S}}$. We may, therefore, independently of the potential and the lattice constant but for each crystal structure, diagonalize the ll-diagonal blocks of $\bar{\boldsymbol{S}}$ and obtain the *canonical tight-binding bands*, $\bar{S}^{\boldsymbol{k}}_{li}$, where the Block vector $\boldsymbol{k}$ runs over the Brillouin zone and i is a band index running from 1 to $(2l+1)M$ with M being the number of atoms in the primitive cell. The « unhybridized » l energy bands are then, to first order in

$E - E_{\nu l}$,

$$\bar{E}^k_{li} = \bar{C}_l + \bar{\Delta}_l \bar{S}^k_{li} \tag{175}$$

and, to second order,

$$E^k_{li} = E_{\nu l} + (\bar{E}^k_{li} - E_{\nu l})[1 + \bar{o}_l(\bar{E}^k_{li} - E_{\nu l})]^{-1}\,, \tag{176}$$

or equivalently, and in terms of the unbarred potential parameters,

$$E^k_{li} = C_l + \Delta_l \bar{S}^k_{li}[1 - (Q_l - \bar{Q}_l)\bar{S}^k_{li}]^{-1}\,. \tag{177}$$

To all orders in $E - E_{\nu l}$ we have the implicit equation

$$\bar{P}_l(E^k_{li}) = \bar{S}^k_{li} \tag{178}$$

with the potential functions being defined in terms of the logarithmic derivative function in (94) and (95).

The canonical s, p and d tight-binding bands for the f.c.c. and b.c.c. structures are shown in fig. 10 and 11 along the lines of high symmetry in the respective Brillouin zones. From the numerical values of the hopping integrals given in table I it is a trivial matter to obtain these bands. The canonical tight-

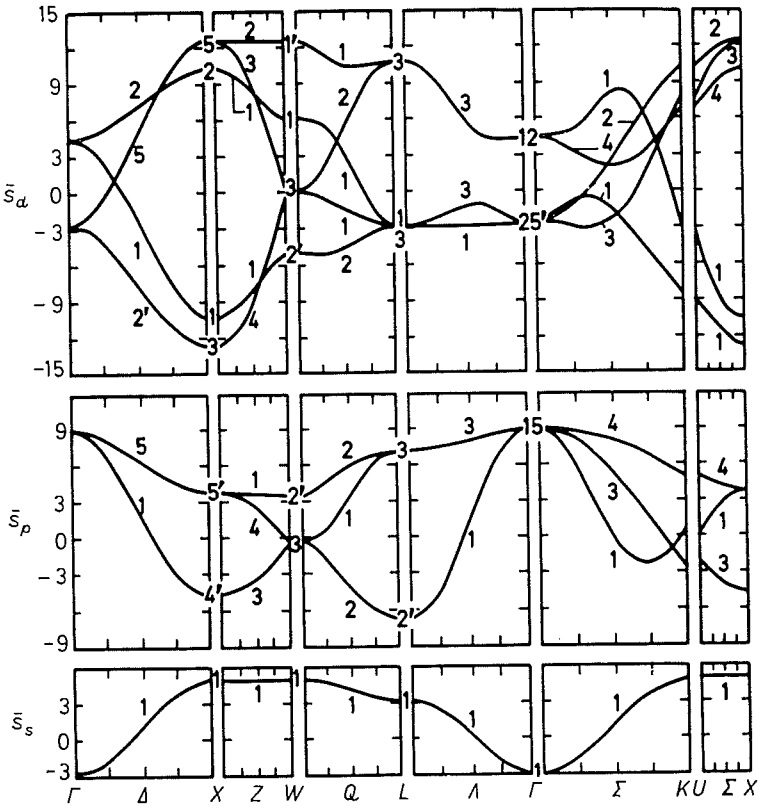

Fig. 10. – The screened canonical s-, p- and d-bands for the f.c.c. structure.

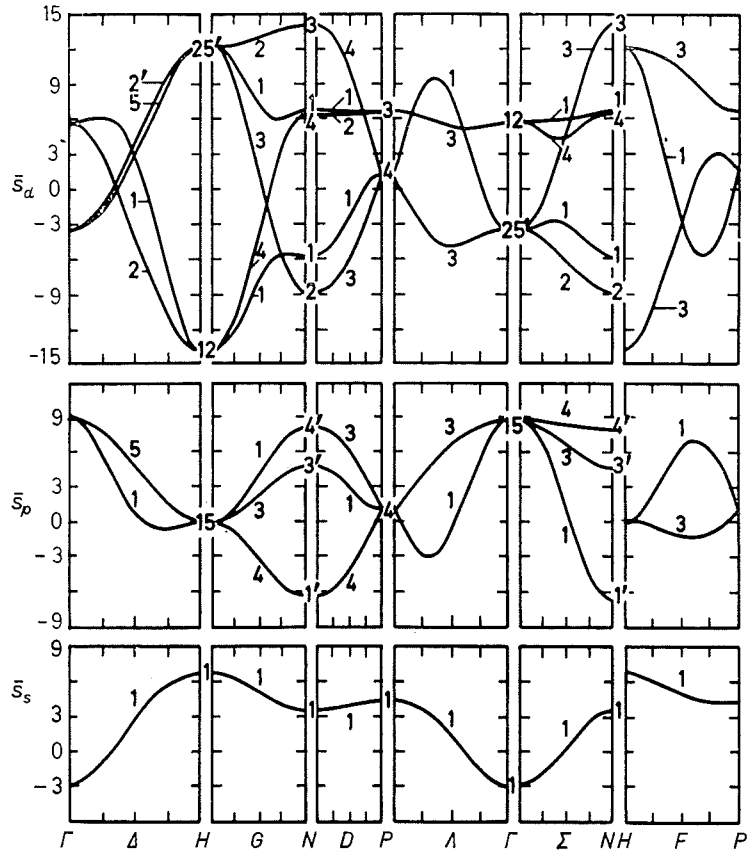

Fig. 11. – The screened canonical *s*-, *p*- and *d*-bands for the b.c.c. structure.

binding bands for the h.c.p. structure, which is the one most commonly found for the elemental metals, may be obtained using the hopping integrals in table II plus the rotation matrices tabulated by SLATER and KOSTER [38]. For comparison with the f.c.c. canonical tight-binding bands in fig. 10 we show in fig. 12 the full energy band structure of f.c.c. Ag [56].

The construction of an « unhybridized » energy band structure from a set of canonical tight-binding bands and the unbarred potential parameters that we have tabulated follow most simply from (177): The canonical l-bands are placed with their zero point at the energy C_l, they are then scaled with the energy Δ_l and, finally, they are distorted by the dimensionless parameter $Q_l - \bar{Q}_l$, which is of the order of 0.08, 0.07 and 0.01 for, respectively, the *s*-, *p*- and *d*-bands of the metals considered. The result of such a construction for b.c.c. vanadium is shown in the left-hand side of fig. 13.

Bands of different l's, but belonging to the same irreducible representation, can hybridize with each other, as seen by comparison of fig. 10 with fig. 12 and of the left-hand and right-hand sides of fig. 13. In order to describe this hybridization with the terminology used above, it is necessary first to include the off-diagonal blocks neglected in the inversion (172) of $\boldsymbol{I} - (\boldsymbol{Q} - \bar{\boldsymbol{Q}})\,\bar{\boldsymbol{S}}$. This has, in fact, been done in the left-hand side of fig. 13 and it leads to an

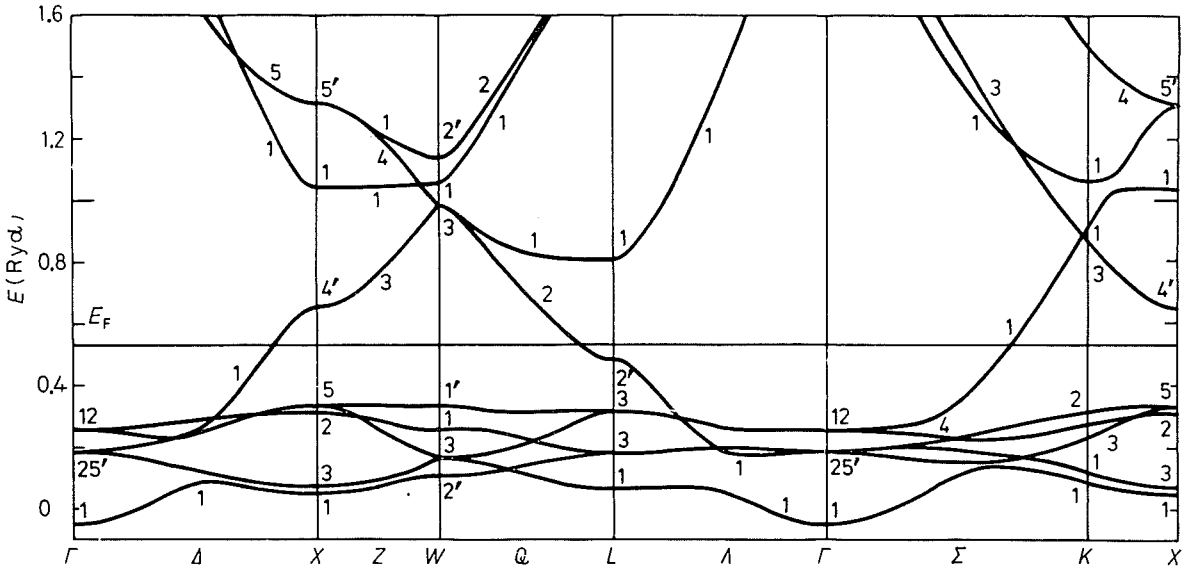

Fig. 12. – Relativistic band structure of Ag neglecting spin-orbit coupling, as calculated with the LAPW method and the self-consistent LD-ASA potential given in table III. The zero of energy is taken at $v(s) = -0.71$ Ryd.

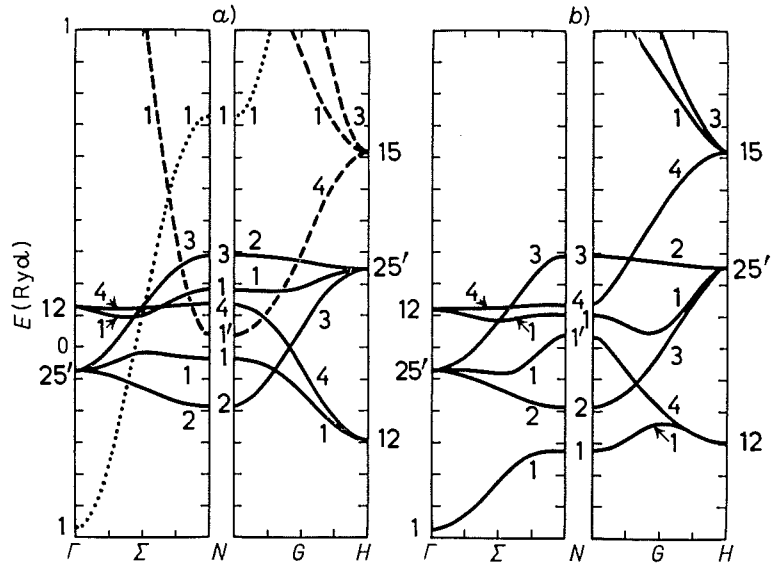

Fig. 13. – Unhybridized energy bands corresponding to the screening given by $Q_s = 0.435$, $Q_p = 0.0907$ and $Q_d = 0.0095$ (a)) and hybridized energy bands (b)) of b.c.c. vanadium.

unhybridized description in terms of the (potential-dependent) nearly orthogonal orbitals. Thereafter the hybridization would be included via the off-diagonal elements, $\Delta_l^{\frac{1}{2}} \tilde{S}^k_{li,l'i'} \Delta_{l'}^{\frac{1}{2}}$, of $\boldsymbol{H}^{(2)}$. An alternative—and presumably more consistent—procedure consists of defining the pure bands as the eigenvalues (175) of the diagonal blocks of the first-order tight-binding Hamiltonian $\bar{\boldsymbol{H}}^{(1)}$. The hybridization between these tight-binding bands is then described in the

normal way by the off-diagonal elements, $\bar{\Delta}_l^{\frac{1}{2}} \bar{S}^k_{li,l'i'} \bar{\Delta}_{l'}^{\frac{1}{2}}$, of $\bar{\boldsymbol{H}}^{(1)}$. Finally, the bands correct to second and third order in $E - E_\nu$ may be obtained by use of (88) and (89) in the li-representation.

We now return to the canonical tight-binding bands in fig. 10 and 11 and compare the position of the band edges with the predictions of the intuitive Wigner-Seitz rules mentioned in sect. **2**. According to these rules, the bottom of the l-band is at the « bonding » energy B for which the radial logarithmic derivative vanishes (11), and the top of the band is at the « antibonding » energy A for which the logarithmic derivative diverges (12). On P scale the range B/A, as obtained from (95), is $-\infty/2$, $-12/6$ and $-15/10$ for the s-, p- and d-functions, respectively. On the $\bar{P}$ scale (94), corresponding to the canonical tight-binding s-, p- and d-bands, the B/A range is, respectively, $-2.87/6.60$, $-7.33/8.80$ and $-12.92/11.20$. For the bottom of the s-band (Γ_1) the Wigner-Seitz rule is exact (provided that the structure is cubic and that partial waves with $l > 3$ can be neglected), and so is our canonical result, as will be demonstrated in the following subsection. In most other cases the rules are merely approximate but, nevertheless, in quite good agreement with the canonical band edges: For the range of the s-band we find (-2.87, $\Gamma_1/4.96$, W_1) for the f.c.c. structure and (-2.87, $\Gamma_1/6.65$, H_1) for the b.c.c. structure. For the p-bands the range is (-6.69, $L_{2'}/8.80$, Γ_{15}) for the f.c.c. structure and (-6.33, $N_{1'}/8.80$, Γ_{15}) for the b.c.c. structure; here the value at the top is exact. Our f.c.c. d-band range is (-12.62, $X_3/12.39$, X_5 and $W_{1'}$), while the b.c.c. range is (-13.80, $H_{12}/14.16$, N_3).

5·2. *Bare canonical bands.* – For certain states the symmetry is so high that only *one* partial wave with $l < 3$ is allowed to contribute. In cubic crystals such states are, for instance, $\Gamma_1(s)$, $\Gamma_{15}(p)$, $\Gamma_{12}(d)$ and $\Gamma'_{25}(d)$. The remaining high-symmetry states of this kind in the f.c.c. and b.c.c. structures may be identified in fig. 10 and 11 as those where, for a given $\boldsymbol{k}$, the irreducible label occurs for only one set of l-bands. For these states the energy in the ASA is given exactly by the « unhybridized » expression (178) (and to second order by (177) or (176)) *regardless* of our choice of $\bar{Q}_s$, $\bar{Q}_p$ and $\bar{Q}_d$, *i.e.* regardless of the range of the orbitals chosen. Of course, for other states the energies obtained from a canonical band do depend on the $\bar{Q}$'s, and only the fully hybridized energies are representation independent.

We now make the traditional choice, $\bar{\mathbf{Q}} = \mathbf{0}$, so that we can use the simple analytical expression (46)-(47) for the canonical hopping integrals. The « unhybridized » bare l energy bands are given by

$$E^k_{li} = C_l + \Delta_l S^k_{li}(1 - Q_l S^k_{li})^{-1} = V_l + \Gamma_l(Q_l^{-1} - S^k_{li})^{-1} \tag{179}$$

or by

$$S^k_{li} = P_l(E) \approx \frac{E - C_l}{\Delta_l}\left(1 + Q_l \frac{E - C_l}{\Delta_l}\right)^{-1} = \frac{\Gamma_l}{V_l - E} + \frac{1}{Q_l}, \tag{180}$$

where, in addition to (177) and (178), we have used (85) and (105), which are more appropriate for free-electron–like bands. The bare canonical bands S_{li}^{k} are shown for the f.c.c. and h.c.p. structures in fig. 14 and 15. The b.c.c. bare canonical bands may be found in ref. [2]. From the analytical expressions for the hopping integrals the following properties of the bare canonical bands may be derived [6]:

Since S_{onsite} is zero, the centre of gravity of a bare canonical band, averaged over the Brillouin zone, is zero. The centre of gravity may be shown to vanish also for each individual $\boldsymbol{k}$-point, except for the s-band and for the p-bands at $\boldsymbol{k} = \mathbf{0}$.

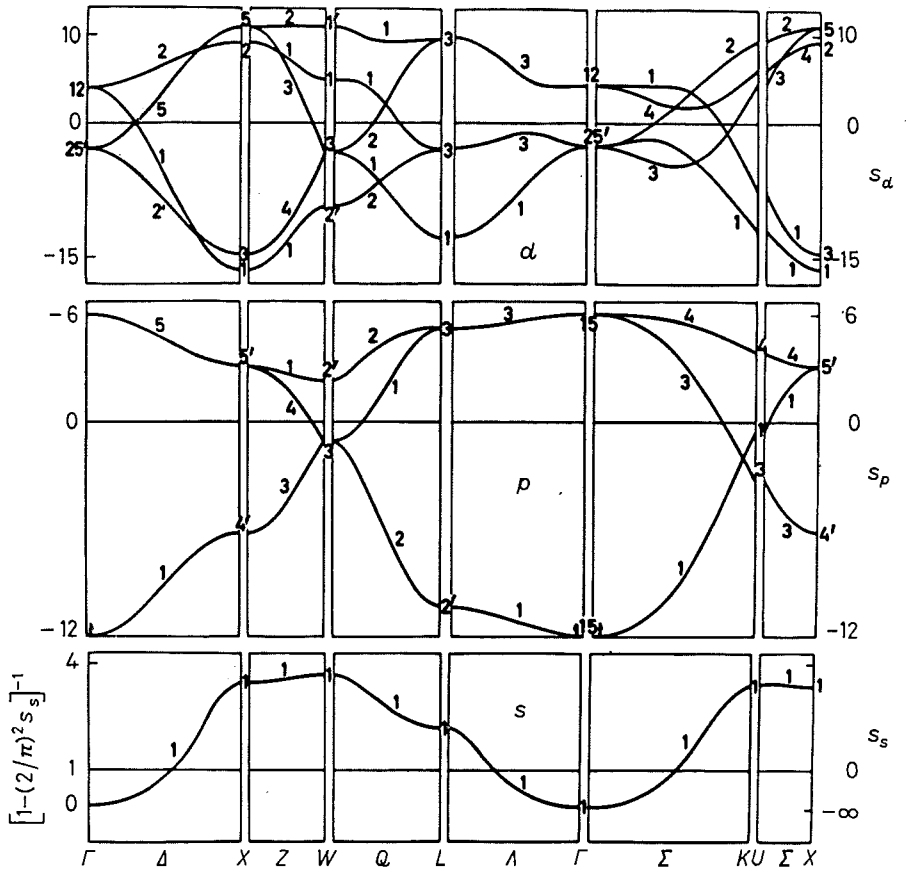

Fig. 14. – The bare canonical s-, p- and d-bands for the f.c.c. structure.

The width of a bare canonical band with $l \neq 0$ may conveniently be estimated from the following expression [6] for the second moment (see also eq. (47)):

$$(181) \qquad S_l^2 \equiv [(2l+1)]^{-1} \sum_i (\mathrm{BZV})^{-1} \int \mathrm{d}^3k (S_{li}^k)^2 =$$

$$= 4(2l+1) \frac{(4l)!}{[(2l)!]^2} \sum_{R \neq 0} \left(\frac{w}{d}\right)^{2(2l+1)} \approx \frac{2l+1}{\sqrt{2\pi l}} \sum_{R \neq 0} \left(\frac{2w}{d}\right)^{2(2l+1)} .$$

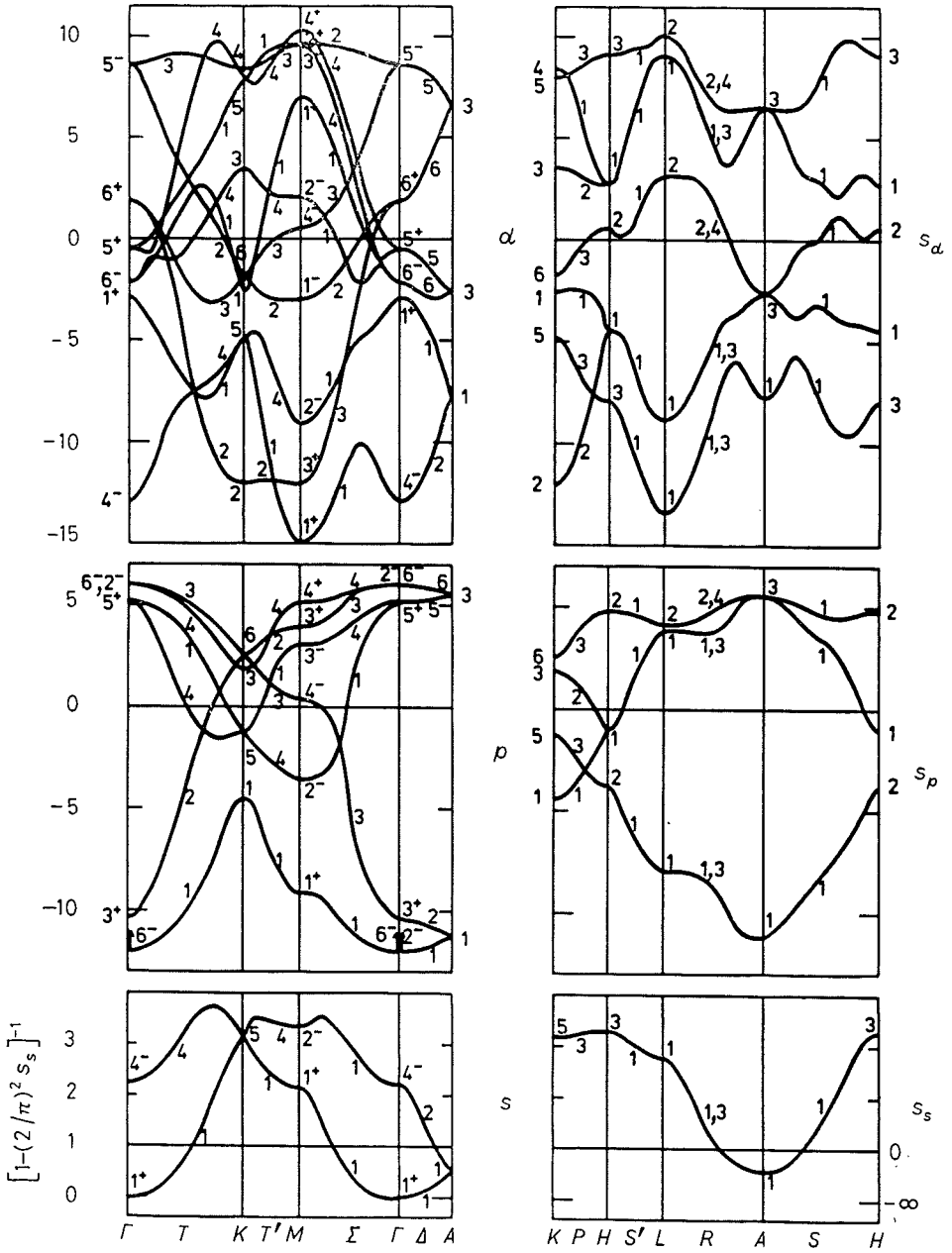

Fig. 15. – The bare canonical s-, p- and d-bands for the h.c.p. structure with $c/a = (8/3)^{\frac{1}{2}}$.

Here BZV is the Brillouin-zone volume which equals $(2\pi)^3$ times the inverse volume of the primitive cell. In the last approximation we have used Stirling's formula, which, for our purposes, is sufficiently accurate for all $l > 0$. The second moment (181) only depends on l plus the distances to and the numbers of atoms in the various shells. For the f.c.c. and b.c.c. structures these are given at the bottom of table II. Due to the high power $2(2l + 1)$ essentially only the first-nearest-neighbour shell contributes and, for closely packed structures, the ratio of the Wigner-Seitz radius to the nearest-neighbour distance

$2w/d_1$ varies between 1.10 and 1.14. If we assume that the density of states is rectangular on the P_l scale, the second moment yields the rough measure

$$[12S_l^2]^{\frac{1}{2}} \approx \left[\frac{12(2l+1)\cdot M_1}{\sqrt{2\pi l}}\right]^{\frac{1}{2}} \left(\frac{2w}{d_1}\right)^{2l+1} \tag{182}$$

of the bare canonical l-band width. Without the Stirling and nearest-neighbour approximations we obtain for the f.c.c., b.c.c. and h.c.p. ($c/a = (8/3)^{\frac{1}{2}}$) structures, respectively, 18.8, 18.7 and 18.6 for the bare canonical p-band widths and 23.8, 23.5 and 23.5 for the bare canonical d-band widths. Nearly the same results are obtained from (182). By comparison with the results in fig. 14 and 15 we realize that these estimates are quite accurate and they also compare well with the Wigner-Seitz results of 18 and 25 mentioned in the preceding subsection.

The bottom of the bare canonical s-band, which in cubic structures is the Γ_1-state, occurs at minus infinity due to the long range of $S_{ss\sigma}$ (46). This is in accord with the exact Wigner-Seitz rule mentioned in the previous subsection. (In order to avoid this divergence in fig. 14 and 15, we plotted $[1-(2/\pi)^2 S_s^k]^{-1}$ rather than S_s^k. This corresponds to using (179) with $V_s = 0$, $\Gamma_s = 1$ and $Q_s = (2/\pi)^2 \approx 0.40$, which is the free-electron value given in (76).) By Fourier transformation of the unscreened monopole field $S_{ss\sigma}$ we find that, for $\boldsymbol{k} \to \mathbf{0}$,

$$S_s^k \to -6(ks)^{-2} + \text{const} \quad \text{and} \quad E_s^k \to V_s + k^2/\tau_s\,. \tag{183}$$

The last result was obtained using (179) and (83). We have thus verified that the potential parameter V_s defined in (79) marks the bottom of the s-band and that τ_s defined in (83) is the s-band mass.

For the bare canonical p-band one subband, the «longitudinal acoustic branch», is discontinuous at the centre of the zone and it is only through hybridization with the s-band that the resulting energy band becomes continuous. By Fourier transformation of (46) we find that

$$S_{sp\sigma}^k \to -\sqrt{18}(ks)^{-1}\,, \quad S_{pp\sigma}^k \to -12 \quad \text{and} \quad S_{pp\pi}^k \to 6 \tag{184}$$

for small but nonzero values of $\boldsymbol{k}$ in the z-direction. The range $(-12/6)$ of the bare canonical p-band thus exactly follows the Wigner-Seitz rules. For the hybridization between the $ss\sigma$- and $pp\sigma$-bands near $k = 0$ the unbarred version of the tail cancellation condition (the KKR-ASA secular equation) yields

$$[P_s(E)(ks)^2/6 + 1][P_p(E) + 12] = 18\,. \tag{185}$$

We see that now the $pp\sigma$-like subband tends towards the value $18 - 12 = 6$

for $k \to 0$. This equals the common value of the two transverse and the longitudinal branches *at* $k = 0$ and, hence, the longitudinal branch of the energy band *is* continuous, regardless of the s-potential parameters. For the $ss\sigma$-like band (185) yields

$$E_s^k \to V_s + k^2 D_p(V_s)/\tau_s \approx V_s + k^2[\tau_s(1 - \tau_p(V_p - V_s)\, s^2/5)]^{-1} \quad \text{for } k \to 0\,, \tag{186}$$

if we use the parametrization (180) of the s-potential function, the relation (83) between Γ_s and the mass parameter τ_s and the definition (95) of the p-potential function. In the second equation we have parametrized the p-potential function too, and we have expanded to first order in $V_p - V_s$. By comparison with (183) we realize that the mass of the bottom of the sp-band deviates from τ_s unless the s and p square-well pseudopotentials coincide. Expression (186) is a well-known result originally derived by BARDEEN [57].

The shapes of the bare canonical d-bands are fairly similar to those of the canonical tight-binding d-bands, as may, for instance, be seen by comparison of fig. 10 and 14 for the f.c.c. structure. Moreover, Q_d in (179) as well as $Q_d - \bar{Q}_d$ in (177) are both relatively small, such that the P_d and the $\bar{P}_d$ scales are similar. The extent of the f.c.c. and h.c.p. bare canonical d-bands are, respectively, $(-16.40,\ X_1/10.94,\ W_1)$ and $(-15.01,\ M_{1^+}/10.36,\ M_{4^+})$ and, hence again, we

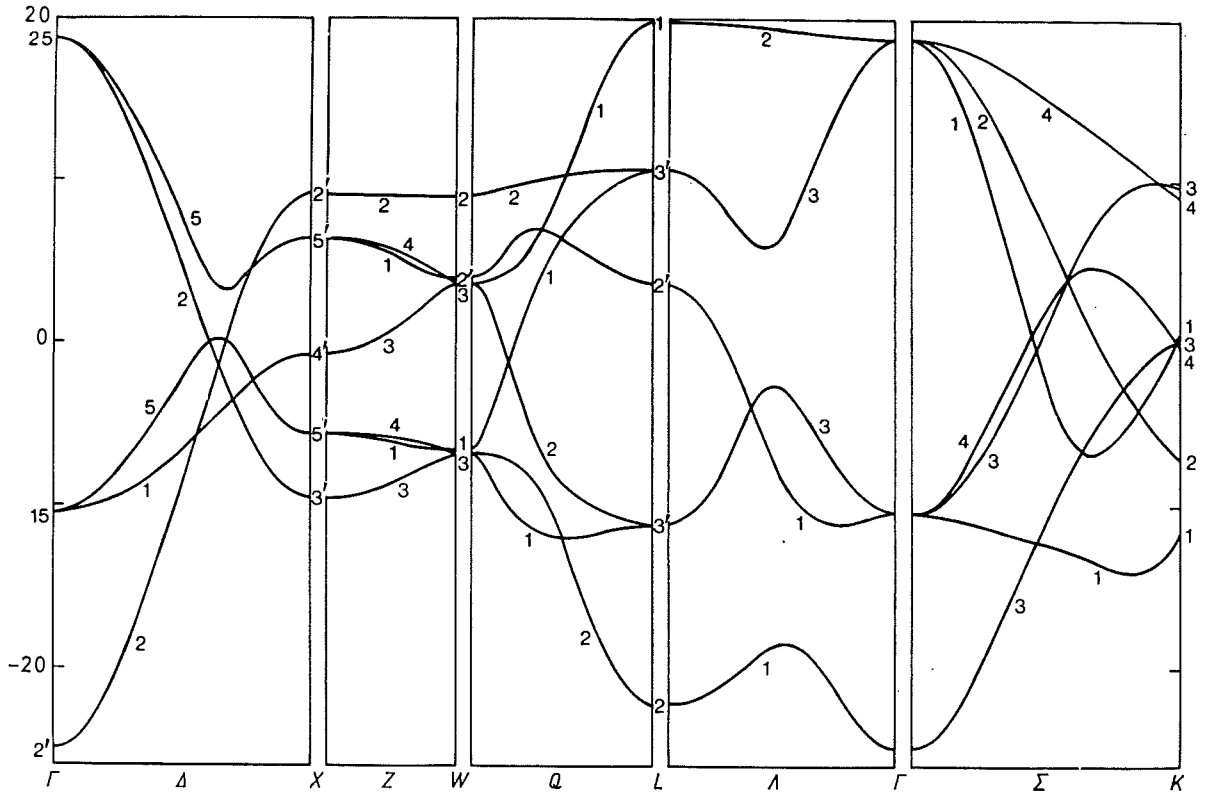

Fig. 16. – The bare canonical f-bands for the f.c.c. structure.

find a confirmation of the Wigner-Seitz result (— 15/10). The width of a transition metal d energy band is thus approximately

$$25\Delta_d = 25[\mu_d s^2]^{-1} \tag{187}$$

and the centre of gravity of an « unhybridized » d-band approximately falls at C_d.

Due to their simple analytical form, sufficient short range and good accuracy, the bare canonical d-hopping integrals (46) have been frequently used to describe transition metal d-bands [7-10, 58, 59]. For the same reasons the bare f-hopping integrals (47) are useful for describing the f-bands of the light actinides and cerium [10, 60-62]. In fig. 16 we show the f.c.c. bare canonical f-bands. These have low- and high-energy tails such that their range of approximately $(-25, \Gamma_{2'}/20, L_1)$ exceeds both the Wigner-Seitz range (— 18.67/14) and the band width 30.7 obtained from (182). The hybridization with the bare s-, p- and d-bands may be described in a convenient way using (47). For quantitative calculations of the *entire* band structure we, however, prefer using the tight-binding representation with the f-related hopping integrals derived from (130), (131) and (47).

5'3. *Potential parameters and trends.* – The relative band energies, the Fermi level and the band masses for the Rb series are shown in fig. 17. Since the Wigner-Seitz radii vary substantially, as seen in table V, the positions with respect to the bottom of the s-band have been multiplied by s^2, such that identical values of $(C_d - V_s)s^2$, etc. lead to identical band structures when plotted as functions of $\boldsymbol{ks}$. For free electrons the masses are unity, $V_s = V_p = V_f$ and $(C_d - V_s)s^2 = 20.2$, as mentioned in subsect. **4**'3.

Of the many trends apparent in fig. 17, the most significant is the development of the $4d$-band from being empty and free-electron–like to being an occupied core level: As the atomic number increases, the position of the $4d$-band decreases and its mass increases, because the added electron only partially screens the increased nuclear change. The added electrons essentially have $4d$ character as seen from the entry n_d in table V and the screening experienced by the less localized, *i.e.* smaller-mass, $5s$- and $5p$-electrons, is, therefore, rather complete, so that their potential parameters remain free-electron–like. The number of non-d-electrons is thus fairly constant equal to 1.5 ± 0.1 through the series and, apart from fluctuations due to structure in the densities of states, the position of the Fermi level is nearly constant, when scaled as in fig. 17.

The bottom of the $5s$-band falls well above the $4f$ pseudopotential V_f and well above the value of the one-electron potential at the sphere boundary (v in table V). Moreover, the $5s$ mass is significantly smaller than unity and attains a minimum, as do $(V_f - V_s)s^2$ and $(v - V_s)s^2$, near the middle of

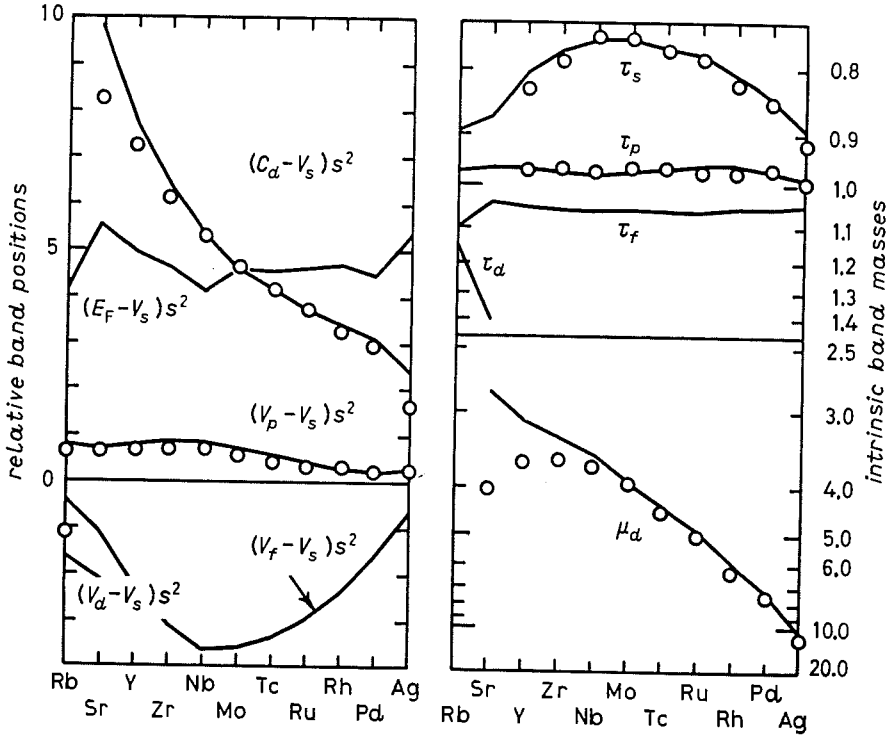

Fig. 17. – Band positions relative to the bottom of the s-band, in dimensionless units, and intrinsic band masses, on a reciprocal scale, in the $4d$ series. The full lines represent the results given in table III of self-consistent local-density LMTO-ASA calculations, while the open circles were obtained from the standard Mattheiss-Slater potential construction.

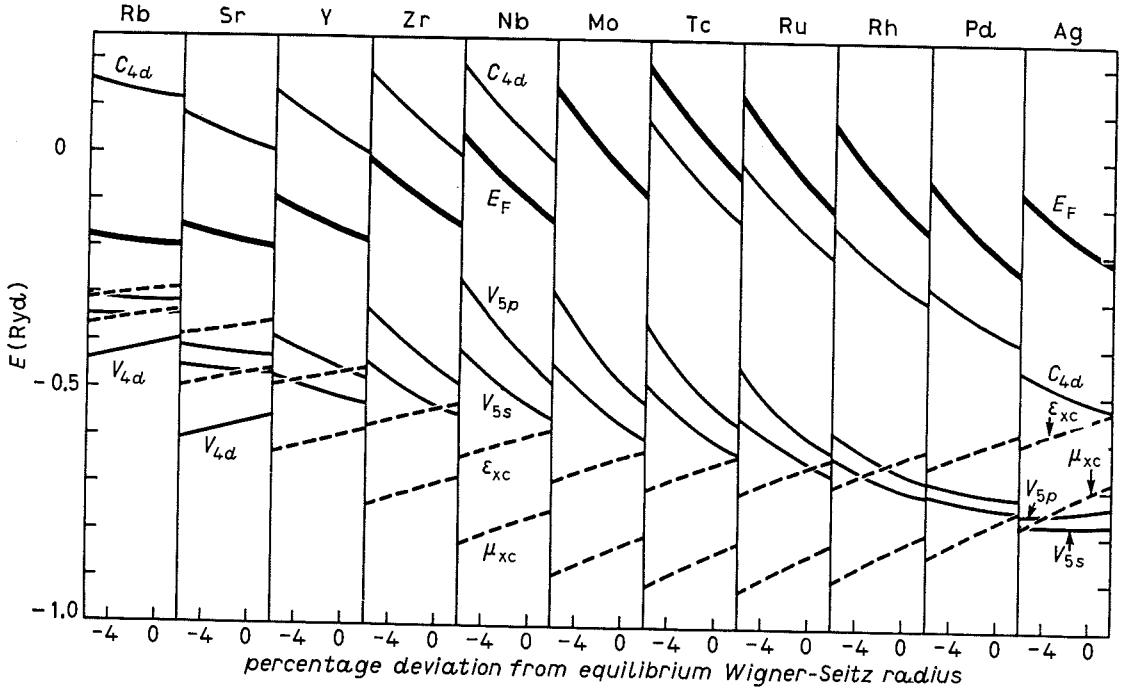

Fig. 18. – Self-consistent potential parameters for the $4d$ series as functions of the lattice constant.

TABLE VII. – *Volume derivatives of potential parameters.*

		K Rb Cs	Ca Sr Ba	Sc Y Lu	Ti Zr Hf	V Nb Ta	Cr Mo W	Mn Tc Re	Fe Ru Os	Co Rh Ir	Ni Pd Pt	Cu Ag Au
$\frac{dE_\nu}{d\ln s}$ (Ryd)	s	−0.14	−0.38	−0.85	−1.19	−1.39	−1.45	−1.08	−0.89	−0.85	−0.69	−0.44
		−0.15	−0.37	−0.86	−1.34	−1.74	−1.90	−1.82	−1.61	−1.18	−0.74	−0.25
		−0.06	−0.52	−0.82	−1.24	−1.59	−1.82	−1.82	−1.63	−1.26	−0.80	−0.33
	p	−0.19	−0.45	−0.89	−1.31	−1.52	−1.65	−1.35	−1.16	−1.37	−0.93	−0.82
		−0.18	−0.35	−0.88	−1.38	−1.78	−2.06	−2.06	−1.93	−1.55	−1.06	−0.71
		−0.08	−0.53	−0.83	−1.35	−1.76	−2.17	−2.21	−2.21	−2.00	−1.38	−1.01
	d	−0.22	−0.51	−0.91	−1.20	−1.36	−1.43	−1.28	−1.27	−0.85	−1.38	−1.04
		−0.22	−0.48	−0.82	−1.22	−1.52	−1.67	−1.76	−1.69	−1.47	−1.20	−0.85
		−0.12	−0.47	−0.88	−1.27	−1.56	−1.73	−1.88	−1.86	−1.60	−1.50	−1.14
	f	−0.02	−0.52	−0.98	−1.29	−1.42	−1.52	−1.34	−1.31	−1.54	−1.09	−0.71
		0.63	−0.18	−0.84	−1.29	−1.60	−1.84	−1.87	−1.85	−1.56	−1.16	−1.07
		−0.10	−0.49	−0.97	−1.38	−1.66	−2.01	−2.04	−2.18	−2.18	−1.61	−1.28
$\frac{d(C-E_\nu)}{d\ln s}$ (Ryd)	s	−0.15	−0.25	−0.48	−0.70	−0.89	−0.95	−0.85	−0.85	−0.77	−0.79	−0.58
		−0.11	−0.21	−0.42	−0.63	−0.84	−0.88	−0.89	−0.86	−0.78	−0.66	−0.54
		−0.13	−0.28	−0.34	−0.47	−0.62	−0.58	−0.60	−0.57	−0.47	−0.46	−0.39
	p	−0.82	−1.16	−1.92	−2.45	−2.90	−3.03	−2.70	−2.70	−2.20	−2.66	−2.13
		−0.83	−1.20	−2.03	−2.76	−3.45	−3.52	−3.45	−3.28	−2.93	−2.55	−1.94
		−0.88	−1.61	−2.24	−2.83	−3.46	−3.44	−3.43	−3.23	−2.73	−2.54	−1.96
	d	−0.34	−0.55	−0.77	−0.78	−0.72	−0.62	−0.43	−0.31	−0.23	−0.13	−0.06
		−0.28	−0.42	−0.73	−0.82	−0.86	−0.82	−0.64	−0.48	−0.30	−0.13	−0.02
		−0.23	−0.45	−0.79	−0.91	−0.98	−0.97	−0.79	−0.64	−0.43	−0.19	−0.04
	f	−2.32	−2.81	−3.78	−4.63	−5.46	−6.48	−6.14	−6.80	−6.25	−7.21	−7.26
		−2.43	−2.32	−2.85	−3.35	−3.83	−3.91	−3.99	−4.01	−4.08	−4.14	−3.76
		−1.08	−0.81	−3.88	−4.28	−4.68	−4.59	−4.60	−4.34	−3.86	−3.97	−3.65

$\frac{d \ln \Delta}{d \ln s}$	s	−2.9	−3.1	−2.9	−2.9	−2.8	−2.8	−2.9	−2.9	−2.9	−2.9	−2.9
		−3.0	−3.1	−3.0	−3.0	−2.9	−2.9	−2.9	−3.0	−3.0	−3.0	−3.1
		−3.1	−3.0	−3.2	−3.1	−3.1	−3.1	−3.2	−3.2	−3.2	−3.3	−3.4
	p	−2.6	−2.7	−2.8	−2.7	−2.7	−2.7	−2.7	−2.7	−2.7	−2.6	−2.6
		−2.6	−2.9	−3.0	−3.0	−3.1	−3.1	−2.9	−2.8	−2.8	−2.7	−2.7
		−2.9	−3.1	−3.0	−3.0	−3.1	−3.0	−3.0	−2.9	−2.8	−2.8	−2.8
	d	−1.1	−2.9	−4.3	−4.6	−4.5	−4.8	−4.7	−4.6	−4.7	−4.8	−4.9
		−1.4	−2.6	−3.7	−4.2	−4.5	−4.8	−4.8	−5.0	−5.0	−5.0	−5.5
		−1.9	−3.3	−3.6	−4.1	−4.3	−4.5	−4.8	−4.9	−4.9	−5.1	−5.5
	f	−2.6	−1.8	−1.8	−1.7	−1.8	−2.2	−1.7	−2.2	−1.7	−1.8	−1.8
		−2.7	−2.8	−2.7	−2.6	−2.5	−2.4	−2.3	−2.2	−2.0	−2.0	−1.9
		−1.8	−0.8	−3.2	−3.0	−2.8	−2.7	−2.6	−2.5	−2.4	−2.1	−2.1
$\frac{d[2(2l+1)Q]}{d \ln s}$	s	−0.11	−0.14	−0.12	−0.11	−0.11	−0.10	−0.10	−0.11	−0.10	−0.10	−0.11
		−0.12	−0.15	−0.13	−0.12	−0.12	−0.12	−0.11	−0.11	−0.11	−0.11	−0.12
		−0.12	−0.13	−0.15	−0.14	−0.14	−0.13	−0.13	−0.13	−0.13	−0.14	−0.15
	p	−0.13	−0.19	−0.27	−0.31	−0.31	−0.28	−0.20	−0.17	−0.14	−0.14	−0.11
		−0.18	−0.25	−0.41	−0.65	−0.64	−0.56	−0.45	−0.35	−0.25	−0.18	−0.12
		−0.27	−0.56	−0.35	−0.44	−0.54	−0.49	−0.43	−0.35	−0.26	−0.20	−0.14
	d	0.27	−0.07	−0.30	−0.30	−0.26	−0.22	−0.16	−0.10	−0.08	0.00	0.06
		0.22	−0.02	−0.27	−0.34	−0.37	−0.37	−0.34	−0.31	−0.23	−0.12	−0.02
		0.13	−0.17	−0.23	−0.32	−0.37	−0.40	−0.40	−0.38	−0.34	−0.24	−0.11
$\frac{d \ln p^{-\frac{1}{2}}}{d \ln s}$	s	−3.3	−3.6	−3.5	−3.4	−3.3	−3.3	−3.4	−3.4	−3.4	−2.8	−3.4
		−3.5	−3.8	−3.7	−3.5	−3.4	−3.3	−3.4	−3.4	−3.5	−3.5	−3.7
		−3.8	−3.7	−3.9	−3.6	−3.7	−3.7	−3.8	−3.7	−3.8	−3.8	−3.9
	d	−1.0	−2.7	−3.6	−3.7	−3.6	−3.6	−3.5	−3.6	−3.4	−3.3	−3.3
		−1.4	−2.6	−3.4	−3.7	−3.8	−3.9	−3.9	−3.9	−3.8	−3.8	−3.7
		−1.4	−3.1	−3.3	−3.7	−3.8	−4.0	−4.0	−4.0	−4.0	−3.9	−3.8

TABLE VIII. – *Volume derivatives of band parameters.*

		K Rb Cs	Ca Sr Ba	Sc Y Lu	Ti Zr Hf
$\frac{dn}{d\ln s}\left(\frac{\text{electrons}}{\text{atom}}\right)$	s	0.182	0.538	0.455	0.421
		0.117	0.628	0.688	0.651
		0.088	0.955	0.828	0.720
	p	−0.048	0.395	0.989	0.727
		−0.005	0.854	1.276	1.373
		0.169	0.905	1.494	1.613
	d	−0.144	−0.936	−1.377	−0.988
		−0.246	−1.532	−1.854	−1.720
		−0.427	−1.765	−2.206	−2.053
	f	0.011	0.003	−0.067	−0.161
		0.135	0.049	−0.112	−0.302
		0.000	−0.097	−0.119	−0.281
$\frac{d\ln q}{d\ln s}$		−0.7	−0.6	−0.5	−0.8
		−0.6	−0.5	−0.5	−0.6
		−0.7	−0.5	−0.6	−0.6
$\frac{dv}{d\ln s}$ (Ryd)		0.38	0.52	0.66	0.79
		0.35	0.47	0.61	0.73
		0.24	0.46	0.64	0.76
$\frac{dE_F}{d\ln s}$ (Ryd)		−0.27	−0.58	−1.07	−1.52
		−0.26	−0.62	−1.00	−1.60
		−0.13	−0.48	−1.12	−1.67
$\frac{d\,\text{r.m.s.}(E-E_\nu)}{d\ln s}$ (Ryd)	s	−0.084	−0.101	−0.071	−0.053
		−0.081	−0.081	−0.035	−0.043
		−0.060	−0.008	−0.089	−0.104
	p	−0.067	−0.089	−0.071	−0.081
		−0.063	−0.036	−0.032	−0.055
		−0.035	−0.005	−0.090	−0.133
	d	−0.072	−0.044	−0.053	−0.130
		−0.034	−0.040	−0.040	−0.154
		−0.007	−0.016	−0.060	−0.174

V Nb Ta	Cr Mo W	Mn Tc Re	Fe Ru Os	Co Rh Ir	Ni Pd Pt	Cu Ag Au
0.392	0.285	0.233	0.253	—0.074	0.240	0.191
0.615	0.365	0.247	0.136	0.038	—0.086	0.128
0.667	0.411	0.355	0.226	0.041	0.129	0.257
0.411	—0.029	—0.404	—0.469	—1.664	—0.504	—1.061
1.066	0.405	—0.036	—0.535	—0.934	—1.176	—1.490
1.272	0.429	0.026	—0.662	—1.542	—1.402	—1.923
—0.602	—0.032	0.406	0.535	1.831	0.590	1.042
—1.297	—0.255	0.345	1.031	1.535	1.816	1.790
—1.532	—0.385	0.221	1.153	2.255	2.094	2.324
—0.202	—0.222	—0.236	—0.321	—0.091	—0.327	—0.172
—0.381	—0.515	—0.555	—0.636	—0.634	—0.558	—0.423
—0.407	—0.455	—0.602	—0.718	—0.754	—0.821	—0.658
—1.0	—1.2	—1.4	—1.5	—1.8	—1.6	—1.8
—0.9	—1.2	—1.5	—1.8	—2.1	—2.4	—2.6
—0.8	—1.1	—1.4	—1.7	—2.2	—2.4	—2.7
0.93	1.03	1.04	1.10	1.16	1.08	1.09
0.89	1.03	1.10	1.21	1.24	1.20	1.12
0.93	1.06	1.12	1.25	1.31	1.28	1.25
—1.70	—2.04	—1.81	—1.87	—1.45	—1.98	—1.66
—2.01	—2.50	—2.64	—2.66	—2.52	—2.14	—1.55
—2.04	—2.62	—2.82	—2.98	—2.93	—2.77	—2.26
—0.064	—0.131	—0.166	—0.183	—0.192	—0.272	—0.382
—0.111	—0.265	—0.311	—0.368	—0.388	—0.387	—0.300
—0.160	—0.304	—0.362	—0.433	—0.439	—0.474	—0.420
—0.080	—0.152	—0.193	—0.203	—0.266	—0.245	—0.388
—0.099	—0.243	—0.320	—0.390	—0.426	—0.403	—0.286
—0.138	—0.272	—0.364	—0.451	—0.496	—0.508	—0.484
—0.162	—0.242	—0.298	—0.338	—0.354	—0.343	—0.452
—0.215	—0.352	—0.461	—0.519	—0.544	—0.524	—0.433
—0.225	—0.358	—0.501	—0.594	—0.670	—0.677	—0.613

the series. Since the mass (83) is essentially the ratio between the normalization integral in the sphere and the probability at the sphere boundary, this means that the 5*s*-electron is excluded from the core region (orthogonalization hole), and the above-mentioned facts may be explained as the effects of a repulsive ion core, whose size, relative to the atomic sphere, attains a maximum in the middle of the series. For a further discussion of this point and other trends in the 4*d* series we refer to a paper by PETTIFOR [58].

In fig. 18 we give the absolute band positions through the Rb series and as functions of the atomic volume. The numerical results may be found in tables III, V, VII and VIII. In fig. 18 and in tables III-VIII the zero of energy is the electrostatic (Hartree) potential between the atoms in an infinite crystal. This value is well defined in the ASA, where the charge density is spherical. At the sphere boundary of an elemental solid where the spheres are neutral, the electrostatic potential vanishes, and the one-electron potential, therefore, equals the exchange correlation potential which, in the local-density approximation, is $\mu_{xc}(n(s))$, *i.e.*

$$v \equiv v(s) = \mathrm{d}[n(s)\,\varepsilon_{xc}(n(s))]/\mathrm{d}n(s) \equiv \mu_{xc}(n(s)) \equiv \mu_{xc}\,, \tag{188a}$$

$$v \approx \mu_x(n(s)) = \frac{4}{3}\varepsilon_x(n(s)) = \frac{4}{3}\frac{-0.916}{r_s(n(s))} = \frac{-1.221}{s}q^{\frac{1}{3}}\,. \tag{188b}$$

For the approximation (188*b*) we have neglected correlation and used the well-known Hartree-Fock result for the homogeneous electron gas. The electron gas parameter r_s is the radius of a sphere holding one electron and, consequently, $qr_s(n(s))^3 = s^3$, where $q \equiv n(s)\,\mathcal{V}$ is the electron density at the sphere times the sphere volume, $\mathcal{V} \equiv \frac{4}{3}\pi s^3$. This «effective free-electron number» q is given in tables V and VI for the equilibrium atomic volume and its variation with volume is given in table VIII and is shown in fig. 19. The stippled lines in that figure are the constant-r_s curves given by $q = (s/r_s)^3$. The values of $v = \mu_{xc}$ and ε_{xc} at the sphere are shown in fig. 18.

The parabolic trend followed by the Fermi energy in fig. 18 results from the combined effects of filling-up the *d*-band and lowering its centre of gravity. The Fermi energy is the negative of the internal work function, and the difference between this and the external work function, which experimentally increases from about 0.23 Ryd in Y to about 0.40 Ryd in Pd, is due to the surface dipole.

Under the entry r.m.s. $(E - E_\nu)$ in tables V, VI and VIII we give the values of $[m_l^{(2)}/n_l]^{\frac{1}{2}}$, where $m_l^{(2)}$ is the second energy moment defined in (39).

The potential parameters indicated by open circles in fig. 17 result from the standard, non-self-consistent Matheiss-Slater potential construction which involves superposition of neutral-atom densities with the s^1-configuration in the 3*d* and 4*d* series and the s^2-configuration in the 5*d* series. For the transi-

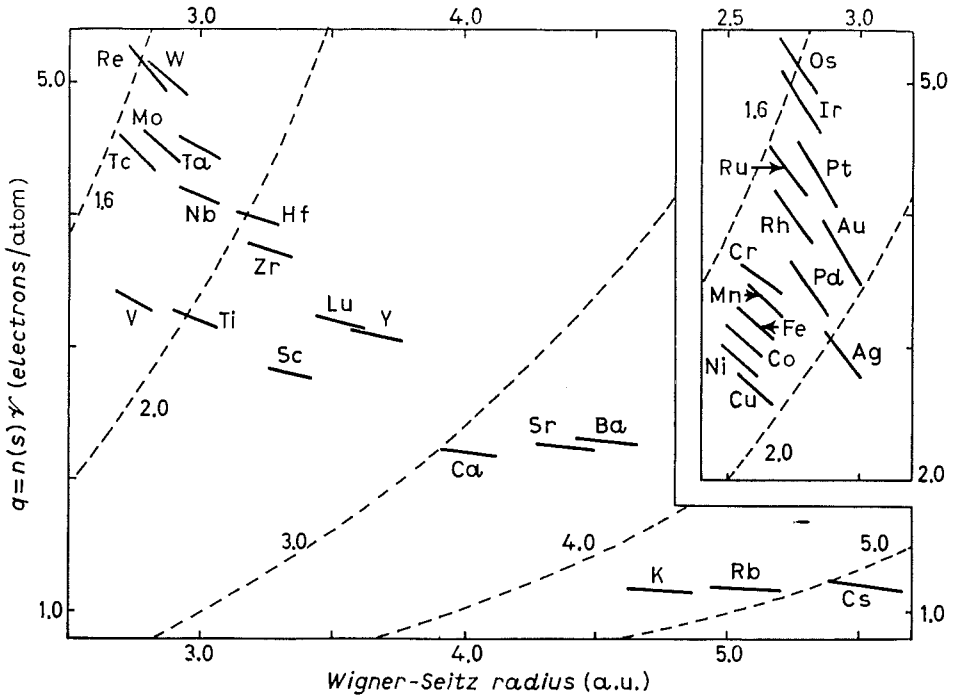

Fig. 19. – Electron density, $n(s)$, at the Wigner-Seitz radius, s, times the sphere volume $\mathscr{V} \equiv (4/3)\pi s^3$, that is, the effective free-electron number, $q \equiv n(s)\mathscr{V}$. The q-values were obtained from self-consistent calculations at three different atomic volumes for each metal. For the mono-, di- and tri-valent metals, at the beginning of the $3d$, $4d$ and $5d$ rows q is seen to be close to the respective values 1, 2 and 3. The stippled lines are the constant-r_s contours ($q = (s/r_s)^3$) corresponding to the r_s values 1.6, 2.0, 3.0, 4.0 and 5.0.

tion metals the band structures derived from the local density and the standard potentials differ by less than 20 mRyd, but for the simple, alkaline-earth and noble metals the differences are larger and here the local density potential generally yields the better Fermi surfaces [2].

Crude estimates of the potential parameters may be obtained directly from atomic energies and wave functions by renormalizing the latter to the atomic sphere and by using first-order perturbation theory.

The relativistic corrections to the band structures of metals have their origin in the regions close to the nuclei, where the velocity of the electrons is high, and they may, therefore, be separated into mass velocity plus Darwin shifts and the spin-orbit coupling. For a given metal the relativistic effects decrease with increasing angular momentum and principal quantum number and, for a given nl-shell, they increase with atomic number, approximately as Z^2. Due to the normalization (13) of the partial wave to the atomic sphere, the magnitudes of the relativistic effects are larger in the solid than in the atom by a factor of approximately $(1 - q_{nl})^{-1}$, where q_{nl} is the fraction of the *atomic* nl-electron which lies outside the sphere. For transition elements this fraction is about 0.5 for s-electrons and less than 0.1 for d-electrons. The par-

tial-wave normalization furthermore causes the magnitude of the relativistic effects in the solid to increase from the bottom to the top of the band and, for transition metal d-bands, this increase is nearly a factor of two.

Of the relativistic corrections, the shifts are the most important; the downwards shift of the $4s$-band with respect to the $3d$-band is about 15 mRyd in the middle of the $3d$ series, in the $4d$ series the corresponding number is 75 mRyd, and in the $5d$ series it is 250 mRyd. As a result, the number of non-d-electrons increases from 1.50 ± 0.10 per atom in the $4d$ series (Y to Ag) to 1.75 ± 0.15 in the $5d$ series (Lu to Au). In our self-consistent calculations the relativistic shifts have been taken into account by performing fully relativistic calculations, but leaving out the spin-orbit coupling effects on the band states, by deriving the potential parameters from a scalar radial Dirac equation [63]. As shown in fig. 20, the spin-orbit coupling parameters are typically one order of magnitude smaller than the relativistic shifts. More-

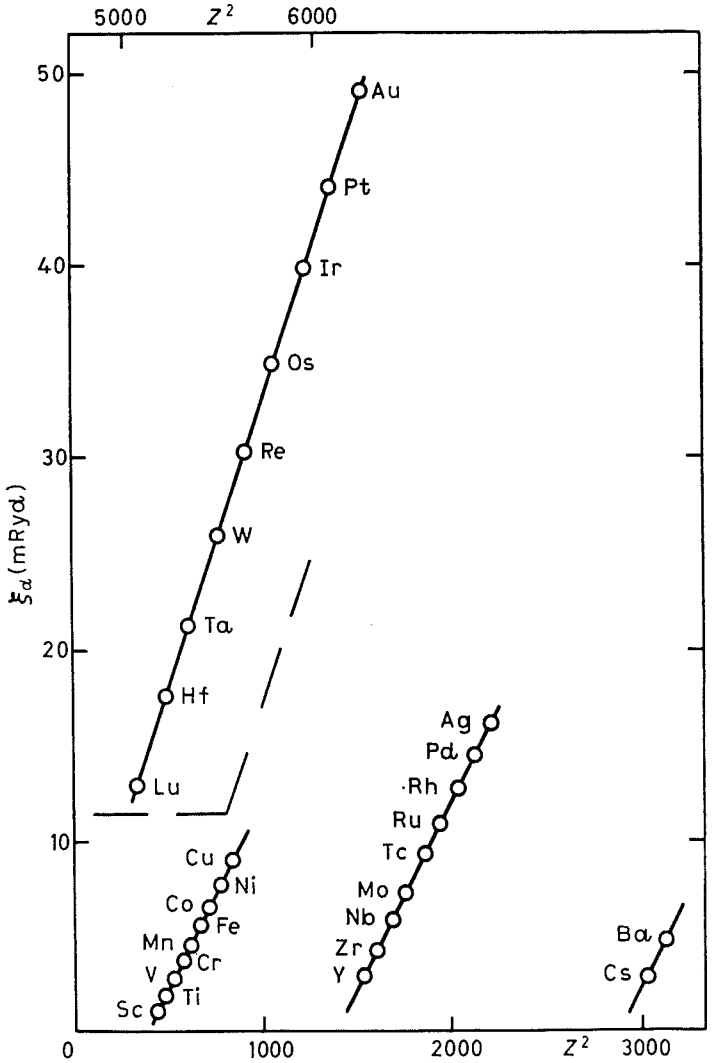

Fig. 20. – Spin-orbit coupling parameter $\xi_d(C_d)$ for the centre of the d-band, as a function of the square of the atomic number.

over, for crystals with inversion symmetry the spin-orbit coupling cannot split the two spin bands and, therefore, gives rise to splittings of first order in ξ only in small regions of $\boldsymbol{k}$-space near points of degeneracy.

Potential parameter tables for the rare-earth and actinide metals have been produced by SKRIVER [10].

6. – Ground-state properties of elemental metals.

6·1. *Cohesive properties.* – Recent interest has focussed on the calculation of the ground-state energy with the density-functional formalism using (41) or (43) and there has been a tendency to regard the resulting band structures as unphysical by-products. Not even in Hartree-Fock theory, where Koopman's theorem holds, does the sum of the band structure energies equal the total energy, because the former counts the electron-electron interactions twice. Nevertheless, many years of experience with *empirical* one-electron methods in solid-state physics and in chemistry indicate that often the simplest way to understand structural stability [64], elastic constants [65], phonon spectra [66], chemical reactions [67], etc., is through the behaviour of the sum of the one-electron energies plus an empirical short-range repulsion. It is now fairly simple, from the Born-Oppenheimer and the local-density-functional (LDF) approximations, to derive a so-called *force theorem* [2, 68, 69] which indicates that this practical experience might be firmly based. The force theorem has been used extensively [2, 9-11, 45, 53, 60, 61, 70-76] in first-principles calculations of the *pressure* [68] at zero temperature, that is the change of the total energy with uniform compression, *i.e.*

$$\mathscr{P}(\mathscr{V}) \equiv - \mathrm{d}E_{\mathrm{tot}}/\mathrm{d}\mathscr{V} , \tag{189}$$

where $\mathscr{V}$ is the volume and we have neglected the zero-point motion of the nuclei. Calculation of the pressure-volume relation enables one to estimate the equilibrium atomic volume, $\mathscr{V}_0$, as

$$\mathscr{P}(\mathscr{V}_0) = 0 , \tag{190}$$

the bulk modulus, or inverse compressibility, as

$$\mathscr{B} = - [\mathrm{d}\mathscr{P}/\mathrm{d} \ln \mathscr{V}]_{\mathscr{V}_0} \tag{191}$$

and, in principle, the cohesive energy as

$$E_{\mathrm{coh}} = - \int_{\mathscr{V}_0}^{\infty} \mathscr{P} \, \mathrm{d}\mathscr{V} = - \int_{s_0}^{\infty} 3 \mathscr{P} \mathscr{V} \, \mathrm{d} \ln s . \tag{192}$$

This is illustrated in fig. 21. Moreover, the force theorem has been used to calculate the heats of formation of alloys [77, 78] and, with appropriate modifications to include energy changes to second order, to the calculation of elastic constants [79].

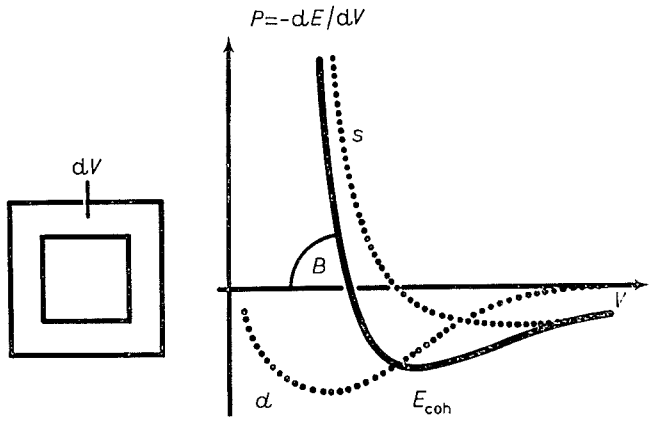

Fig. 21. – Total and partial pressure-volume curves (schematic). The bulk modulus is the slope of the curve, the equilibrium volume is the intersection with the volume axis and the cohesive energy is the area below the curve from the intersection to infinity.

The force theorem [2] states that the change of the total energy due to a deformation to first order equals the change in the sum of the one-electron energies for *rigidly shifted* cellular potentials plus the change of the electrostatic interaction between the *rigidly shifted* cellular (electronic plus nuclear) charge densities. In order to illustrate this theorem, we consider the calculation of the force acting on the nucleus at point $\boldsymbol{R}$: First we perform a self-consistent LDF calculation for the entire solid obtaining the one-electron energies E_j, the potential $V(\boldsymbol{r})$ and the electronic (plus nuclear) charge density $n(\boldsymbol{r})$. Then we choose some cell surrounding the nucleus at $\boldsymbol{R}$, but no other nuclei, and cut the potential $v_R(\boldsymbol{r}-\boldsymbol{R})$ and the charge density $n_R(\boldsymbol{r}-\boldsymbol{R})$ in that cell loose. With the virtually displaced potential $V(\boldsymbol{r}) - v_R(\boldsymbol{r}-\boldsymbol{R}) + v_R(\boldsymbol{r}-\boldsymbol{R}-\mathbf{d}\boldsymbol{R})$ we now solve the one-electron Schrödinger equation obtaining the new one-electron energies $E_j + \delta E_j$. If $\boldsymbol{r}$ lies in a gap region between the displaced cell and the undisturbed rest, the potential is given the value $V(\boldsymbol{r}) + \varepsilon_{xc}(n(\boldsymbol{r})) - \mu_{xc}(n(\boldsymbol{r}))$ and, if $\boldsymbol{r}$ lies in a region of overlap, the value is $V(\boldsymbol{r}) - \varepsilon_{xc}(n(\boldsymbol{r})) + \mu_{xc}(n(\boldsymbol{r}))$. When the new density $n(\boldsymbol{r}) + \delta n(\boldsymbol{r})$, obtained by solution of Schrödinger's equation with the displaced, non-self-consistent potential, is used as the trial density in the energy functional for the configuration with the virtually displaced nucleus, the change of the total energy $E_{tot} + \mathrm{d}E_{tot}$ can be evaluated explicitly and, as a result, we find the desired expression for the force

$$\boldsymbol{F} \equiv -\,\mathrm{d}E^{tot}/\mathbf{d}\boldsymbol{R} = -\sum_{j}^{occ} \delta E_j/\mathbf{d}\boldsymbol{R} + \boldsymbol{F}_{el} \tag{193}$$

with the electrostatic force given by

$$(194)\qquad -\boldsymbol{F}_{\mathrm{el}}\cdot\mathbf{d}\boldsymbol{R} \equiv$$
$$\equiv\int\!\!\int[n(\boldsymbol{r})-n_R(\boldsymbol{r}-\boldsymbol{R})]\,|\boldsymbol{r}-\boldsymbol{r}'|^{-1}\,[n_R(\boldsymbol{r}'-\boldsymbol{R}-\mathbf{d}\boldsymbol{R})-n_R(\boldsymbol{r}'-\boldsymbol{R})]\,\mathrm{d}^3r\,\mathrm{d}^3r'\,.$$

Note that it is merely the rigidly shifted density, rather than $n(\boldsymbol{r})+\delta n(\boldsymbol{r})$, which enters (194).

It is obvious that the force acting on the nucleus is independent of *where* we choose to cut that nucleus loose; the choice of cell just shifts the weight between the two terms on the right-hand side of (193). If, for instance, we choose the cell as an infinitesimal sphere around the nucleus, the first term vanishes and (193) reduces to the well-known Hellmann-Feyman theorem, which states that the force equals the electrostatic force acting on the nucleus. If, on the other hand, we choose the cell around the nucleus so large that its electronic charge neutralizes the nuclear charge and, furthermore, the cell is fairly compact, then the electrostatic field from the cellular charge $n_R(\boldsymbol{r}-\boldsymbol{R})$ is weak and of short range. Consequently, the change of the sum of the one-electron energies gives the dominant contribution to the force (193). The notation δE_j—rather than $\mathrm{d}E_j$—for the change of the band structure energy emphasizes that this change corresponds to the rigidly shifted, *non-self-consistent* potential. This undoing of self-consistency is what cancels the double counting.

The evaluation of the *pressure* from the force theorem is particularly simple with the LMTO method, because only the potential parameters change; the structure matrix is independent of the lattice constant. For the evaluation of the « deformation potentials » δE_j we first need the perturbation of the Hamiltonian. If we choose to work in the orthogonal representation and, for instance, use (65)-(66), we readily find that

$$(195)\qquad \delta\boldsymbol{H}^{(2)}=\delta\boldsymbol{C}+(\tfrac{1}{2}\,\delta\ln\boldsymbol{\Delta})\,\boldsymbol{\Delta}^{\frac{1}{2}}\,\tilde{\boldsymbol{S}}\boldsymbol{\Delta}^{\frac{1}{2}}+\boldsymbol{\Delta}^{\frac{1}{2}}\,\tilde{\boldsymbol{S}}\boldsymbol{\Delta}^{\frac{1}{2}}(\tfrac{1}{2}\,\delta\ln\boldsymbol{\Delta})+\boldsymbol{\Delta}^{\frac{1}{2}}\,\tilde{\boldsymbol{S}}\,\delta\boldsymbol{Q}\,\tilde{\boldsymbol{S}}\boldsymbol{\Delta}^{\frac{1}{2}}=$$
$$=\delta\boldsymbol{C}+(\tfrac{1}{2}\,\delta\ln\boldsymbol{\Delta})[\boldsymbol{H}^{(2)}-\boldsymbol{C}]+[\boldsymbol{H}^{(2)}-\boldsymbol{C}](\tfrac{1}{2}\,\delta\ln\boldsymbol{\Delta})+[\boldsymbol{H}^{(2)}-\boldsymbol{C}]\,\boldsymbol{\Delta}^{-1}\,\delta\boldsymbol{Q}[\boldsymbol{H}^{(2)}-\boldsymbol{C}]\,.$$

Here the only matrices which are not diagonal in Rlm are $\tilde{\boldsymbol{S}}$ and $\boldsymbol{H}^{(2)}$. If we now assume that $\boldsymbol{H}^{(2)}$ has been diagonalized as in (31), first-order perturbation theory simply yields

$$(196)\qquad \delta E_j^{(2)}=\boldsymbol{u}_j^{+}\,\delta\boldsymbol{H}^{(2)}\,\boldsymbol{u}_j=$$
$$=\sum_l[\delta C_l+(E_j^{(2)}-C_l)\,\delta\ln\Delta_l+(E_j^{(2)}-C_l)^2\,\Delta_l^{-1}\,\delta Q_l]\sum_{Rm}|u_{Rlm,j}|^2=$$
$$=\sum_l\delta E_l\big(P(E_j)\big)^{(2)}\sum_{Rm}|u_{Rlm,j}|^2\,,$$

where $E_l(P)^{(2)}$ was given in (103). It is now possible to include the change of the small potential parameter p, as well as the combined-correction term, but this is seldom necessary. Here, we shall just go to second order and use the ASA, whereby, for an elemental solid, also the electrostatic term in the force relation (193) vanishes. With these approximations the pressure is given by the following equivalent expressions:

$$(197a) \qquad 3\mathscr{P}\mathscr{V} \equiv -\mathrm{d}E_{\mathrm{tot}}/\mathrm{d}\ln s = -\sum_j^{\mathrm{occ}} \delta E_j/\delta \ln s =$$

$$= -\sum_l n_l \left[\frac{\delta C_l}{\delta \ln s} + \langle E - C\rangle_l \frac{\delta \ln \Delta_l}{\delta \ln s} + \langle (E-C)^2\rangle_l \frac{1}{\Delta_l}\frac{\delta Q_l}{\delta \ln s}\right],$$

$$(197b) \qquad 3\mathscr{P}\mathscr{V} = -\sum_l n_l \left[\frac{\delta V_l}{\delta \ln s} + \langle E - V\rangle_l \frac{\delta \ln \Gamma_l}{\delta \ln s} + \langle (E-V)^2\rangle_l \frac{1}{\Gamma_l Q_l^2}\frac{\delta Q_l}{\delta \ln s}\right],$$

$$(197c) \qquad 3\mathscr{P}\mathscr{V} = -\sum_l \int^{E_F} [\delta E_l(P_l(E))/\delta \ln s] N_l(E)\,\mathrm{d}E \equiv \sum_l 3\mathscr{P}_l\mathscr{V}\,;$$

$\mathscr{V} = \frac{4}{3}\pi s^3$ is the atomic volume. Like in subsect. **3**'4, we have projected the density of states onto the orthogonal orbitals or, equivalently, onto the partial waves and the pressure has been decomposed in the same way. Moreover, the energy moments are

$$(198) \qquad \langle E - C\rangle_l \equiv (m_l^{(1)}/n_l) - (C_l - E_{\nu l}) = -(C_l - E_{\nu l})$$

and

$$(199) \qquad \langle (E-C)^2\rangle_l \equiv (m_l^{(2)}/n_l) - 2(m_l^{(1)}/n_l)(C_l - E_{\nu l}) + (C_l - E_{\nu l})^2 =$$

$$= [\mathrm{r.m.s.}(E - E_\nu)_l]^2 + (C_l - E_{\nu l})^2\,,$$

where, like in our tables, we have chosen $E_{\nu l}$ to be at the centre of gravity of the occupied part of the band. For the transition metal d-bands we prefer using the « central » parameters C and Δ, while for the s- and p-bands we prefer using the « pseudopotential » parameters V and Γ. The corresponding equation (197b), which is equivalent to (197a), was obtained from expression (85).

So far eq. (196) is valid for any first-order perturbation of the atomic-sphere potential. Now we derive expressions for the change of the potential parameters using the fact that, for evaluating the pressure, the potential should be frozen and only the sphere radius should be changed. The (unnormalized) radial wave function as given by the radial Schrödinger equation

$$(200) \qquad -[r\bar{\varphi}_l(E, r)]'' = [E - v(r) - l(l+1)r^{-2}] r\bar{\varphi}_l(E, r) \equiv [E - v_l(r)] r\bar{\varphi}_l(E, r)$$

is, therefore, unchanged and only the radius, s, at which the boundary condition D_l, or equivalently P_l, is installed varies (see fig. 8, eqs. (70), (95) and (100)). This is illustrated in fig. 22. Since $(r\bar{\varphi})''r/\bar{\varphi} = D(D+1) + rD'$, with $D \equiv r\bar{\varphi}'/\bar{\varphi}$, the radial Schrödinger equation is easily rewritten as a first-order differential equation for the s-dependence of the logarithmic derivative function, $D_l(E, s)$, and hence, for the inverse function, the energy $E_l(D_l, s)$ corresponding to the boundary condition D_l at the radius s. The result is

$$(201) \quad -\partial E_l(D_l, s)/\partial \ln s = [\partial D_l(E, s)/\partial \ln s][\partial D_l(E, s)/\partial E]^{-1} = \\ = [(D_l + l + 1)(D_l - l) + (E - v)s^2]s\varphi_l(E, s)^2 = \\ = [D_l(D_l + 1) + (E - v_l)s^2]s\varphi_l(E, s)^2 .$$

The fact that

$$(202) \quad \dot{D}_l(E) = -[s\varphi_l(E, s)^2]^{-1}$$

follows from

$$(203) \quad 0 = \langle\varphi(E)|-\nabla^2 + v(r) - E_\nu|\varphi\rangle = (E - E_\nu)\langle\varphi(E)|\varphi\rangle + W\{\varphi, \varphi(E)\}$$

by letting $E_\nu \to E$. In (201) v is the value of the potential at the sphere and $v_l \equiv v + l(l+1)s^{-2}$ is the corresponding value of the potential including the centrifugal term which enters the effective one-dimensional Schrödinger equation (200). When calculating the pressure, we must substitute v (188) by $\varepsilon_{xc}(n(s)) \equiv \varepsilon_{xc}$ due to the exchange correlation correction mentioned above, or add this exchange correlation correction as a separate term which is given by (204) below. Expression (201) for the « frozen » deformation potential is exact, to all orders in $E - E_\nu$, and it may be inserted directly for $-\delta E_l(P_l(E))/\delta \ln s$ in (196) or (197c), although the expansions in powers of $E - C_l$, $E - V_l$ or $E - E_\nu$, to which we shall return in a moment, are more convenient.

From (201) we realize that the various characteristic energies V, B, C and A, which correspond to the respective logarithmic derivative values $D = l$, 0, $-l-1$ and $-\infty$, have quite different deformation potentials: The contribution to the pressure from a pure state with energy, B, at the bottom of the band is positive (repulsive) if the electron is allowed classically to pass out of the atomic sphere ($B_l > v_l$), and it is negative (attractive) if the electron escapes the sphere only by tunnelling ($B_l < v_l$). The magnitude of the pressure is proportional to $\varphi(E, s)^2$, *i.e.* to the probability of being *at* the sphere. The contribution to the pressure from a pure state with energy, A, at the top of a band is always repulsive. These different behaviours are illustrated in fig. 22. At the bonding energy the radial wave function attains a maximum between the atoms, if the region is classically allowed, and a minimum, if it is forbidden (see eq. (200)). For a compression from s to $s - \delta s$ this energy

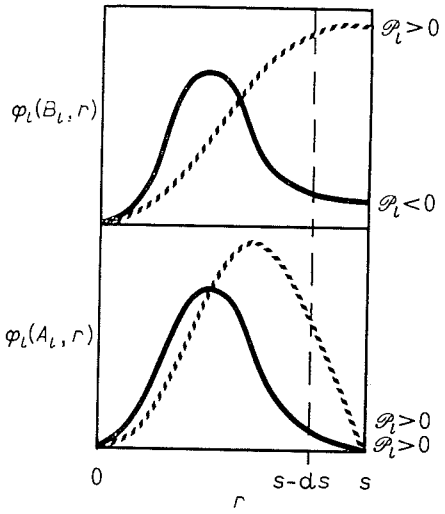

Fig. 22. – Radial wave functions, φ_l, at the bottom (B_l) and the top (A_l) of the band. The dotted lines are for cases where B_l and A_l are greater than the effective potential, v_l, at the sphere, and the full lines are for cases where B_l and A_l are smaller than v_l: The sign of the partial pressure is indicated to the right.

now corresponds to a positive slope of the wave function for a « free » state and to a negative slope for a tunnelling state. Since for a given atomic volume the slope (or rather φ'/φ) is a decreasing function of energy (202), it is necessary, in order to restore the bonding condition, $\varphi'=0$, to raise the energy of the « free » state and to lower the energy of the tunnelling state. The pressure thus raises the energy of a « free » electron and lowers the energy of a tunnelling electron at the bottom of the band. That the pressure always raises the energy of an electron at the top of the band can be realized from fig. 22, too.

An elemental metal is, therefore, kept together by the tunnelling electrons in the lower (bonding) parts of (narrow) *d*- or *f*-bands *and* the exchange plus correlation which contributes the attraction

$$(204a)\qquad 3\mathscr{P}_{xc}\mathscr{V}=-\sum_l\int^{E_F}(\varepsilon_{xc}-\mu_{xc})\,s^3\varphi_l(E,s)^2N_l(E)\,\mathrm{d}E=$$

$$=-3n(s)\mathscr{V}[\varepsilon_{xc}(n(s))-\mu_{xc}(n(s))]=-3q(\varepsilon_{xc}-\mu_{xc})\approx$$

$$(204b)\qquad 3\mathscr{P}_x\mathscr{V}=q\varepsilon_x=-0.916\,q/r_s(s)=-0.916\,q^{\frac{4}{3}}/s\,.$$

For approximation (204*b*) we have neglected correlation like in (188*b*). In free-electron–like metals the exchange correlation pressure (204*a*) is the only attractive one, unless a partial square-well pseudopotential, V_l, falls below $v(s)$.

This description of binding seems to differ from the « chemical » one, where, essentially, the states in the lower half of any band are said to be bonding, while those in the upper half are antibonding. The connection to the chemical

description is given by (197*a*), where the pressure is separated into a movement of the centre of the band, the band broadening and the change of the band shape which may often be neglected. Now, in the chemical description the movement of the band centre is not included but, instead, an empirical short-range repulsion is added to the contribution from the sum of the one-electron energies calculated *with fixed* C's.

In order to obtain explicit expressions for the change of C or V, of the band broadening and the shape, we may, for instance, expand the energy dependence of (201) to second order in $E - E_\nu$ using the third-order expansion (104) for $E(P(D))$ with $P(D)$ given by (95), perform the integral over energy and then express the $E - E_\nu$ moments in terms of the $E - C$ or $E - V$ moments as in (198)-(199). This yields fairly complicated expressions for the volume dependence of the position, width and shape parameters C, Δ and Q, or V, Γ and Q. The numerical results given in the present lecture were in fact obtained with a third-order expansion of (201) [10]. An alternative and equivalent procedure is, from the normalized and orthogonal phi–phi-dot pair for the sphere radius s, to construct a normalized and orthogonal pair for radius $s - \delta s$ and then use the latter in definitions (64), (67), (68), (79) and (81) of the potential parameters. We now quote the results correct to first order in $E - E_\nu$:

For the change of the band positions (201) yields

$$(205) \qquad -\frac{\delta C}{\delta \ln s} = 2\,\frac{C-v}{\mu} \quad \text{and} \quad -\frac{\delta V}{\delta \ln s} = (2l+3)\,\frac{V-v}{\tau}\,.$$

If the exchange correlation pressure (204) is not added separately, v should be substituted by $v + \varepsilon_{xc} - \mu_{xc}$ ($= \varepsilon_{xc}$ for an elemental solid). For free electrons, where $V = v$ and $\tau = \mu = 1$, these equations reduce to $\delta V = 0$ and $\delta(C - v)s^2 = 0$, as they should. Usually C lies above v, so that the centre of the band moves up under compression. This movement is inversely proportional with the band mass.

For the volume dependence of the width and mass parameters the first-order results are

$$(206a) \qquad -\frac{\delta \ln \Delta}{\delta \ln s} = \frac{\delta \ln \mu s^2}{\delta \ln s} = (2l+1) + \frac{2}{\mu} - \frac{2(C-v)s^2}{D\{\dot\varphi\} + l + 1}$$

and

$$(206b) \qquad -\frac{\delta \ln \Gamma}{\delta \ln s} = \frac{\delta \ln \tau s^2}{\delta \ln s} = -(2l+1) + \frac{2l+3}{\tau} - \frac{2(V-v)s^2}{D\{\dot\varphi\} - l}\,.$$

For free electrons $\tau = 1$ and $V = v$, so that (206*b*) yields the well-known result that the band width scales as s^{-2}, *i.e.* like a kinetic energy with a volume-independent mass, τ. Moreover, for free electrons with $E_\nu = C$, it may be proved

that $2(C-v)s^2[D\{\dot{\varphi}\}+l+1]^{-1}=2l+1$ (see (72) and (76)) so that $\delta\ln\Delta/\delta\ln s=-2$, which is the same result as obtained for $\delta\ln\Gamma/\delta\ln s$. For transition metal d-bands $Q\approx 0$, so that $D\{\dot{\varphi}\}+l+1\approx 5$. Furthermore, fig. 17 shows that $(C-v)s^2$ decreases from about 7 to 2 and that μ increases from about 3 to 12 as we proceed through the $4d$ series. The result is, therefore, that $\delta\ln\Delta/\delta\ln s$ decreases from about -3 to about -5.

The band shape depends on volume like

$$(207a)\qquad \frac{\delta Q}{\delta\ln s}=\frac{1}{2}\frac{D\{\dot{\varphi}\}-l-4/\mu}{D\{\dot{\varphi}\}+l+1}+\left[\frac{1}{(D\{\dot{\varphi}\}+l+1)^2}-\frac{12p}{(\mu s^2)^2}\right]\frac{(C-v)s^2}{\mu}$$

when $E_\nu\approx C$ and like

$$(207b)\qquad \frac{\delta Q}{\delta\ln s}=\frac{\tau}{(2l+3)\mu}\frac{D\{\dot{\varphi}\}+l+1-2(2l+3)/\tau}{D\{\dot{\varphi}\}-l}+$$
$$+\left[\frac{1}{(D\{\dot{\varphi}\}-l)^2}-\frac{6(2l+3)p}{(\tau s^2)^2}\right]\frac{(V-v)s^2}{\mu}$$

when $E_\nu\approx V$. When we are not considering an elemental solid, both expressions should contain the prefactor $(s/w)^{2l+1}$. For free electrons Q is a fixed number, given by (75) and (76) and thus independent of volume. This is, of course, consistent with (207) as seen by using the free-electron values (75), (76) and (78). The second-moment term of the pressure (197) thus vanishes for free-electron bands. For transition metal d-bands $Q\approx 0$, so that $D\{\dot{\varphi}\}\approx 2$, and $p^{-\frac{1}{2}}$ is of the order of $50(\mu s^2)^{-1}$. This means that the term proportional to p is rather small and consequently $\delta Q/\delta\ln s\approx[-10+(C-v)s^2]/25\mu$, which in (197$a$) gives rise to a small repulsive pressure.

The s, p, d and f partial pressures for the $4d$ and $5d$ series are shown in fig. 23 as functions of $(s-s_0)/s_0$, where s_0 is the experimentally observed equilibrium radius. In this picture the exchange correlation term (204) has been included in each partial pressure, moreover, the small f-pressure arises because we explicitly included f-orbitals in the calculations rather than folding them down into the tails of the s-, p- and d-orbitals with the procedure described in subsect. 4·12. As mentioned above, we could also have separated the repulsion from the centre-of-band movement from the band-broadening contribution, we could have shown the energy distribution of the partial pressures and we could even have projected onto the nonorthogonal short-range orbitals instead of onto the orthogonal ones and hence have obtained a non-diagonal description more similar to the descriptions of bonding used by the chemists in terms of overlap populations. The radius at which the total pressure, which is independent of these choices of representation, vanishes is denoted by th and is seen to be generally a few per cent too small. Using the band parameters shown in fig. 17-19, or in tables III, IV for the experimental

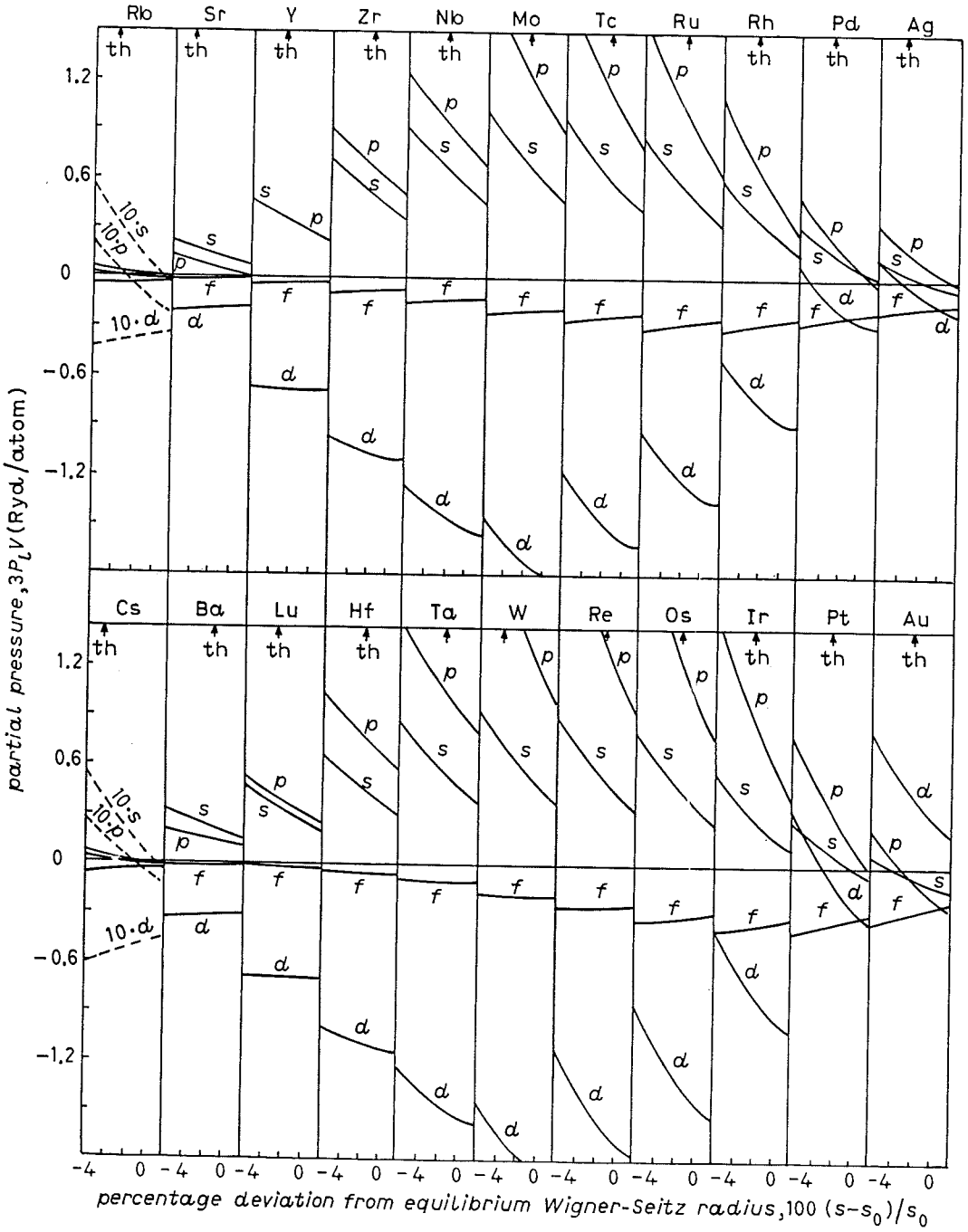

Fig. 23. – Partial pressures calculated for the Rb and Cs series as functions of $(s - s_0)/s_0$, where s_0 is the experimentally observed equilibrium radius. th indicates the calculated equilibrium Wigner-Seitz radius.

radius, together with (197), (205) and (206), we shall now discuss the balance between the partial contributions to the pressure shown in fig. 23.

For a homogeneous electron gas in a homogeneous positive background (whose kinetic energy is neglected), *i.e.* for nonrigid jellium, $V = \mu_{xc} < \varepsilon_{xc}$ and $\tau = 1$ for all values of l and s. The δV term in (197*b*), therefore, provides

an attractive, *i.e.* negative, pressure which is the exchange correlation correction (204) to the second, band-broadening term

$$(208) \qquad 3\mathscr{P}_{\mathrm{kin}}\mathscr{V} = -n\langle E - V\rangle(-2) = -q\tfrac{3}{5}k_{\mathrm{F}}^2(-2) = -q(2.21\, r_s^{-2})(-2)\,.$$

The latter is the usual kinetic-energy term. The equilibrium for the jellium occurs at $r_s \equiv sq^{-\frac{1}{3}} = 2\times 2.21/0.916 = 4.83$ a.u., if correlation is neglected, and at $r_s \approx 4.1$, when it is included. Crudely speaking, this is the situation found in the simple metals (see, for instance, fig. 19). As we proceed into a transition series, where the number of s- and p-electrons is about 1.6, the atomic volumes decrease (see fig. 24) due to increased d-electron binding, as will be explained below. The relative core size thereby increases with the result that

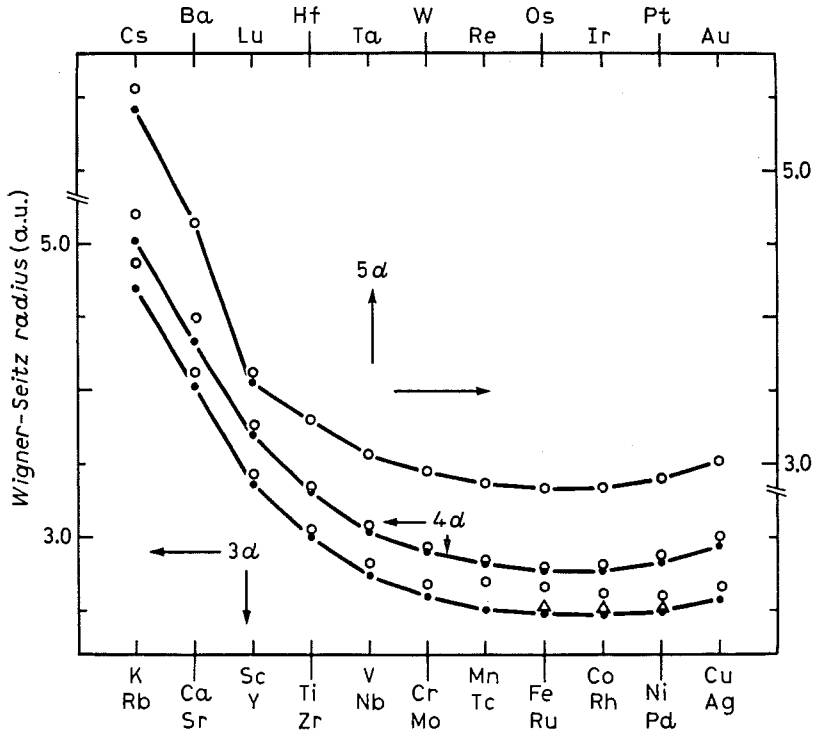

Fig. 24. – Equilibrium Wigner-Seitz radii for the 3d, 4d and 5d series. The line and full dots are the results of non-spin-polarized calculations, while the open triangles for Fe, Co and Ni are for spin-polarized calculations. The open dots are the experimental values.

the s and p pseudopotentials, V, increase and reach maxima well above $\varepsilon_{\mathrm{xc}}$ near the middle of the series, and that τ_s decreases to a minimum of about 0.7. The s and p pressures contributed by the δV term, therefore, change sign and reach positive maxima near the middle of the series. Also the positive, kinetic s and p contributions to $3\mathscr{P}\mathscr{V}$, arising from the band-broadening term, increase with decreasing s. The s^{-2} behaviour (208) found for free elec-

trons is, however, somewhat modified, due to the presence of the hybridization gap in the s-band created by the d-bands.

Turning now to the d-electrons, we realize that C_d lies above ε_{xc} and, therefore, increases with pressure. This means that the δC term in (197a) is repulsive, as are the s and p terms, and it reaches a maximum near the middle of the series due to the combined behaviour of $C_d - \varepsilon_{xc}$, μ_d and n_d. The attraction is provided by the band-broadening term and, for a rectangular density of d-states, $\langle E - C\rangle_d \approx -25\Delta_d\,(10 - n_d)/20$ and $\delta \ln \Delta_d/\delta \ln s \approx -5$, as obtained from (206$a$). Therefore, the d-band broadening gives rise to the well-known parabolic behaviour [80]

$$3\mathscr{P}_{d\text{-bond}}\mathscr{V} \approx (25\Delta_d) n_d(10 - n_d)/4\,, \tag{209}$$

which is about 30 per cent reduced by the δC term.

In order to obtain the bulk modulus or the cohesive energy from the pressure relation (eqs. (190)-(193) and fig. 21), the band parameters must be determined self-consistently as functions of atomic volume. Although the change of radius at which the boundary condition is installed as well as the electron-electron interaction cause the band energies to rise rapidly with compression, we have seen that it is only the former which enters the pressure relation. For the d-electrons this change is at least one order of magnitude smaller than the total self-consistent change given in table VII, and we have argued that its magnitude is only about one-third of the attractive contribution from the broadening of the d-band. For d-electrons the effect of electron-electron interaction is nearly the same throughout the band and this means that

$$\mathrm{d} \ln \Delta_d/\mathrm{d} \ln s \approx \delta \ln \Delta_d/\delta \ln s\,. \tag{210}$$

In Pd, for instance, the values in (210) are, respectively, -5.0 and -4.5. The d contribution to the cohesive energy is, therefore, roughly minus the sum of the one-electron energies measured relative to C_d. The sum of the s and p pressures becomes negative for $s \gtrsim 4$, as we have seen, and their integral from s_0 to infinity turns out to be rather small. The major contribution to the cohesive energy in the transition metals thus arises from the broadening of the d-band as argued originally by WIGNER and SEITZ [81] and used extensively by FRIEDEL [80] and co-workers. The bulk modulus is, however, except at the end of a series, contributed mainly by the highly compressed s- and p-electrons, as seen in fig. 23. This short-range repulsion is not included in the simple extended Hückel [82], chemical pseudopotential [83] and empirical tight-binding [80] schemes.

Our LMTO-ASA results for the equilibrium Wigner-Seitz radii and bulk moduli are summarized in fig. 24 and 25. In fig. 24 the line and the full

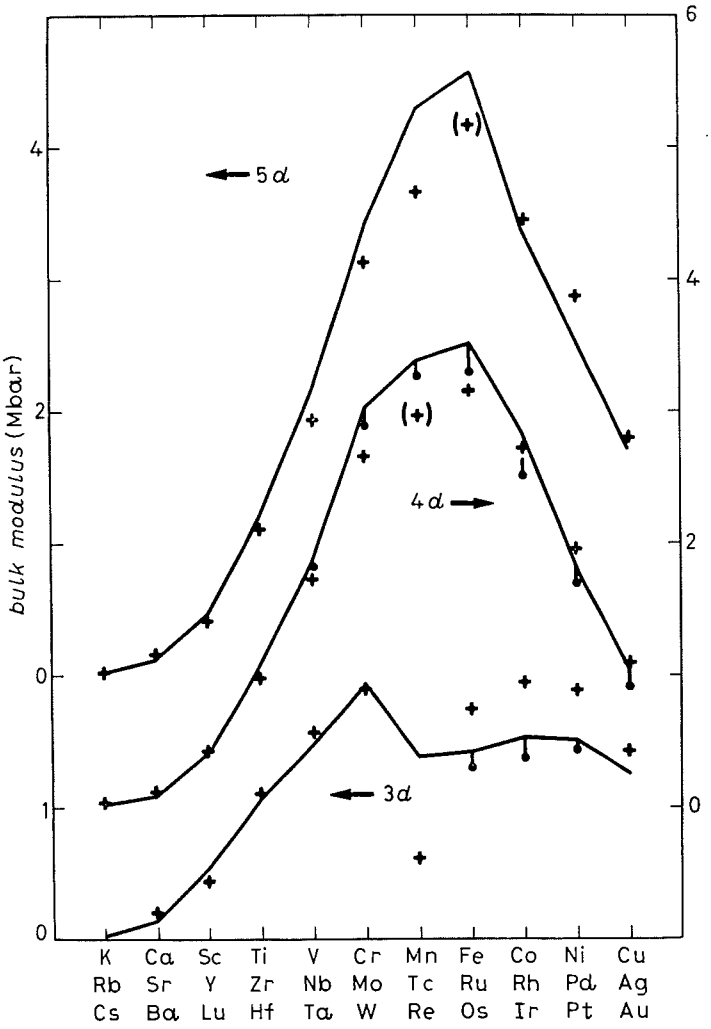

Fig. 25. – Bulk moduli for the 3*d*, 4*d* and 5*d* series. The lines and the full dots are the theoretical ASA values evaluated at the experimental equilibrium volumes. The full dots for Fe, Co and Ni correspond to non-spin-polarized calculations. The values indicated by full dots for the 4*d* series include the most simple electrostatic correction to the ASA. The crosses give the experimental bulk moduli.

dots are the results of our non-spin-polarized calculations, the open triangles for Fe, Co and Ni are from our ferromagnetic spin-polarized calculations, which will be discussed in the following subsection, and the open dots are the experimental values. Our radii are consistently a few per cent smaller than the experimental ones and the discrepancy is somewhat larger than found in the KKR-MT calculations for the 3*d* and 4*d* series by MORUZZI *et al.* [54]. This suggests that part of the discrepancy is due to the assumption made in the ASA for an elemental metal that each nucleus is perfectly screened by the electronic charge cloud in the surrounding cell. In fig. 25 the crosses give the experimental bulk moduli and the line as well as the full dots give our theoretical bulk moduli in the ASA but evaluated at the *experimental* equilibrium volumes. The bulk modulus varies substantially with atomic

volume, and, had we evaluated the bulk moduli at the (too small) theoretical —rather than at the experimental—equilibrium volumes, our bulk moduli would have been up to 20 per cent larger than the experimental ones. For the 3*d* series the line includes for Fe, Co and Ni (but not for Mn) the effects of spin polarization and the full dots give the bulk moduli calculated without spin polarization. For the 4*d* series the full dots include the most simple electrostatic correction to the ASA [73].

Structural-energy differences have the order of magnitude mRyd per atom, and the task of evaluating them as the difference between two self-consistently calculated total energies requires outmost care and provides little insight. If the rearrangement of the atoms needed to go from one crystal structure to another were an infinitesimal one, one could, however, use the force relation (193) and calculate the structural-energy difference as the difference between the sums of the one-electron energies, calculated *for the same potential* in the two different crystal structures. In the ASA, one would furthermore neglect the electrostatic term (194). This simple, approximate method has been successfully applied in a number of cases, as we shall give examples of below, and this recently led MCMAHAN *et al.* [84] to compare numerically the correct difference-of-total-energies method with the first-order force theorem method. (In both cases the combined correction to the ASA (subsect. 4·8) was used for the one-electron energies and (43) was employed for the total-energy calculations.) MCMAHAN *et al.* considered the f.c.c., h.c.p. and b.c.c. phases of Na, Mg, Al and Si for atomic volumes ranging from the normal ones and down to tenfold compression, and it was generally found that the structural-energy differences calculated with the two methods agreed within 2 per cent, or, for the smaller differences, to within 0.05 mRyd per atom. With one exception, the calculations agreed with the known experimental facts, a number of high-pressure phase transitions were predicted, and the results could be qualitatively understood on the basis of the volume dependence of the band structure, in particular the down movement of the 3*d*-band and the position of the Fermi level. (The one exception was that Na was predicted to be h.c.p. rather than b.c.c. at normal volume, even after the zero-point motion has been taken into account. This discrepancy, however, now seems to be due to insufficiently converged Ewald summations in the evaluation of the bare structure constants.)

SKRIVER [85] used the force theorem approximation for a similar study of the structural stability, as a function of pressure, for the divalent metals Be, Mg, Ca, Sr, Ba, Eu and Yb. At normal volume he obtained the b.c.c.-f.c.c. and h.c.p.-f.c.c. structural-energy differences shown in fig. 26 and, as seen, the stable structures are correctly predicted. Here again, the structural trends could be correlated with the degree of hybridization with the nearly empty *d*-band. A measure of this hybridization is the number of *d*-electrons, n_d (table V).

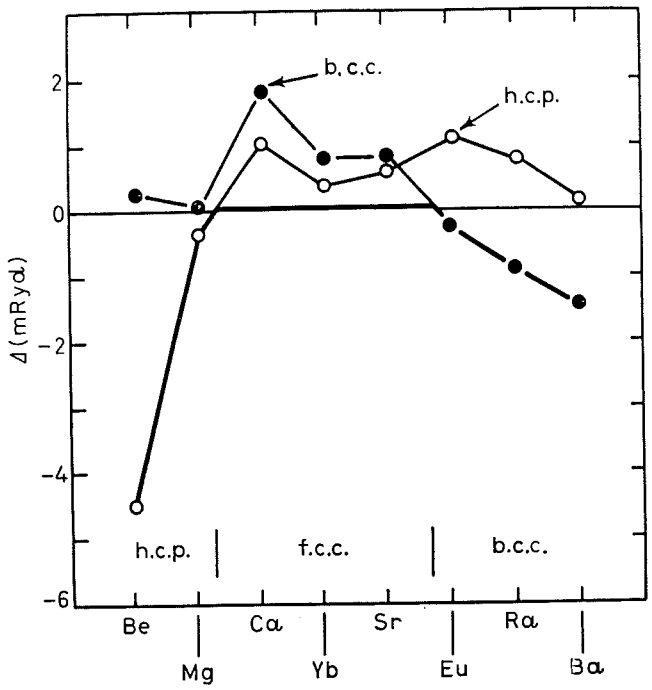

Fig. 26. – Structural-energy differences b.c.c.-f.c.c. and h.c.p.-f.c.c. for divalent metals as calculated from the force theorem by SKRIVER [85]. The structures observed at normal pressure (≈ 0) are indicated at the abscissa.

For the nonmagnetic transition metals the structural sequence at normal atomic volume is h.c.p. (Sc, Y, Lu), h.c.p. (Ti, Zr, Hf), b.c.c. (V, Nb, Ta), b.c.c. (Cr, Mo, W), h.c.p. (Tc, Re), h.c.p. (Ru, Os), f.c.c. (Rh, Ir) and f.c.c. (Ni, Pd, Pt). If we use the force theorem approximation and, furthermore, consider the unhybridized bare canonical d-bands only and neglect the small potential parameters Q_d and p_d, the structural-energy difference is simply the difference between the first canonical moments

$$\int^{S(n_d)} S N_d(S)\, \mathrm{d}S \tag{211}$$

in units of $\Delta_d = (\mu_d s^2)^{-1}$. Here $N_d(S)$ are the densities of states shown in fig. 27 of the bare canonical d-bands illustrated in fig. 14 and 15. The result of (211) is shown in fig. 28 as a function of the band filling, n_d, and it is similar to the one obtained earlier by PETTIFOR [64]. The stability of the b.c.c. structure in the middle of the series is clearly associated with the pronounced depletion of states seen in fig. 27 near the centre of the b.c.c. d-band. Figure 28*b*) accounts qualitatively for the crystal structures of the nonmagnetic transition metals, apart from the occurrence of the f.c.c. structure at the end of the series. A most recent calculation [86], still based on the force theorem approximation but including the hydridization and the combined correction term, yields the correct crystal structures for all transitional metals.

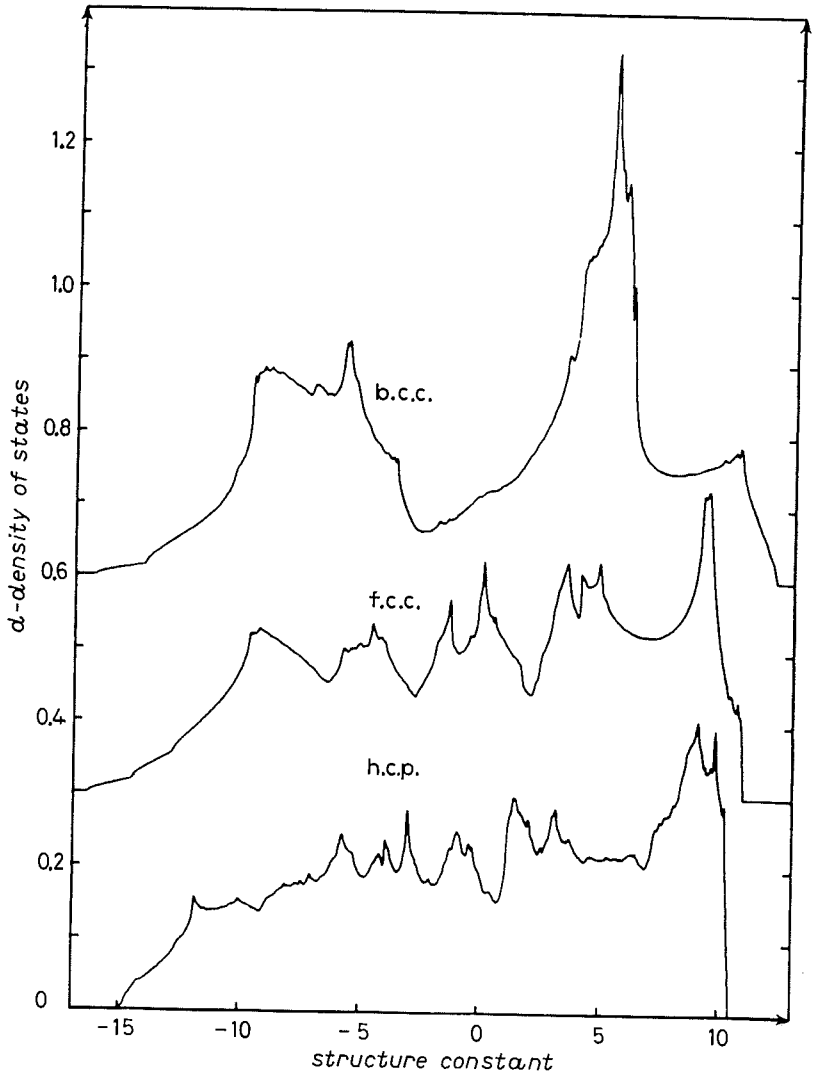

Fig. 27. – Densities of states per spin for the bare canonical *d*-bands.

The elastic constants of the transition and noble metals have been calculated successfully [79] from the force theorem with careful consideration of the electrostatic term and with energy bands calculated in the usual ASA-plus-correction-term way. Moreover, it should be possible in the near future to go beyond the so-called rigid MT, or rigid ASA, approximation used, for instance, by GLÖTZEL *et al.* [87, 88] to study the electron-phonon interaction in the transition metals.

The crystal structure sequence h.c.p., Sm., d.h.c.p., f.c.c. observed both for increasing pressure and for decreasing atomic number from right to left across the trivalent rare-earth series was explained qualitatively by DUTHIE and PETTIFOR [89] using bare canonical *d*-bands. The sequence arises when the number of *d*-electrons is increased from about 1.5 in Lu to about 2.5 in La as a result of the increasing relative size of the core which causes the *sp*-band to rise and thereby pour some of its electrons into the *d*-band.

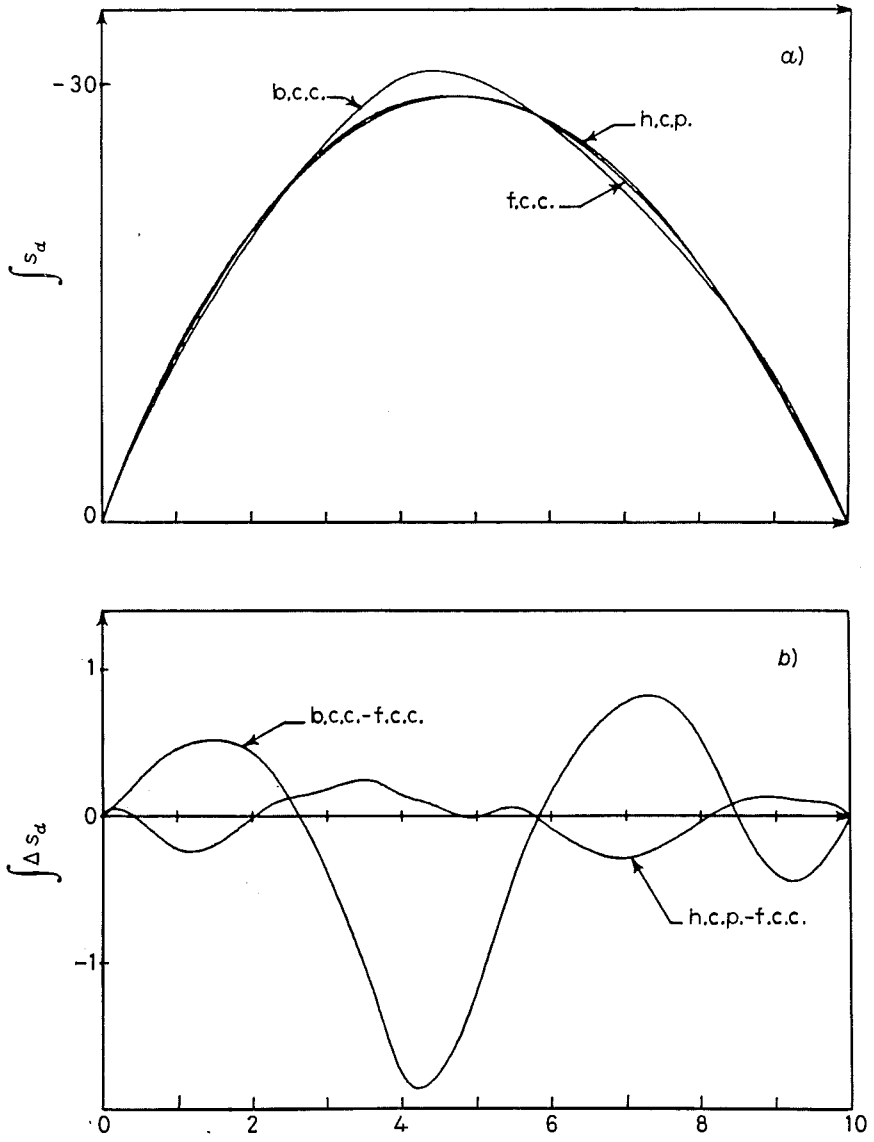

Fig. 28. – First moment of the bare canonical d density of states for the f.c.c., b.c.c. and h.c.p. structures (a)) and their structural differences (b)), as a function of the d occupancy.

6·2. *Magnetic properties.* – The density-functional formalism has been generalized to a spin density scheme [1, 90] in which, instead of the density, $n(\boldsymbol{r})$, the elements, $n(\boldsymbol{r}\sigma, \boldsymbol{r}\sigma')$, of the density matrix are the independent variables and in which the external potential has the form $v_{\text{ext}}(\boldsymbol{r}\sigma, \boldsymbol{r}\sigma')$. This is the generalization which allows inclusion of the spin-orbit coupling and a magnetic field in the external potential, and hence the calculation of spin susceptibilities. In the *local*-spin-density (LSD) approximation, the exchange correlation energy, $E_{\text{xc}}\{n(\boldsymbol{r}\sigma, \boldsymbol{r}\sigma')\}$, is expressed in terms of the exchange correlation energy, $\varepsilon_{\text{xc}}(n\uparrow, n\downarrow)$, per electron for a homogeneous electron gas with density $n \equiv n\uparrow + n\downarrow$ and spin density $m \equiv n\uparrow - n\downarrow$, as created by an external, homogeneous magnetic field. The corresponding exchange correlation potential is diagonal in

the spin variable and hence, to first order in m,

$$V_{xc}(\boldsymbol{r}^{\uparrow}_{\downarrow}) = \mu_{xc}(n) \pm \tfrac{1}{3}\delta(n)\mu_x(n)m/n\,, \tag{212}$$

where $n \equiv n(\boldsymbol{r})$, $m \equiv m(\boldsymbol{r})$, $\mu_x(n) = -\frac{4}{3}0.916/r_s$, and the effect of correlation is to reduce the function $\delta(n)$ from 1, in the high-density limit, to about 0.55 for $r_s = 4$.

If we now neglect the spin-orbit coupling and consider a para- or ferromagnet in the presence of a uniform magnetic field, $\mathscr{H}$, the band structure problem (1) is decoupled into separate equations for each direction of spin and the external plus exchange correlation potentials are given by $\mp\mu_B\mathscr{H}$ plus (212), where μ_B is the Bohr magneton. In all other cases, say for an antiferromagnet, where the spin density $m(\boldsymbol{r})$ varies periodically with zero average value, the Bloch functions have mixed spin-up and spin-down character. By solving the spin-polarized band structure problem self-consistently, one may calculate zero-temperature spin magnetizations, m, spin susceptibilities, $\chi \equiv \mu_B \cdot \mathrm{d}m/\mathrm{d}\mathscr{H}$, and magnetic contributions to the cohesive properties.

For small relative magnetizations, *i.e.* when $m(\boldsymbol{r})/n(\boldsymbol{r}) \ll 1$ at all points in space, the LSD theory may be approximated by a Stoner formalism. If, for instance, we treat the spin-dependent parts of the potential by first-order perturbation theory [70, 91], we find that the exchange splitting in a ferromagnet, or in a paramagnet subject to a uniform magnetic field, is given by

$$\Delta E = E^k_{j\downarrow} - E^k_{j\uparrow} = \tag{213}$$
$$= 2\mu_B\mathscr{H} - m\left\langle \psi^k_j(\boldsymbol{r}) \left| \frac{2\delta(n(\boldsymbol{r}))\mu_x(n(\boldsymbol{r}))m(\boldsymbol{r})}{3n(\boldsymbol{r})m} \right| \psi^k_j(\boldsymbol{r}) \right\rangle \equiv 2\mu_B\mathscr{H} + mI\,.$$

Here the Stoner parameter I and hence ΔE are only strictly independent of $\boldsymbol{k}$ on the constant-energy surface, $E^k_j = E$, if we assume that $n(\boldsymbol{r})$ and $m(\boldsymbol{r})$ are spherically symmetric in each atomic sphere and that only one partial wave contributes to the one-centre expansion (32) of the wave function. The values of I obtained by averaging over the (non-spin-polarized) Fermi surface [92, 93] are given in fig. 29. The trend shown for I may be explained from (213) by the fact that I, for a given density, $n(\boldsymbol{r})$, is larger for free-electron–like s- and p-waves than for more localized d-waves, because the former include a large contribution from the factor $n^{-\frac{2}{3}}(r)$ in the outer region of the cell. The minimum found in the middle of the series is caused by the mixing of the s-, p- and d-waves and the variation of the density. This trend was pointed out by JANAK [93], who calculated the I's for all metals up to and including In. His results for the $3d$ and $4d$ series are in close agreement with ours.

The static spin susceptibility is given by the well-known expression

$$\chi = 2\mu_B^2 N(1 - IN)^{-1}\,, \tag{214}$$

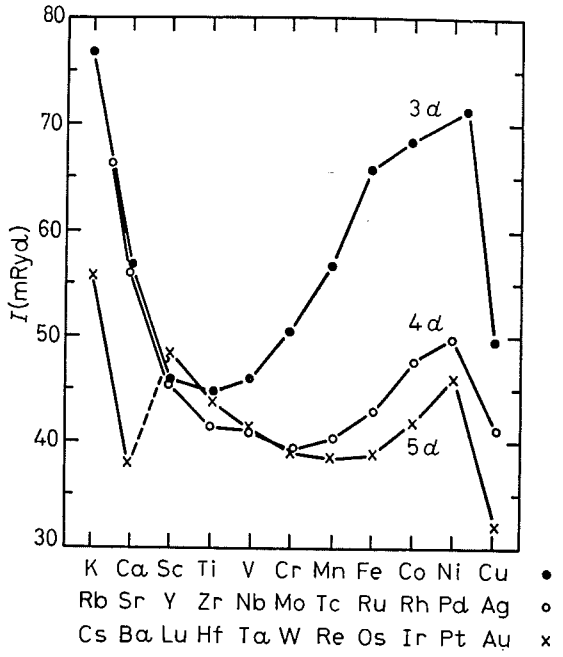

Fig. 29. – The LSD Stoner parameter for the $3d$, $4d$ and $5d$ series calculated [2] with the LMTO-ASA method, with the procedure of Janak [93] and with the exchange correlation potential of Barth and Hedin [90].

where N is the density of states per spin at the Fermi level. Among the non-magnetic metals it is only in Pd, where the Fermi level falls at the peak at the top of the f.c.c. d density of states (fig. 27), that NI is so large that the spin susceptibility dominates the orbital and diamagnetic contributions. The measured susceptibility of $7 \cdot 10^{-4}$ e.m.u./mol is in reasonable agreement with the theoretical spin susceptibility of $4 \cdot 10^{-4}$ e.m.u./mol, considering that $IN = 0.815$ and that an uncertainty in $C_d - V_s$ of 10 mRyd will change the Fermi energy by about 1 mRyd, and hence the density of states by about 10 per cent. The correlation effects included in the LSD approximation are crucial for a proper description of magnetic effects; with exchange only ($\delta = 1$ in (212)) Pd would be a strong ferromagnet.

The values of I become large at the second half of the $3d$ series and this, together with the presence of the narrow d-bands, causes the spontaneous antiferromagnetism of Cr [94] and Mn [95] and the ferromagnetism of Fe, Co and Ni. Results of our self-consistent ferromagnetic [90] calculations for b.c.c. Fe, h.c.p. Co and f.c.c. Ni may be found in tables IV and VI. Like previous authors [70, 96, 97] we find extremely good agreement between the calculated spin moments of, respectively, 2.18, 1.60 and 0.60 μ_B per atom and the experimental saturation moments corrected for the deviation of the g-factor from two. For Ni the value of the exchange splitting is found from table IV to be $C_{d\downarrow} - C_{d\uparrow} = 44$ mRyd at the centre of the d-band. At the Fermi level the I value of 72 mRyd obtained from fig. 29 and the moment of 0.60 μ_B per

atom yields the nearly identical value $mI = 43$ mRyd. These values of the exchange splitting are nearly twice as large as what has been measured in angular-resolved photoemission experiments [98] and the solution of this discrepancy, plus the related one found for the elemental semiconductors where the gaps obtained with LD theory are smaller than the experimental ones, is an urgent problem which has been and is being pursued along different paths [1, 99-102]. In this connection it might be mentioned that for the transition metals the fine structure (on the scale of 0.1 Ryd) found in the X-ray absorption spectra, from the Fermi level and 5 Ryd upwards (see fig. 3), is generally in good agreement with LD calculations [19, 103].

If we use the Stoner equation (213) with a $\boldsymbol{k}$-independent exchange splitting, the self-consistency condition for a ferromagnet is that the integral of the paramagnetic-state density (per spin) over the energy range ΔE equals the magnetization m. This is illustrated for b.c.c. Fe (in the absence of an external magnetic field) in fig. 30. In terms of a function $\bar{N}(n, m)$, which is the density of states averaged about the Fermi level corresponding to an occupancy of $n/2$ spins, over a range corresponding to m spins, self-consistency requires that $m/\Delta E = \bar{N}(n, m)$ and, when combined with (213), this yields the Stoner

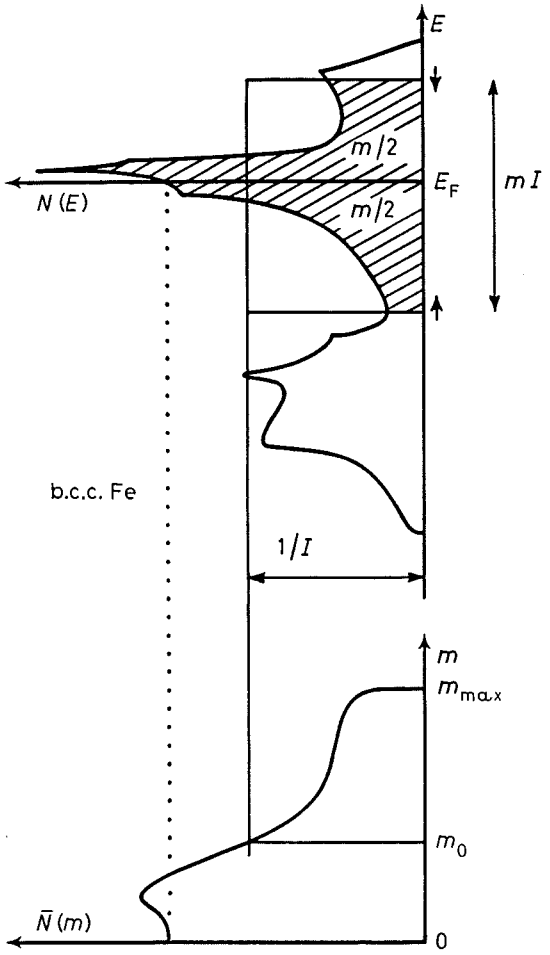

Fig. 30. – Stoner criterium for ferromagnetism illustrated for b.c.c. iron.

condition

$$(I + 2\mu_B \mathscr{H}/m)\, \bar{N}(n, m) = 1 \tag{215}$$

which determines the magnetization m_0 and leads to (214) when there is no spontaneous magnetization [104].

From fig. 24 and 25 we realize that the magnetic metals have relatively large atomic volumes and abnormal bulk moduli and that the spin-polarized calculations for Fe, Co and Ni only account for a fraction of these anomalies. In a band description this increase of atomic volume arises mainly because, with a spin polarization, m, the attractive d-bond pressure (209) is reduced by the amount

$$\begin{aligned} (216) \qquad & 3[\mathscr{P}_{d\,\mathrm{bond}}(m) - \mathscr{P}_{d\,\mathrm{bond}}(0)]\mathscr{V} = \\ & = -(25\Delta_d)[\tfrac{1}{2}(n+m)(10-n-m) + \tfrac{1}{2}(n-m)(10-n+m) - n(10-n)]/4 = \\ & = 25\Delta_d m^2/4\,. \end{aligned}$$

In other words, the attractive d-bond pressure (209) without spin polarization follows the curve shown in fig. 28*a*) as a function of the d-band occupancy n. The pressure with spin polarization is the average of the values obtained for the two subband occupations, $n + m$ and $n - m$, and it is obvious that this average is smaller than the value at n by an amount proportional to $m^2 + o(m^2)$. In case of a half-full band ($n = 5$) and full spin polarization ($m = 5$) the entire d-bond pressure will be lost because the two subbands are, respectively, full and empty.

In subsect. **6**'3 we mentioned—and gave the reason for—the trend by which a d-band narrows with increasing occupancy. If the band becomes sufficiently narrow, the Coulomb repulsion between the electrons in the narrow band will cause them to avoid each other by localizing them on the individual atoms. In this way the contribution of the narrow-band electrons to the chemical binding will be lost. In fig. 31 we show the experimental (dots) lattice constants for the series of $3d$ metals (shown previously in fig. 24), the $3d$ monoxides and the $5f$ actinide metals. The large lattice constants in the second half of these three series is a signature of the localization of, respectively, the $3d$- and the $5f$-electrons.

In the case of a half-full band the LSD band picture allowing for ferromagnetic spin polarization has the possibility of mimiking this loss of cohesion in the way described in connection with eqs. (215) and (216) and fig. 30. Whether this description will yield the correct cohesive (and magnetic) properties or not depends on the size of I and the width and shape of the band. If the band is being increasingly occupied (or emptied) beyond half-filling, as is the case for Fe, Co and Ni, the maximum possible loss of attractive pressure

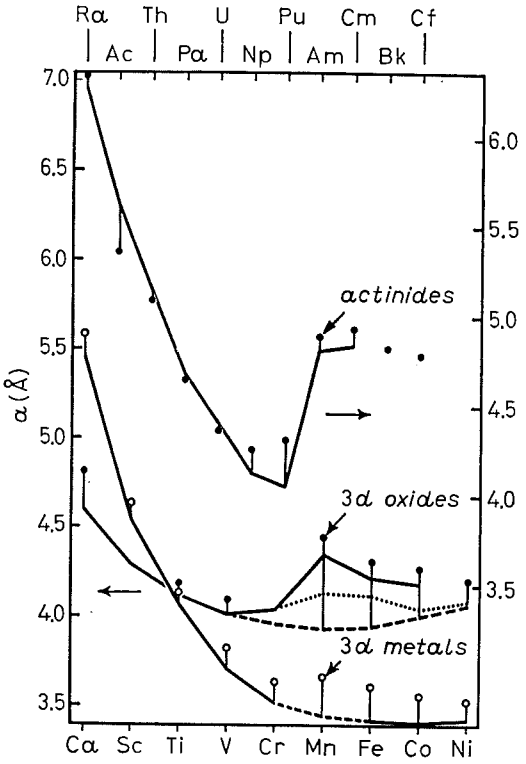

Fig. 31. – Experimental and theoretical lattice constants for the series of 3*d* metals [2], the 3*d* monoxides [74] and the 5*f* actinide metals [61]. For the monoxides having the NaCl structure, *a* is the lattice constant, while for the elemental metals, having various closely packed crystal structures, *a* is the lattice constant of the f.c.c. structure with the proper atomic volume. o, • experiment; ——— theory, nonferro- or antiferromagnetic; ··· theory, ferromagnetic; – – – theory, nonmagnetic.

diminishes rapidly for a band ferromagnet because, according to (216) and fig. 30, it is proportional to the number of holes ($m_{\max}$ in fig. 30) squared. To our knowledge there has been no real LSD calculation of the lattice constant of Mn due to its complicated crystal structure and antiferromagnetic spin alignment, but, as seen from the full curve in fig. 31 for Fe, Co and Ni, the LSD description underestimates the loss of cohesion due to the Coulomb correlation. This would be remedied if both I and the d-band width were reduced towards the end of the 3*d* series.

Antiferromagnetic (AF) spin polarization allows for a better band description of this interatomic correlation effect because in an antiferromagnet an up-spin electron has difficulty in hopping onto a neighbouring site because the majority spin direction at that site is « down », such that the potential at that site is shifted upwards by the amount mI_{AF}. The subband widths in an antiferromagnet are, therefore, smaller than in a ferromagnet and the subbands repel each other. A smaller « exchange » field is, therefore, needed to separate them. The associated loss of cohesion is somewhat reduced by the repulsion between the subbands, which takes place in an antiferromagnet

but not in a ferromagnet, because this repulsion lowers the energy of the majority band and thereby *increases* the cohesion.

Of the 3*d* monoxides shown in fig. 31 CaO is an ordinary ionic insulator, TiO and VO are paramagnetic metals, MnO has a half-full *d*-band and is an AF insulator, and so are FeO, CoO and NiO. LSD calculations [74, 105, 106] allowing for AF spin polarization predict this transition of ground state occurring in the second half of the series and, as seen from the solid line in fig. 31, the associated upwards jump of the lattice constant is reproduced quite well. Except in MnO the gap at the Fermi level for the AF insulators is, however, either nonexistent or far too small [47, 74, 105, 106].

In the series of actinides the localization of the 5*f*-electrons occurs at americium which has a nearly half-full 5*f*-shell. Since the contraction of the 5*f*-shell through the first part of the actinide series is much more pronounced than the contraction of the 3*d*-shell through the transition or monoxide series, and since the 5*f*-band widths depend more sensitively on the lattice constant than do the 3*d*-band widths, LSD calculations [61], allowing only for ferromagnetic spin polarization, neglecting the spin-orbit coupling and using the f.c.c. structure, produce the trends of the lattice constants and bulk moduli (fig. 32) well. Even the theoretical pressure-volume curve of Am, given in fig. 33, and the prediction of a first-order phase transition where the 5*f*-elec-

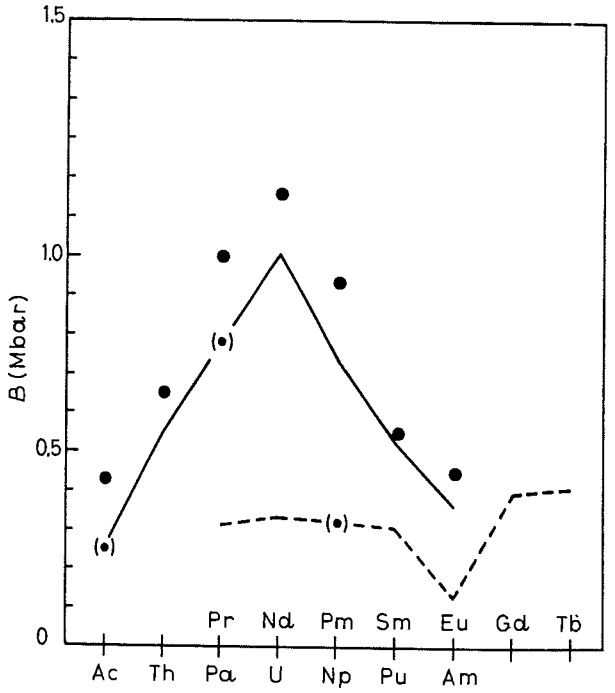

Fig. 32. – Bulk moduli for the first half of the actinide series. The calculations were performed for the f.c.c. structure at the experimental lattice constant, neglecting spin-orbit coupling and allowing only for ferromagnetic spin polarization [61]: • present calculation, ——— experimental values (actinides), – – – experimental values (rare earths), (•) estimated values.

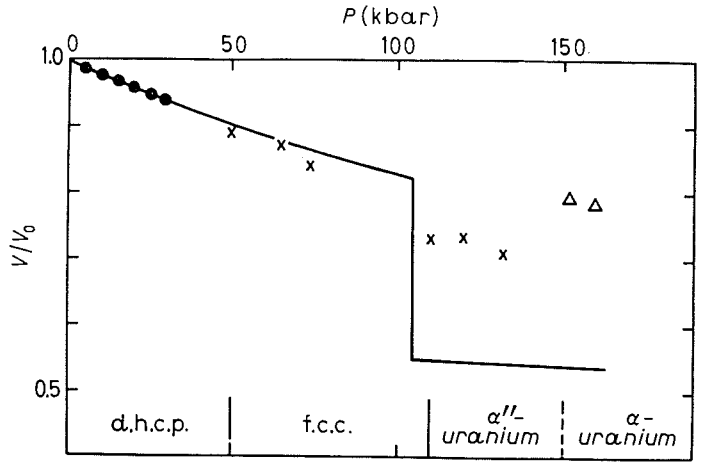

Fig. 33. – Pressure-volume curve for americium. The theoretical curve is for the f.c.c. phase [61]. • STEPHENS *et al.*, × SMITH *et al.*, △ ROOF *et al.*, ——— calculations.

trons delocalize at about 100 kbar has essentially been confirmed by subsequent measurements.

The quite successful treatment by LSD theory of narrow-band materials with a half-full band is perhaps most clearly demonstrated in the total-energy calculation (fig. 34) by KELLY *et al.* [75] for hydrogen. This calcula-

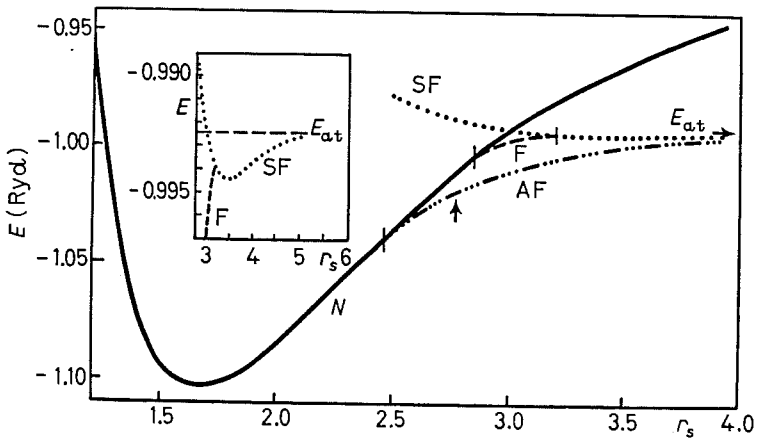

Fig. 34. – Total energy of b.c.c. hydrogen as a function of the Wigner-Seitz radius, r_s, for the nonmagnetic (N), ferromagnetic (F), antiferromagnetic (AF) and strongly ferromagnetic (SF) phases [75].

tion was performed for the Wigner-Seitz radius varying from 1.5 to 5 a.u. and in the nonmagnetic (N), ferromagnetic (F) and antiferromagnetic (AF) phases, as well as in the magnetic-field stabilized, strongly ferromagnetic (SF) phase. In the AF phase the metal-insulator transition takes place for $s \approx 2.7$ a.u. For $s \geqslant 3$ the energy difference between the F and AF phases

agrees within 20 per cent with the nearly exact values derived from the singlet-triplet splitting in the H_2-molecule and the pair approximation.

The question of whether a pressure-induced high-spin, low-spin transition in a ferromagnet is gradual or of first order and associated with a volume collapse depends in band theory on the shape of the density of states [70]. Let us consider the case of b.c.c. (α) and f.c.c. (γ) iron. From fig. 30 and with the assumption of a canonical d-band plus the fact that the Stoner I is largely independent of the atomic volume [104], it is clear that an increase of the atomic volume will reduce the density-of-states curve and, hence, reduce the spontaneous moment, m_0. It is now practical to rescale fig. 30 such that the densities of states and $1/I$ become multiplied by the band width parameter Δ. Scaled in this way $\Delta N(E)$ and $\Delta \bar{N}(m)$ are independent of atomic volume and Δ/I increases with pressure. The self-consistently calculated moment-volume curve for b.c.c. Fe is shown in the upper part of the left-hand side of fig. 35,

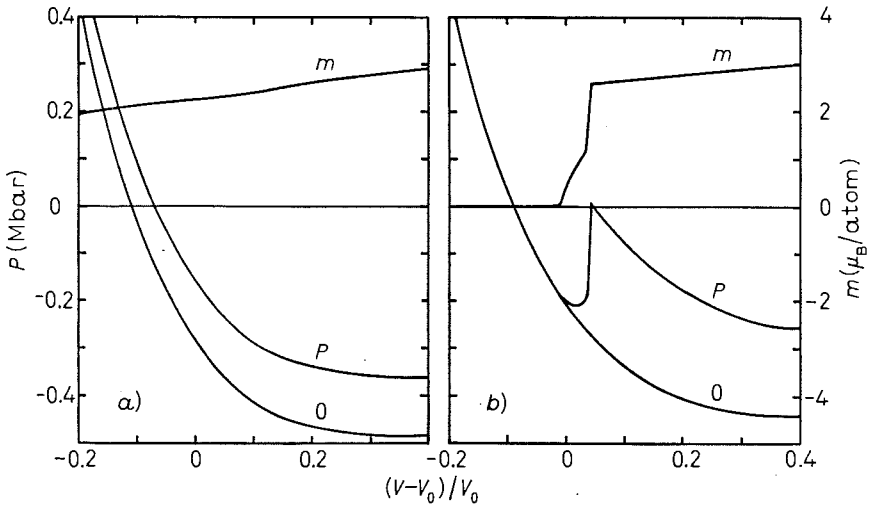

Fig. 35. – The magnetic moment (m) and the pressure calculated with (P) and without (0) spin polarization for *a*) b.c.c. and *b*) f.c.c. iron as a function of the atomic volume [70].

and the moment is seen to be quite slowly varying because this curve reflects the steep slope of $\bar{N}(m)$ in fig. 30. The magnetic pressure, proportional to m^2 (216), is, therefore, also slowly varying. This is shown at the bottom of the left-hand side of fig. 35 as the difference between the pressure calculated with (P) and without (0) spin polarization. If, however, instead of the b.c.c. density of states, which is strongly peaked at the (nonpolarized) Fermi level of Fe, we use the f.c.c. density of states, which from fig. 27 is seen to be rather flat near the Fermi level, the corresponding $\bar{N}(m)$ curve in fig. 30 will be rather low and flat in the m range from zero and nearly up to the band edge, m_{max}, which equals the number of holes in the (nonpolarized) d-band. As a consequence, the moment will depend strongly on volume and may even jump,

and so will the magnetic pressure. This is shown in the right-hand side of fig. 35 and it is seen that f.c.c. Fe according to the self-consistent calculation [70] has two stable states: a low-volume, nonmagnetic state and a high-volume, high-moment state.

Now, f.c.c. Fe is unstable with respect to b.c.c. Fe at zero pressure, but GRADMANN *et al.* [107] have been able to measure the magnetic moment of a few monolayers of f.c.c. Fe grown epitaxially on substrates of noble-metal alloys of varying lattice constant. The measured moments are the points in fig. 36 and, apart from those for the thickest layer which presumably does not follow the lattice constant of the substrate, they are in good agreement with the theoretically predicted [70] rapid variation in f.c.c. bulk Fe.

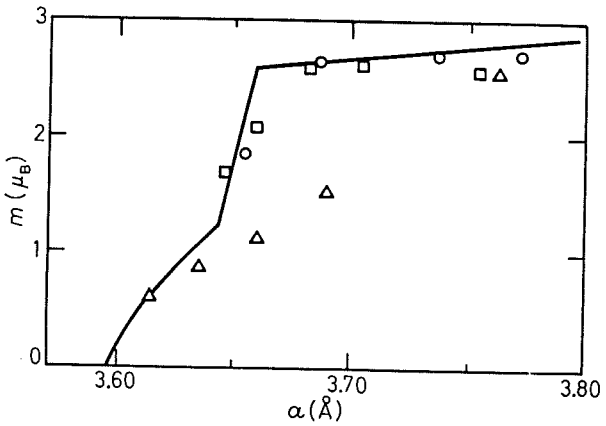

Fig. 36. – Magnetic moment of f.c.c. iron as a function of the lattice constant. The full curve is the theoretical value [70]. The measured values (o, □) [107] are for 2 layers and △ are for 2.9 layers of Fe on CuAu substrates. Experimentally the lattice constant was varied by varying the Au content in the substrate and assuming equal lattice constants of the Fe film and the substrate. The Fe lattice constant might be smaller than the CuAu lattice constant for the 2.9 layer film due to island formation.

The crystal structures of the magnetic $3d$ metals are generally different from those of their nonmagnetic $4d$ and $5d$ counterparts. Fe, for instance, is b.c.c., while Ru and Os are h.c.p. By reducing slightly the magnetic moment in b.c.c. Fe by the application of about 100 kbar pressure, it is possible to induce a phase transition to the h.c.p. structure, at which point the moment vanishes. The fact that a transition metal with spin-up and spin-down d-band occupancies of, respectively, $6.5 + 2.2$ and $6.5 - 2.2$ is b.c.c. follows immediately from fig. 28 and so does the fact that the h.c.p. structure becomes stable when the moment is just slightly reduced. The vanishing of the moment, once the h.c.p. phase has formed, follows from the fact that the Fermi level of Fe falls in a broad valley of the h.c.p. d density of states (see fig. 27) such that the application of pressure in the h.c.p. phase will abruptly switch off the magnetic moment.

7. – Electronic-structure calculations for metallic compounds.

Due to their high computational speed and reasonable accuracy the LMTO-ASA and ASW methods have been used in numerous studies of the electronic structure, the chemical binding, the electron-phonon coupling and the magnetic moments in compounds of varying complexity (with up to 30 atoms per primitive cell). In this section we shall briefly mention a few typical of these applications.

JAN and co-workers have during the last eight years performed dHvA measurements of the Fermi surfaces and, parallel herewith, performed LMTO calculations of the electronic structures for a large number of intermetallic compounds. Most lately $LaSn_3$ was studied [108].

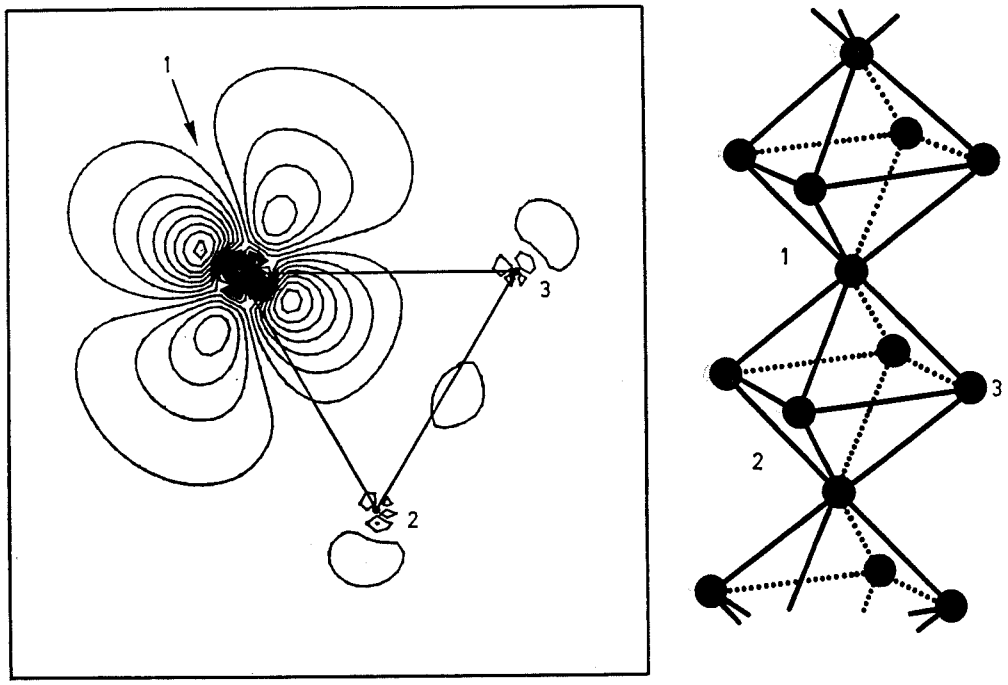

Fig. 37. – Directed d^4-orbital for a Nb_6F_{12} cluster (left-hand side). The back lobes of such orbitals enable the cluster to condense with other clusters and form, for instance, a string of corner-sharing clusters (right-hand side) [47, 51].

There exists a huge variety of ordered compounds where the building blocks are transition metal octahedra, placed in a cage of pnictides, chalcogens or halogens, rather than of individual atoms. Depending on the constituent elements, the cluster geometry, the way in which neighbouring clusters are joined together and the physical properties vary immensely. The string of corner-sharing Ti octahedra shown in the right-hand side of fig. 37 is the backbone of the ordered vacancy compound Ti_5O_5 occurring in the TiO system. Electronic-

structure calculations [47, 51] have shown that the structural stability of this compound, as well as of the ordered vacancy compound Nb_3O_3, where the strings extend in all three directions, is due to the formation of multicentre metal-metal bonds based on the directed *d*-orbital shown in the left-hand side of the figure. The ternary Chevrel phases with composition MMo_6X_8 form another family (with more than one-hundred members) of transition metal cluster compounds. $PbMo_6S_8$ is a superconductor with the presently highest known critical field of 60 T. The electronic structure of a large number of Chevrel phases, and of related compounds showing one-dimensional cluster condensation like in fig. 37, have been calculated [9, 76, 109] with the aim of throwing light on the chemical binding, the connection between structure and superconductivity and on the coexistence of superconductivity and magnetism found in some of the rare-earth molybdenum chalcogenides. In other transition metal cluster compounds, like Nb_6I_{11} and HNb_6I_{11}, the clusters are very loosely connected and the electrons are localized onto each transition metal octahedron which may then carry a magnetic moment. These compounds show interesting coupled structural and electronic phase transitions the nature of which was resolved by electronic-structure calculations [110].

Extensive studies of the electron-phonon coupling and the spin fluctuations in the family of A15 compounds, where the highest transition temperatures to superconductivity are found, have been performed by JARLBORG *et al.* [111] using the rigid MT or AS approximation and LSD theory. Moreover, the Fermi surface of V_3Si was calculated and found in good agreement with the one reconstructed from two-dimensional angular correlation of positron annihilation radiation [112]. MATTHEISS and HAMANN [113] used the LAPW method to calculate the charge density in V_3Si and found qualitative agreement but also significant differences with the charge densities derived from X-ray analysis.

Artificial layered materials (metallic superlattices) have recently been prepared by alternate decomposition of two transition metals. Such materials can have interesting mechanical, superconducting and magnetic properties. The magnetic properties of various structures of CuNi were recently studied by self-consistent spin-polarized calculations using large supercells [114]. In all cases the Ni moment was found to be reduced compared to f.c.c. Ni.

The magnetization per atom of transition metal alloys plotted as a function of the number of electrons per atom forms the so-called Slater-Pauling curve shown in fig. 38. The full lines in this figure [115] were obtained by using the construction [104] illustrated in fig. 30 together with the bare canonical b.c.c. or f.c.c. *d*-bands, the « rigid »-band approximation, the values of I shown in fig. 29 and the values of Δ_d given in table IV and interpolated between Ni, Co, Fe and Mn. The Invar alloys are those (usually Fe_xNi_{1-x}) f.c.c. alloys reached just after the b.c.c. phase has become unstable and they are characterized by having a nearly vanishing coefficient of thermal expansion. This was originally explained by WEISS [116] in terms of a two-level model

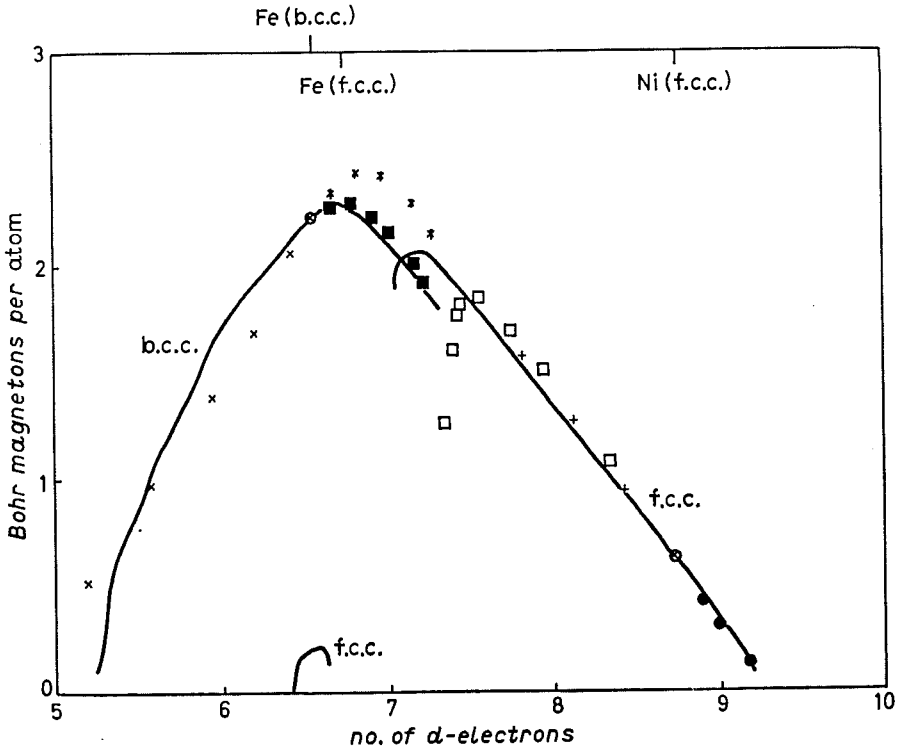

Fig. 38. – Magnetization per atom of transition metal alloys as a function of the number of electrons per atom: × Fe-Cr, ▪ Ni-Fe (b.c.c.), ▫ Ni-Fe (f.c.c.), ∗ Fe-Co, + Co-Ni, ● Ni-Cu, ⊗ pure metals [115].

according to which the higher level, which is populated with increasing temperature, has the lower volume. This model is, in fact, consistent with the two stable states found in f.c.c. Fe in fig. 35. Here the low-volume nonmagnetic state had an 8 mRyd lower energy (the integral under the $\mathscr{P}$-$\mathscr{V}$ curve) than the high-volume high-moment state. If, however, we use the canonical f.c.c. *d*-band in fig. 27 and shift the position of the Fermi level towards that of Ni, we find [115] that the $\mathscr{P}$-$\mathscr{V}$ curve in the right-hand side of fig. 35 essentially moves upwards. The result is that the energy difference between the two states decreases and finally, by the Invar composition, it inverts in agreement with the Weiss model. This behaviour was also noticed by PETTIFOR [117] and further investigated for f.c.c. FeNi by SKRIVER *et al.* [71]. Most recently this picture was confirmed through detailed spin-polarized total-energy calculations for f.c.c. Fe, Fe_3Ni and FeNi by WILLIAMS *et al.* [118]. The details of how an Invar alloy (*e.g.*, Fe_3Ni) fluctuates between the two states, however, remains an open question. WILLIAMS *et al.* also considered another well-known class of magnetic alloys, the Heussler alloys (X_2MnY), and studied their interatomic exchange coupling by comparing F and AF spin alignments. In a recent work [119] a generalized Slater-Pauling curve was introduced and the trends were explained on the basis of self-consistent spin-polarized band calculations.

The cohesive and magnetic ground-state properties of a number of light actinide pnictides and chalcogenides with the NaCl structure were studied by BROOKS [120]. For UN it was found [121] that the spin-orbit coupling in uranium includes a large orbital magnetic moment of $-1.5\mu_B$ antiparallel to the spin moment of $1.0\mu_B$. With this taken into account in the band theory the calculated size and shape of the magnetic form factor and the pressure dependence of the moment agree with the experimental values.

It is presumably realistic to expect that it will be possible within the next 5-10 years to calculate phase diagrams of alloys using parameter-free DF calculations. WILLIAMS *et al.* [122] have performed a huge number of self-consistent ASW total-energy calculations for pure elements and binary alloys as functions of atomic volume to determine the heats of formation for more than one-hundred transition metal-transition metal and transition metal-non-transition metal alloys. The results were generally similar to those given by the empirical scheme of Miedema [123], but the microscopic picture was quite different and, for transition metal-transition metal alloys, the picture derived from the calculations of Williams *et al.* was close to the *d*-bond picture proposed earlier by PETTIFOR [77]. KOLLAR *et al.* [78] recently restricted the ASA self-consistency procedure with the result that they could express the energy difference between the AB and the AA and BB systems in the spirit of the force theorem (subsect. **6**˙1) as the change in the sum of the one-electron energies (Σ) plus the self-energy (U) of the charge density change. These two terms are shown as a function of the charge transfer, q, between the atomic spheres for the noble-metal alloys in fig. 39. The minimum of $\Sigma + U$ yields the heat of formation and is marked with a $+$. In view of the smallness of the heats of for-

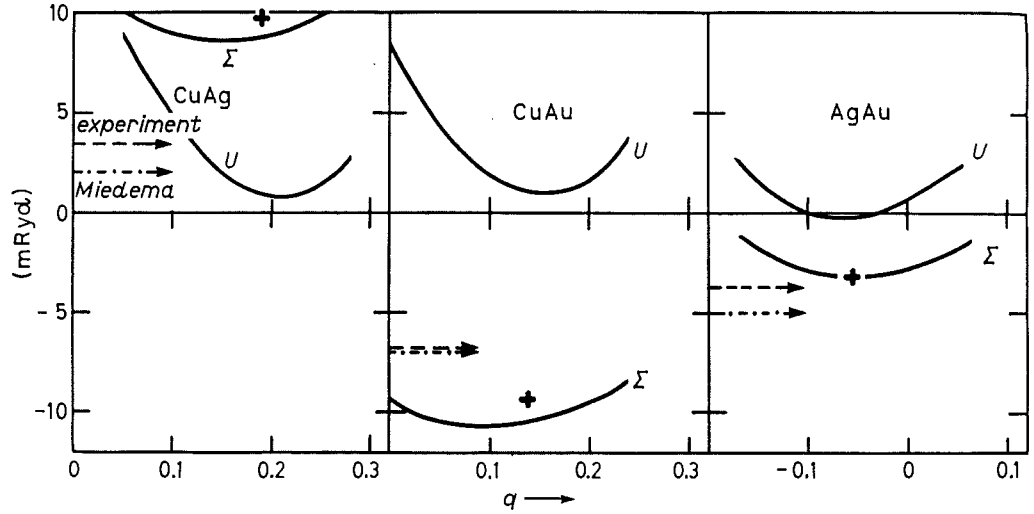

Fig. 39. – The sum of the one-electron energies (Σ) and the self-energy (U) of the charge density change for CuAg, CuAu and AgAu as a function of the charge transfer between the atomic spheres. The minimum of $\Sigma + V$ (indicated by $+$) gives the heat of formation of the alloy [78]. The experimental value and Miedema's empirical results [123] are shown as dashed and dash-dotted lines, respectively.

mations for the noble-metal alloys the approximate theoretical results are seen to be in good agreement with the experimental and with Miedema's empirical results. We thus reproduce the curious fact that CuAu and AgAu form, while CuAg does not. Since U is the self-energy of the charge transfer, it is positive definite and the one-electron estimate min $\{\Sigma(q)\}$, which corresponds to using pure-metal AS potentials for the alloy band structure, therefore represents a lower bound for the heat of formation. Figure 39 shows that for the noble-metal alloys this lower bound is indeed very close to the theoretical heat of formation. The approximate scheme of Kollar *et al.* may thus be used to interpret the heats of formation in a simple and quite general way and, if needed, to speed up the calculations. So far, however, it assumes the validity

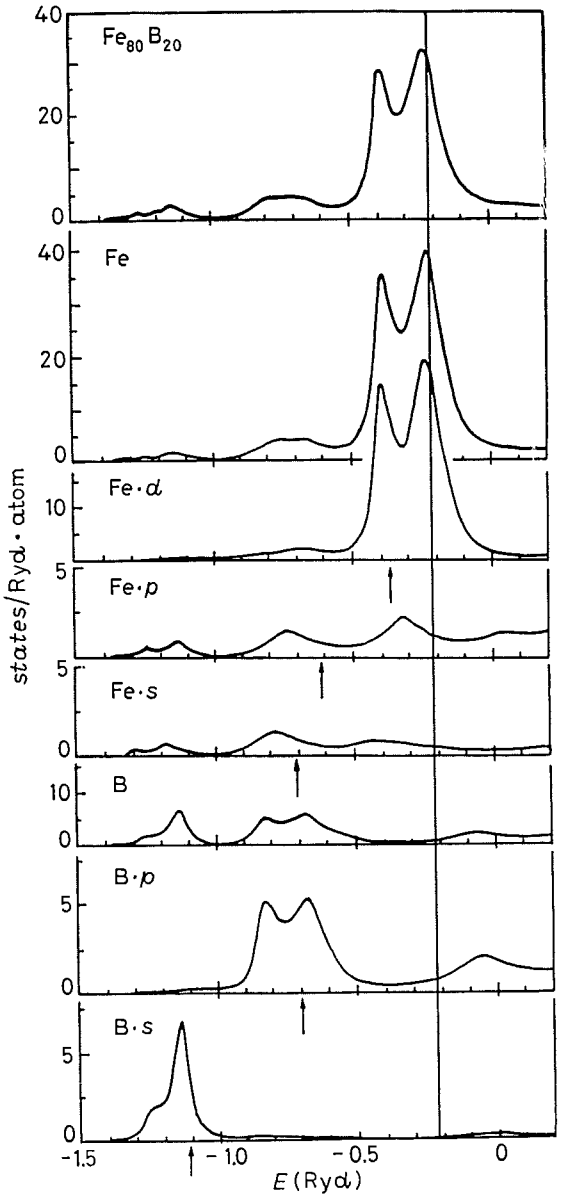

Fig. 40. – Average partial densities of states for the amorphous metal, $Fe_{80}B_{20}$. The vertical line indicates the Fermi energy and the arrows the E_v values [41].

of Vegard's law, *i.e.* that the atomic volume of the alloy equals the average of the atomic volume of the constituents. This assumption is, for instance, not justified for the interesting series of ionic compounds LiAu → CsAu whose electronic and cohesive properties were recently studied by KOENIG *et al.* [124].

In order to calculate the electronic structure of nonperiodic solids, it is necessary to use a set of localized orbitals in connection with a moment method [125] or the recursion method [42]. With the new localized MTOs introduced in sect. 4 FUJIWARA [41] has for the first time performed self-consistent calculations for amorphous metals. The average partial densities of states for $Fe_{80}B_{20}$ are shown in fig. 40. The strong mixing between the Fe and B orbitals may be observed, in particular does the B *s*-peak seen in the figure only contain 0.8 electrons and it, therefore, only represents the lower, bonding part of the B *s*-band. The antibonding part is at high energies outside the frame of the figure. With this new method it should now be possible to study the interesting magnetic properties of amorphous transition metals.

8. – Surface calculations.

In this section we shall review some calculations of surface properties using the LMTO method and the linear augmented-plane-wave (LAPW) method. Most of these calculations have been performed by the LAPW method.

Until now the main advantage of the LAPW method as compared with the LMTO method has been the ease with which a general potential with no shape approximation could be included. Near the surface the potential varies rapidly perpendicular to the surface (fig. 1) and hitherto this was not as easily incorporated in the LMTO method as in the LAPW method. With the new localized orbitals the situation may change. The disadvantage of the LAPW method is the large basis set. 40-60 basis functions per atom are necessary, while 9 orbitals per atom are sufficient in the LMTO method. This makes the computational speed of the latter superior to that of the former. Furthermore, the LAPW method is a brute-force method, because with basis functions derived from plane waves the physical interpretation of the results in terms of, for instance, bond orbitals is difficult. Finally the canonical picture of the band structure as described in this lecture is not utilized in this method.

KASOWSKI [126] was the first to study surface electronic properties by a LMTO-related method (the LCMTO method). He calculated the surface electronic structure of clean copper, tungsten and molybdenum. For the latter two, a possible relaxation of the surface layer was taken into account. Later he studied chemisorption of O, Na and CO on the Ni surface. More recently KASOWSKI and CARUTHERS [126] applied a modified version of this method to study the interaction on the Ni(001) surface of *a*) two CO molecules which

react on the surface to give free CO_2 and carbon on the surface, and *b*) formaldehyde whose CO bond is broken and CH_2 is formed.

Recently the LMTO method was extended to surface calculations [31]. Like in all uses of the LAPW method for surface studies referred to below, the film geometry consisting of 1-20 atomic layers was also adopted for the LMTO method. MA *et al.* [31] used their method to calculate the electronic structure of a noble-metal (Cu) monolager on transition metal (Ru or Ni) surfaces. They obtained good agreement with UPS measurements, which show shift to higher binding energy of the top of the Cu *d*-bands when Cu is deposited on the Ru surface, and with EELS experiments which show filling and narrowing of the Cu *d*-bands when Cu is deposited on a Ni substrate.

The rest of the calculations that we shall mention here were performed by the LAPW method. All relativistic effects were included in these calculations except the spin-orbit coupling.

JEPSEN *et al.* [15] performed spin-polarized calculations for a series of Ni(001) films of different thickness which enabled an extrapolation of the results to the semi-infinite crystal. The single most interesting result of these calculations is the enhancement of the magnetic moment at the surface which is roughly 10% larger than the bulk value. This prediction was later verified experimentally by spin-polarized LEED [127]. Recently a similar calculation for the Ni(110) surface by KRAKAUER *et al.* [128] also shows an enhanced moment at this surface. On the other hand, when one layer of Ni is deposited on Cu(001), the Ni magnetic moment is reduced by 37% [129], and, when the Cu surface is covered by two Ni layers, then the interface Ni layer has a moment reduction of 24%, while, in the surface layer, the moment is somewhat *increased* over the bulk value.

Ni catalyzes the formation of methane from carbon monoxide and hydrogen, but small amounts of sulfur reduce the reaction rate by orders of magnitude. In order to study the role played by sulfur as a catalytic poison, RICHTER *et al.* [130] calculated the electronic structure and charge density of a $c(2\times2)$ overlayer of sulfur on Ni(001). Charge is transferred from the Ni surface to sulfur and the authors speculate that the reduced Ni charge prohibits the breaking of the CO bond which is the first step in the catalytic process.

For the nearly-free-electron metal Al the electronic structures of both the clean (001) and (111) surfaces [131] as well as for oxygen chemisorbed on the (111) face [132] and Na chemisorbed on the (001) face [133] have been calculated. The results which are in good agreement with experiments include work functions, surface states and core level shifts.

The clean unreconstructed tungsten surface has been studied in some detail [134]. The energy and symmetry of the calculated surface states and resonances (SR) were found to be in general agreement with angular-resolved photoemission spectroscopy (ARPS) and field emission energy distribution data, in particular the so-called « Swanson hump » was accounted for. How-

ever, some recent ARPS measurements of the SR along $\bar{\Sigma}$ in the surface Brillouin zone and close to the Fermi energy differ substantially from the calculated values. A relaxation of the surface layer could not resolve this discrepancy. Furthermore, on the basis of the calculated surface susceptibility, the « nesting » features of the calculated SR bands along $\bar{\Sigma}$ were suggested to drive the $c(2\times2)$ reconstruction at low temperatures. This mechanism may, therefore, have to be revised on the basis of the new experiments. Since tungsten is a heavy transition metal it may be that spin-orbit coupling has to be included in order to obtain agreement with the experimental findings.

The low-temperature reconstruction of the W(001) surface can be healed by hydrogen adsorption. This was explained by RICHTER *et al.* [130, 135], who calculated the electronic structure and charge density of a dense $p(1\times1)$ layer of H on W(001) for different H-W separations. They found that hydrogen forms chemical bonds with the surface tungsten atoms and that the clean tungsten surface states dissapear. The hydrogen overlayer screens the outermost tungsten atoms from the perturbation of the vacuum with the result that the charge distribution of the outermost layer resembles that of the bulk.

The technologically important cesiated tungsten surface was studied by WIMMER *et al.* [136] with Cs in a $c(2\times2)$ coverage and for three different Cs-W distances. They found that the well-known reduction of the work function due to cesiation arises because Cs forms a metallic overlayer with its valence electrons shifted towards the W surface. This reduces the effective electrostatic surface barrier and the work function by 2 to 2.5 eV depending on the Cs-W separation.

The determination of the spatial position of surface atoms, adsorbed atoms and molecules is a major challenge in surface physics. The accurate surface geometry has been established only for very few systems and, by far, the most of these have been determined by LEED experiments interpreted by calculations. HAMANN [22] has suggested that atomic diffraction could be used as a complement to LEED. The atom-surface interaction potential is to lowest order proportional to the electron density far outside the surface [137]. This may readily be calculated, for instance, by the LAPW method, for different atomic positions at the surface and the best agreement with the interaction potential extracted from experimental atomic diffraction data may then determine the surface geometry. HAMANN tested this idea on, among other systems, hydrogen on Ni(110) and found best agreement between the theoretical and experimental interaction potential with hydrogen in the so-called « buckled bridge » position. In a similar way the Cl adsorption site on a Ag(001) surface was determined [138]. Two configurations which had been previously suggested by LEED analysis were tested: a simple-overlayer model (SOM) where the Cl ad-atoms occupy every second fourfold hollow site above the Ag surface layer, and a mixed-layer model (MLM) where the remaining fourfold hollow sites are filled with Ag atoms. Even with indetermined vertical distances of the Cl-Ag layer

the MLM could be excluded because it had an order of magnitude smaller corrugation than the SOM, in disagreement with experiments.

Finally we would like to mention two interesting surface calculations which appeared recently. They both concern transition metal overlayers on transition metal surfaces.

The first one [139] is for palladium on niobium. The clean Pd surface and the clean Nb surface adsorbe hydrogen while the Pd-Nb system has *zero* sticking coefficient. The calculations of El-Batanouny *et al.* for a Pd monolayer on a Nb(110) surface show that charge is transferred from Nb to Pd in agreement with the much larger electronegativity of Pd. Consequently the Pd *d*-bands are filled and the resulting surface band structure resembles that of a noble metal for which it is known that no dissociation of H_2 occurs.

In the second calculation [140] the clean, the Ag- and Pd-covered Rh(001) surface and the clean and Ag-covered Rh(111) surface were studied. Ag adsorption lowers the work function of Rh, while Pd has a negligible effect. This was explained in terms of the Pauling electronegativities. Ag has a smaller electronegativity (1.9) than Rh (2.2) and Pd (2.2). Therefore, Ag tends to transfer charge to the Rh substrate lowering its work function, while nearly no charge transfer occurs between Pd and Rh, leaving the work function unchanged. It is well known experimentally that the closest-packed surface has the highest work function, and this was confirmed here for the clean surfaces, as well as for the Ag-covered surfaces. From the calculated core level shifts the heat-of-adsorption differences were predicted and they were found to be in satisfactory agreement with the empirical values of Miedema and Dorleijn [141].

9. – Conclusion and outlook.

Ten years ago the popular methods for *accurate* solution of the one-electron problem for metals in general were the KKR and APW methods which treat this problem as one of scattering between spherically symmetric muffin-tin wells. These methods have now been superseded by their descendants, the linear methods (LMTO, ASW, LAPW, etc.), which have made self-consistent calculations feasible for realistic systems and as functions of external parameters such as the atomic positions. As a result, a vast number of parameter-free density-functional calculations of cohesive and magnetic ground-state properties have been carried out for a variety of metals and we have learned how surprisingly well the local approximation to density-functional theory works [1,142]. Moreover, we are on the way to obtain a simple, quantitative understanding of electronic properties such as chemical binding and magnetic structures. First attempts to obtain finite-temperature properties have appeared [143].

As a further step towards the goal of achieving a quantitative understanding of the properties of real materials under realistic conditions we have, in this lecture, shown how the linear methods, specifically the LMTO method, may be transformed exactly into a minimal-basis first-principles tight-binding method of the most simple, two-centre form. The hopping integrals factorize into products of atomic potential parameters and reduced so-called canonical-hopping integrals which only depend on the structure. In this way we believe to have bridged the gap between a class of well-tried first-principles methods and the empirical tight-binding [80], or Hückel [67, 82], methods upon which much of our present « intuitive » understanding of realistic systems is based.

A further ingredient of the empirical descriptions is to approximate the total eletronic energy by the sum of the one-electron energies. This, we have shown, can to some extent be justified from the so-called force theorem which is based on the stationary property of the total energy with respect to changes of the electronic density. Clearly, more work is needed, not only to establish the accuracy of the force theorem approach [144] for specific applications, such as structural energies or heats of formation which go beyond first-order perturbations, but also in order to explain the results, say in terms of a real-space description of the chemical bonding. Specifically, one might seek a connection between the first-principles description of forces or pressures in terms of individual orbital contributions and the chemist's empirical overlap population analysis.

We have summarized the electronic structure of 33 elemental metals by tabulating the reduced hopping integrals, as well as the self-consistently calculated potential parameters and their volume derivatives around the equilibrium atomic volume. These tables should be useful not only for studies of the properties of elemental metals but also for obtaining an estimate of the electronic properties of intermetallic compounds.

A computational advantage of the new tight-binding formulation is that it makes the treatment of a general, nonspherically symmetric MT or AS potential much simpler than previously [28-30] but this remains to be carried out in practice. Also, the formalism that we have given for displacing the atomic positions from those of a Bravais lattice has so far only been applied (to the case of amorphous metals) in the lowest order. This technique is clearly needed for the treatment [46] of atomic relaxations in the vicinity of an impurity, for the calculation of phonon spectra using the Fröhlich representation where the orbitals move with the atoms and for the calculation of the higher-order force constants.

Finally, when considering narrow $3d$- or $5f$-bands, we have seen the need to go beyond the local approximation to density-functional theory. This is an urgent problem.

REFERENCES

[1] P. HOHENBERG and W. KOHN: *Phys. Rev.*, **136**, B 864 (1964); W. KOHN and L. J. SHAM: *Phys. Rev.*, **140**, A 1133 (1965); O. GUNNARSSON and B. I. LUNDQVIST: *Phys. Rev. B*, **13**, 4274 (1976); W. KOHN: this volume, p. 1.
[2] A. R. MACKINTOSH and O. K. ANDERSEN: in *Electrons at the Fermi Surface*, edited by M. SPRINGFORD (Cambridge, 1980), p. 149.
[3] D. GLÖTZEL: in *Physics of Solids under High Pressure*, edited by J. S. SCHILLING and R. N. SHELTON (Amsterdam, 1981), p. 263.
[4] O. K. ANDERSEN: *Solid State Commun.*, **13**, 133 (1973).
[5] O. K. ANDERSEN: *Mont Tremblant Lectures 1973* (unpublished); O. K. ANDERSEN and G. WOOLLEY: *Mol. Phys.*, **26**, 905 (1973).
[6] O. K. ANDERSEN: *Phys. Rev. B*, **12**, 3060 (1975).
[7] O. JEPSEN: *Phys. Rev. B*, **12**, 2988 (1975); O. JEPSEN, O. K. ANDERSEN and A. R. MACKINTOSH: *Phys. Rev. B*, **12**, 3084 (1975).
[8] O. K. ANDERSEN and O. JEPSEN: *Physica (Utrecht) B*, **91**, 317 (1977).
[9] O. K. ANDERSEN, W. KLOSE and H. NOHL: *Phys. Rev. B*, **17**, 1209 (1978); H. NOHL, W. KLOSE and O. K. ANDERSEN: in *Superconductivity in Ternary Compounds*, I, *Topics of Current Physics*, Vol. **32**, edited by Ö. FISCHER and M. B. MAPLE (Berlin, 1982), p. 165.
[10] H. L. SKRIVER: *The* LMTO *Method* (Berlin, 1984).
[11] A. R. WILLIAMS, J. KÜBLER and C. D. GELATT jr.: *Phys. Rev. B*, **19**, 6094 (1979).
[12] O. K. ANDERSEN: *Europhys. News*, **12**, 5, 1 (1981); O. JEPSEN and O. K. ANDERSEN: in *Festkörperphysik 1981* (Weinheim, 1981), p. 350; O. K. ANDERSEN: in *The Electronic Structure of Complex Systems*, edited by W. TEMMERMAN and P. PHARISEAU (New York, N.Y., 1984), p. 11.
[13] O. K. ANDERSEN and O. JEPSEN: *Phys. Rev. Lett.*, **53**, 2571 (1984).
[14] O. JEPSEN, J. MADSEN and O. K. ANDERSEN: *Phys. Rev. B*, **18**, 605 (1978).
[15] O. JEPSEN, J. MADSEN and O. K. ANDERSEN: *J. Magn. Magn. Mater.*, **15-18**, 867 (1980); *Phys. Rev. B*, **26**, 2790 (1982).
[16] J. C. SLATER: *Phys. Rev.*, **51**, 151 (1937).
[17] J. KORRINGA: *Physica (Utrecht)*, **13**, 392 (1947); W. KOHN and J. ROSTOCKER: *Phys. Rev.*, **94**, 1111 (1954).
[18] Here and in the following we only consider infinite solids where the deep potential regions are nearly spherically symmetric. For the treatment of the surface potential see ref. [14, 15].
[19] D. D. KOELLING and G. ARBMAN: *J. Phys. F*, **5**, 2041 (1975). See also P. M. MARCUS: *Int. J. Quantum Chem. Suppl.*, **1**, 567 (1967).
[20] J. E. MÜLLER, O. JEPSEN, O. K. ANDERSEN and J. W. WILKINS: *Phys. Rev. Lett.*, **40**, 720 (1978); O. JEPSEN, J. E. MÜLLER, O. K. ANDERSEN and J. W. WILKINS: *Inst. Phys. Conf. Ser.*, No. **39**, 153 (1978); J. E. MÜLLER, O. JEPSEN and J. W. WILKINS: *Solid State Commun.*, **42**, 365 (1982).
[21] H. KRAKAUER, M. POSTERNAK and A. J. FREEMAN: *Phys. Rev. B*, **19**, 1706 (1979).
[22] D. R. HAMANN: *Phys. Rev. Lett.*, **46**, 1227 (1981).
[23] T. TAKEDA and J. KÜBLER: *J. Phys. F*, **9**, 661 (1979).
[24] O. K. ANDERSEN: in *Computational Methods in Band Theory*, edited by P. M. MARCUS, J. F. JANAK and A. R. WILLIAMS (New York, N.Y., 1971), p. 178.

[25] O. K. ANDERSEN and R. V. KASOWSKI: *Phys. Rev. B*, **4**, 1063 (1971); R. V. KASOWSKI and O. K. ANDERSEN: *Solid State Commun.*, **11**, 799 (1972).
[26] T. JARLBORG and G. ARBMAN: *J. Phys. F*, **6**, 189 (1976); **7**, 1635 (1977).
[27] O. GUNNARSSON, J. HARRIS and R. O. JONES: *Phys. Rev. B*, **15**, 3027 (1977).
[28] J. HARRIS and G. S. PAINTER: *Phys. Rev. B*, **22**, 2614 (1980); J. HARRIS: in *The Electronic Structure of Complex Systems*, edited by W. TEMMERMAN and P. PHARISEAU (New York, N. Y., 1984), p. 141.
[29] F. HERMAN and R. V. KASOWSKI: *Phys. Rev. B*, **17**, 672 (1978).
[30] F. CASULA and F. HERMAN: *J. Chem. Phys.*, **78**, 858 (1983).
[31] H. KRAKAUER and B. R. COOPER: *Phys. Rev. B*, **16**, 605 (1977); C. Q. MA, H. KRAKAUER and B. R. COOPER: *J. Vac. Sci. Technol.*, **18**, 581 (1981); C. Q. MA, M. V. RAMANA, B. R. COOPER and H. KRAKAUER: *J. Vac. Sci. Technol. A*, **1**, 1095 (1983).
[32] M. SPRINGBORG and O. K. ANDERSEN: to be published.
[33] J. W. DAVENPORT: *Phys. Rev. B*, **29**, 2896 (1984).
[34] N. E. CHRISTENSEN: *Phys. Rev. B*, **29**, 5547 (1984).
[35] J. H. WILKINSON: *The Algebraic Eigenvalue Problem* (London, 1965); R. S. MARTIN and J. H. WILKINSON: *Numer. Math.*, **12**, 377 (1968).
[36] P. O. LÖWDIN: *Adv. Phys.*, **5**, 1 (1956).
[37] W. HOBSON: *The Theory of Spherical and Ellipsoidal Harmonics* (New York, N.Y., 1955), and ref. [5, 24].
[38] J. C. SLATER and G. F. KOSTER: *Phys. Rev.*, **94**, 1498 (1954).
[39] For convenience of notation the definition of Q in this lecture is the reciprocal of the Q in ref. [46] and ref. [12].
[40] For energies more than approximately 1 Ryd above the bottom of the s-band the combined correction (see subsect. **4**'8) for the ASA and for the neglect of the higher partial waves should be included in addition.
[41] T. FUJIWARA: *J. Non-Cryst. Solids*, **61-62**, 1039 (1984); T. FUJIWARA, O. K. ANDERSEN and O. JEPSEN: to be published.
[42] R. HAYDOCK: *Solid State Phys.*, **35**, 215 (1980).
[43] E. P. WIGNER and F. SEITZ: *Phys. Rev.*, **43**, 804 (1933).
[44] R. M. PITZER, C. W. KERN and W. N. LIPSCOMB: *J. Chem. Phys.*, **37**, 267 (1962).
[45] D. GLÖTZEL, B. SEGALL and O. K. ANDERSEN: *Solid State Commun.*, **36**, 403 (1980).
[46] O. GUNNARSSON, O. JEPSEN and O. K. ANDERSEN: *Phys. Rev. B*, **27**, 7144 (1983): M. SCHEFFLER, F. BEELER, O. JEPSEN, O. GUNNARSSON, O. K. ANDERSEN and G. BACHELET: *J. Electron. Mater. A*, **14**, 45 (1985).
[47] O. K. ANDERSEN and S. SATPATHY: in *Colloquium on Basic Properties of Binary Oxides* (Sevilla, 1983), p. 21; K. SCHWARZ: in *Colloquium on Basic Properties of Binary Oxides* (Sevilla, 1983), p. 43.
[48] M. GRODZICKI, O. JEPSEN and O. K. ANDERSEN: to be published.
[49] W. A. HARRISON, O. JEPSEN and O. K. ANDERSEN: to be published.
[50] K. H. WEYRICH, O. JEPSEN and O. K. ANDERSEN: to be published.
[51] S. SATPATHY and O. K. ANDERSEN: *Inorg. Chem.*, to be published.
[52] L. HEDIN and B. I. LUNDQVIST: *J. Phys. C*, **4**, 2064 (1971), see also ref. [90].
[53] O. K. ANDERSEN: *Inst. Conf. Phys. Ser.*, No. **39**, 1 (1978).
[54] V. L. MORUZZI, J. F. JANAK and A. R. WILLIAMS: *Calculated Electronic Properties of Metals* (New York, N.Y., 1978).
[55] P. THIRY, D. CHANDESRIS, J. LECANTE, C. GUILLOT, R. PINCHAUX and Y. PETROFF: *Phys. Rev. Lett.*, **43**, 82 (1979); D. E. EASTMAN and F. J. HIMPSEL: in *Physics of Transition Metals*, edited by P. RHODES (London, 1981), p. 115.
[56] O. JEPSEN, D. GLÖTZEL and A. R. MACKINTOSH: *Phys. Rev. B*, **23**, 2684 (1981).
[57] J. BARDEEN: *J. Chem. Phys.*, **6**, 367 (1938).

[58] D. G. PETTIFOR: *J. Phys. F*, **7**, 613 (1977).
[59] W. A. HARRISON: *Electronic Structure and the Properties of Solids* (San Francisco, Cal., 1980).
[60] R. PODLOUCKY and D. GLÖTZEL: *Phys. Rev. B*, **27**, 3390 (1983).
[61] H. L. SKRIVER, O. K. ANDERSEN and B. JOHANSSON: *Phys. Rev. Lett.*, **41**, 42 (1978); **44**, 1230 (1980); B. JOHANSSON, H. L. SKRIVER, H. L. MARTENSSON, O. K. ANDERSEN and D. GLÖTZEL: *Physica (Utrecht) B*, **102**, 12 (1980); B. JOHANSSON, H. L. SKRIVER and O. K. ANDERSEN: in *Physics of Solids under High Pressure*, edited by J. S. SCHILLING and R. N. SHELTON (Amsterdam, 1981), p. 245.
[62] W. A. HARRISON: *Phys. Rev. B*, **28**, 550 (1983).
[63] D. D. KOELLING and B. N. HARMON: *J. Phys. C*, **10**, 3107 (1977).
[64] D. G. PETTIFOR: *J. Phys. C*, **3**, 367 (1970).
[65] J. ASHKENAZI, M. DACOROGNA, M. PETER, Y. TALMOR and E. WALKER: *Phys. Rev. B*, **18**, 4120 (1978).
[66] C. M. WARMA and W. WEBER: *Phys. Rev. Lett.*, **39**, 1094 (1977).
[67] R. HOFFMANN: Nobel Lectures, *Angew. Chem.*, **94**, 725 (1982).
[68] D. G. PETTIFOR: *Commun. Phys.*, **1**, 141 (1976).
[69] V. HEINE: *Solid State Phys.*, **35**, 1 (1980).
[70] U. K. POULSEN, J. KOLLAR and O. K. ANDERSEN: *J. Phys. F*, **6**, L241 (1976); O. K. ANDERSEN, J. MADSEN, U. K. POULSEN, O. JEPSEN and J. KOLLAR: *Physica (Utrecht) B*, **86-88**, 249 (1977).
[71] H. L. SKRIVER and O. K. ANDERSEN: *Inst. Phys. Conf. Ser.*, No. **39**, 100 (1978).
[72] D. G. PETTIFOR: *J. Phys. F*, **8**, 219 (1978).
[73] D. GLÖTZEL and A. K. MCMAHAN: *Phys. Rev. B*, **20**, 3210 (1979).
[74] O. K. ANDERSEN, H. L. SKRIVER, H. NOHL and B. JOHANSSON: *Pure Appl. Chem.*, **52**, 93 (1979).
[75] P. KELLY, T. M. RICE and O. K. ANDERSEN: to be published.
[76] A. J. FREEMAN and T. JARLBORG: in *Superconductivity in Ternary Compounds* II, edited by M. B. MAPLE and O. FISCHER (Heidelberg, New York, N.Y., 1982), p. 167; T. JARLBORG and A. J. FREEMAN: in *Superconductivity in d- and f-band Metals*, edited by W. BUCKEL and W. WEBER (Karlsruhe, 1982), p. 153.
[77] D. G. PETTIFOR: *Phys. Rev. Lett.*, **42**, 846 (1979).
[78] J. KOLLAR and O. K. ANDERSEN: to be published.
[79] N. E. CHRISTENSEN: *Solid State Commun.*, **49**, 70 (1984); N. E. CHRISTENSEN, D. GLÖTZEL and O. K. ANDERSEN: to be published.
[80] J. FRIEDEL: in *The Physics of Metals*, edited by J. M. ZIMAN (Cambridge, 1969), p. 340; J. D. DOW: this volume, p. 465.
[81] E. P. WIGNER and F. SEITZ: *Solid State Phys.*, **1**, 96 (1955).
[82] M. H. WHANGBO and R. HOFFMANN: *J. Am. Chem. Soc.*, **100**, 6093 (1978).
[83] D. W. BULLETT: *Solid State Phys.*, **35**, 129 (1980).
[84] A. K. MCMAHAN and J. A. MORIARTY: *Phys. Rev. B*, **27**, 3235 (1983).
[85] H. L. SKRIVER: *Phys. Rev. Lett.*, **49**, 1768 (1982).
[86] H. L. SKRIVER: to be published.
[87] D. GLÖTZEL, D. RAINER and H. R. SCHOBER: *Z. Phys. B*, **35**, 317 (1979).
[88] D. L. YIN and L. Y. ZHANG: *Acta Phys. Sin.*, **29**, 677 (1980).
[89] J. C. DUTHIE and D. G. PETTIFOR: *Phys. Rev. Lett.*, **38**, 564 (1977).
[90] U. VON BARTH and L. HEDIN: *J. Phys. C*, **5**, 1629 (1972).
[91] O. GUNNARSSON: *J. Phys. F*, **6**, 587 (1976).
[92] S. H. VOSKO and J. P. PERDEW: *Can. J. Phys.*, **53**, 1385 (1975).
[93] J. F. JANAK: *Phys. Rev.*, **16**, 255 (1977).
[94] H. L. SKRIVER: *J. Phys. F*, **11**, 97 (1981); J. KÜBLER: *J. Magn. Magn. Mater.*, **20**, 277 (1980).

[95] N. CADE: *J. Phys. F*, **10**, L187 (1980).
[96] C. S. WANG and J. CALLAWAY: *Phys. Rev. B*, **15**, 298 (1977); J. CALLAWAY and C. S. WANG: *Phys. Rev. B*, **16**, 2095 (1977).
[97] J. F. JANAK: *Phys. Rev. B*, **20**, 2206 (1979).
[98] D. E. EASTMAN, F. J. HIMPSEL and J. A. KNAPP: *Phys. Rev. Lett.*, **40**, 1514 (1978); F. J. HIMPSEL, J. A. KNAPP and D. E. EASTMAN: *Phys. Rev. B*, **19**, 2919 (1979).
[99] A. LIEBSCH: *Phys. Rev. Lett.*, **43**, 1431 (1979).
[100] A. M. OLES and G. STOLLHOFF: *Phys. Rev. B*, **29**, 314 (1984); S. HORSCH, P. HORSCH and P. FULDE: *Phys. Rev. B*, **29**, 1870 (1984).
[101] O. GUNNARSSON, M. JONSON and B. I. LUNDQVIST: *Phys. Rev. B*, **20**, 3136 (1979); G. KERKER: *Phys. Rev. B*, **24**, 3468 (1981); H. PRZYBYLSKI and G. BORSTEL: to be published; M. S. HYBERTSEN and S. LOUIE: *Solid State Commun.*, **51**, 451 (1984); F. MANGHI, G. RIEGLER, C. M. BERTONI, C. CALANDRA and G. B. BACHELET: *Phys. Rev. B*, **28**, 6157 (1983).
[102] G. STRINATI, H. J. MATTAUSCH and W. HANKE: *Phys. Rev. B*, **25**, 2867 (1982); *Phys. Rev. Lett.*, **45**, 290 (1980); W. HANKE, T. GÖLZER and H. J. MATTAUSCH: *Solid State Commun.*, **51**, 23 (1984).
[103] G. MATERLIK, J. E. MÜLLER and J. W. WILKINS: *Phys. Rev. Lett.*, **50**, 267 (1983).
[104] J. MADSEN, O. K. ANDERSEN, U. K. POULSEN and O. JEPSEN: in *Magnetism and Magnetic Materials 1975* (New York, N.Y., 1976), p. 327.
[105] T. OGUCHI, K. TERAKURA and A. R. WILLIAMS: *Phys. Rev. B*, **28**, 6443 (1983); K. TERAKURA, A. R. WILLIAMS, T. OGUCHI and J. KÜBLER: *Phys. Rev. Lett.*, **52**, 183 (1984).
[106] J. YAMASHITA and S. ASANO: to be published.
[107] U. GRADMANN and H. O. ISBERT: *J. Magn. Magn. Mater.*, **15-18**, 1109 (1980).
[108] R. M. BOULET, J. P. JAN and H. L. SKRIVER: *J. Phys. F*, **12**, 293 (1982).
[109] H. NOHL and O. K. ANDERSEN: in *Superconductivity in d- and f-band Metals*, edited by W. BUCKEL and W. WEBER (Karlsruhe, 1982), p. 161; P. J. KELLY and O. K. ANDERSEN: in *Superconductivity in d- and f-band Metals*, edited by W. BUCKEL and W. WEBER (Karlsruhe, 1982), p. 137.
[110] J. J. FINLEY, H. NOHL, E. E. VOGEL, H. IMOTO, R. E. CAMLEY, V. ZEVIN, O. K. ANDERSEN and A. SIMON: *Phys. Rev. Lett.*, **46**, 1472 (1981).
[111] T. JARLBORG, A. JUNOD and M. PETER: *Phys. Rev.*, **27**, 1558 (1983), and references therein.
[112] T. JARLBORG, A. A. MANUEL and M. PETER: *Phys. Rev. B*, **27**, 4210 (1983).
[113] L. F. MATTHEISS and D. R. HAMANN: *Solid State Commun.*, **38**, 689 (1981).
[114] T. JARLBORG and A. J. FREEMAN: *J. Appl. Phys.*, **53**, 8041 (1982).
[115] J. KOLLAR, U. K. POULSEN and O. K. ANDERSEN: in *Proceedings of the VIII Symposium on Electronic Structure of Metals and Alloys* (Dresden, 1978), p. 29.
[116] R. J. WEISS: *Proc. Phys. Soc. London*, **82**, 281 (1963).
[117] D. G. PETTIFOR: *J. Phys. F*, **7**, L183 (1977).
[118] A. R. WILLIAMS, V. L. MORUZZI, C. D. GELATT and J. KÜBLER: *J. Magn. Magn. Mater.*, **31-34**, 88 (1983); J. KÜBLER, A. R. WILLIAMS and C. B. SOMMERS: *Phys. Rev. B*, **28**, 1745 (1983).
[119] A. R. WILLIAMS, V. L. MORUZZI, A. P. MALOZEMOFF and K. TERAKURA: *IEEE Trans. Magn.*, MAG-**19**, 1983 (1983).
[120] M. S. S. BROOKS: *J. Phys. F.*, **14**, 639, 653, 1157 (1983).
[121] M. S. S. BROOKS and P. J. KELLY: *Phys. Rev. Lett.*, **51**, 1708 (1983).

[122] A. R. WILLIAMS, C. D. GELATT and V. L. MORUZZI: *Phys. Rev. Lett.*, **44**, 429 (1980); C. D. GELATT, A. R. WILLIAMS and V. L. MORUZZI: *Phys. Rev. B*, **27**, 2005 (1983).
[123] A. R. MIEDEMA, P. F. DECHATEL and F. R. DE BOER: *Physica (Utrecht) B*, **100**, 1 (1980).
[124] C. KOENIG, N. E. CHRISTENSEN and J. KOLLAR: *Phys. Rev. B*, **29**, 6481 (1984).
[125] F. CYROT LACKMANN: *J. Phys. (Paris), Suppl.*, C **1**, 67 (1970).
[126] R. V. KASOWSKI: *Phys. Rev. Lett.*, **33**, 83, 1147 (1974); **37**, 219 (1976); R. V. KASOWSKI: *Solid State Commun.*, **17**, 179 (1975); R. V. KASOWSKI and E. CARUTHERS: *Phys. Rev. B*, **21**, 3200 (1980).
[127] R. FEDER, S. F. ALVARADO, E. TAMURA and D. KISKER: *Surf. Sci.*, **127**, 83 (1983).
[128] H. KRAKAUER, A. J. FREEMAN and E. WIMMER: *Phys. Rev. B*, **28**, 610 (1983).
[129] D. S. WANG, A. J. FREEMAN and H. KRAKAUER: *Phys. Rev. B*, **24**, 1126 (1981); **26**, 1340 (1982).
[130] R. RICHTER and J. W. WILKINS: *J. Vac. Sci. Technol. A*, **1**, 1089 (1983).
[131] E. WIMMER, H. WEINERT, A. J. FREEMAN and H. KRAKAUER: *Phys. Rev. B*, **24**, 2292 (1981); D. S. WANG, A. J. FREEMAN, H. KRAKAUER and M. POSTERNAK: *Phys. Rev. B*, **23**, 1685 (1981).
[132] D. S. WANG, A. J. FREEMAN and H. KRAKAUER: *Phys. Rev. B*, **24**, 3092, 3104 (1981).
[133] G. A. BENESH, H. KRAKAUER, D. E. ELLIS and M. POSTERNAK: *Surf. Sci.*, **104**, 599 (1981).
[134] H. KRAKAUER, M. POSTERNAK and A. J. FREEMAN: *Phys. Rev. Lett.*, **43**, 1885 (1979); M. POSTERNAK, H. KRAKAUER, A. J. FREEMAN and D. D. KOELLING: *Phys. Rev. B*, **21**, 5601 (1980); M. POSTERNAK, H. KRAKAUER and A. J. FREEMAN: *Phys. Rev. B*, **25**, 755 (1982); O. JEPSEN and J. W. WILKINS: to be published.
[135] R. RICHTER and J. W. WILKINS: *Surf. Sci.*, **128**, L190 (1983).
[136] E. WIMMER, A. J. FREEMAN, M. WEINERT, H. KRAKAUER, J. R. HISKES and A. M. KARO: *Phys. Rev. Lett.*, **48**, 1128 (1982): E. WIMMER, A. J. FREEMAN, J. R. HISKES and A. M. KARO: *Phys. Rev. B*, **28**, 3074 (1983).
[137] N. ESBJERG and J. K. NØRSKOV: *Phys. Rev. Lett.*, **45**, 807 (1980).
[138] M. J. CARDILLO, G. E. BECKER, D. R. HAMANN, J. A. SERRI, L. WHITMAN and L. F. MATTHEISS: *Phys. Rev. B*, **28**, 494 (1983); D. R. HAMANN, L. F. MATTHEIS and H. S. GREENSIDE: *Phys. Rev. B*, **24**, 6151 (1981).
[139] M. EL-BATANOUNY, D. R. HAMANN, S. R. CHUBB and J. W. DAVENPORT: *Phys. Rev. B*, **27**, 2575 (1983).
[140] P. J. FEIBELMAN and D. R. HAMANN: *Phys. Rev. B*, **28**, 3092 (1983).
[141] A. R. MIEDEMA and J. W. F. DORLEIJN: *Surf. Sci.*, **95**, 447 (1980).
[142] A. R. WILLIAMS and U. VON BARTH: in *Applications of Density-Functional Theory to Atoms, Molecules and Solids*, edited by N. MARCH and S. LUNDQVIST (1983), p. 89.
[143] See, for instance, M. V. YOU and V. HEINE: *J. Phys. F*, **12**, 177 (1982); T. OGUCHI, K. TERAKURA and N. HAMADA: *J. Phys. F*, **13**, 145 (1983); J. W. D. CONNOLLY and A. R. WILLIAMS: *Phys. Rev. B*, **27**, 5169 (1983).
[144] See also M. METHFESSEL and J. KÜBLER: *J. Phys. F*, **12**, 141 (1982); O. H. NIELSEN and R. MARTIN: *Phys. Rev. Lett.*, **50**, 697 (1983).

Reprinted From
Highlights of
Condensed-Matter Theory

Soc. Italiana di Fisica - Bologna - Italy